Università di Pisa

Facoltà di Scienze Matematiche Fisiche e Naturali

Dottorato in Fisica Applicata

VI ciclo

Tesi di Dottorato

Development of a Positron Emission Tomograph for "in-vivo" Dosimetry in Hadrontherapy

Candidato:
Sara Vecchio

Relatore:
Alberto Del Guerra

Introduction and outlook

Cancer is second only to heart disease as cause of premature death in Europe. In 2006 in Europe, there were an estimated 3.2 million new cancer cases diagnosed (excluding nonmelanoma skin cancers) and about 1.7 million deaths from cancer [1]. The present diagnostic techniques allows the diagnosis of about 60% of all cancers at the stage of a localized primary tumor, but even among those cases the current tumor treatments still fail for 20% of patients. At present [2], the only available tools for non-systemic curative treatment, are surgery and radiotherapy.

In radiotherapy there is still room for improvements through the research of new treatments which might reduce to a minimum the ratio of normal tissue dose to tumor dose. This is desired to allow higher and more effective radiation doses to be safely delivered to tumors, reducing (or at least without increasing) the treatment toxicity to healthy surrounding tissues.

On the other hand, in order to make the most of the higher physical selectivity and biological effectiveness achievable with the recent techniques, an increasing accuracy of treatment delivery and a growing attention to quality assurance are required.

Since the seventies [3] the possibility was explored of detecting and localizing, in real time, the exact point of maximum ionization (Bragg's peak) of a hadronic beam, through a PET system adapted for the on-line detection of β^+ emitter isotopes produced (or injected) by the beam in the biological tissue. However, the research was not intensively pursued for a long time, until hadrontherapy became a better established technique and the initial idea generated new interest [4, 5, 6, 7, 8, 9]. The basic principles of hadron-driven PET technique and the state of the art in this research field are reminded in chapter 1.

The DoPET project, developed by an Italian INFN collaboration, aims to explore one possible approach to the hadron-driven PET technique. Its start coincided with the beginning of my PhD research, therefore I was able to follow each stage of the project evolution.

The final goal of the DoPET project, and the main core of this thesis, is to evaluate the feasibility of a dedicated PET system for dose monitoring of hadrontherapy. Such goal has been reached through the validation of a PET prototype with proton irradiation on plastic phantoms at the CATANA proton therapy facility (Catania, Italy) [10]. The CATANA project was developed to treat ocular pathologies like uveal melanoma, which is the most frequent eye tumor in adults. The final application will require the realization of a larger and more refined detector. The system and the methods described in this thesis have to be considered as a proof of principle, which is needed so as to justify a larger effort for the construction of a clinical system. A description of DoPET experiment and some basic information about the CATANA project are given in chapter 2. The design of mechanical support and the following detector assembly were both performed at Pisa division of INFN, under my supervision.

The usefulness of the PET for hadrontherapy monitoring is assured by a detection capability of deviations equal to (or lower than) 1 mm in the dose distribution from the reconstructed image of the β^+-induced activity. Although the final aim of the in-beam PET is the determination of the delivered dose distribution, the primary goal for a proof of principle can be to reach a detection capability of deviations of the order of the millimeter for the proton range, i.e., only for one direction. In the following it will be shown that the DoPET prototype is able to achieve 1 mm shift detection capability in the activity distal profiles, but no univocal extrapolation of the corresponding dose distal shifts nor detection of the longitudinal extension of the spread-out Bragg peak have been yet stated. Work must still go on towards more precise conclusions.

The accuracy of the measurement is affected by the detector performances in terms of detection efficiency as well as (planar) spatial and energy resolutions, the acquisition time, and the algorithms used to reconstruct the β^+ activity and to determine the Bragg's peak position.

As a preliminary step of a project realization, Monte Carlo simulations and analytical methods must be used to perform a detailed evaluation of the activity intensity and distribution, as well as of the detector efficiency. This would provide a basis for the comparison of subsequent results in experimental measurements at the beam-line. Methods and results are presented in chapter 3: my contribution in this subject includes the development of one "ad-hoc" version of the GEANT4 `Hadrontherapy` routine, with a selection of simulated physical processes tailored to the generation of an isotope production database, and the comparison of my results with those obtained by other prediction methods available in literature.

In the first phase of the project, during the design of the detector, the focus

was on the detector performances. It was required an optimal choice of the crystal (in terms of material, thickness, pixel and pitch size) and of the photo-detector. Since the H8500 PSPMT offers several possibilities for the signals read out, an important task was also to reach the best solution for a simple and performing read out system. Results of these preparatory studies are reported in chapter 4: I did all the measurements presented, except for those shown in table 4.4 and figure 4.6.

The reconstruction algorithm of the β^+ activity distribution has been derived from a 3D EM-ML iterative algorithm, that makes use of all the collected lines-of response. Several approach for data pre-correction and probability matrix generation have been considered before reaching the final implementation. At the beginning, a purely geometrical version of the probability matrix was chosen for the algorithm implementation and had led to promising results. We have carried on with this approach for two years, and I have personally performed its adaption to the experimental setup, as well as the implementation of data corrections within the planogram generation. However the simplicity of the software affected the numerical precision and the information content of the reconstructed data. In particular, heavy modifications were required to remove the presence of strong voxel-dependent artifacts and to discard the adoption of an arbitrary normalization of the reconstructed activity. The reconstruction algorithm presently adopted is described in section 5.1. My contribution in that version of the reconstruction software is limited to the introduction of the additional correction required by the natural radioactivity of LYSO scintillator crystal (section 5.1.3). The original simplified solution is now still used for fast reconstruction during the data taking at the beam facility.

Besides the uncertainties due to the implemented algorithm itself, the resolution of reconstructed images is affected by the statistics available in the measurements, and by the accuracy of the head positioning. I performed an intrinsic evaluation of the overall detector performances by means of measurements with β^+ point sources. Methods and results are reported in chapter 6.

Measurements after phantom irradiations have then been planned and performed. The criteria for data analysis must then be settled and implemented, in order to perform a proper comparison of the results at different conditions and to draw conclusions for the future work. Results and discussion are presented in chapter 7. The whole content of that chapter (except for the dosimetric measurements) is part of my work: I was involved in the measurement planning, in all the data taking, and in the entire data analysis.

As a final step, in order to demonstrate the feasibility of a clinical device, the

choice (or the development) of a deconvolution algorithm is essential. In fact, the final aim of the in-beam PET is the determination of the delivered dose distribution. The extrapolation of dose information from the activity distribution is the most critical and challenging issue, due to the low statistics available from a clinical proton beam at such low energies. This last subject is investigated by another member of the DoPET group, however, due to the importance of this final step, the adopted method and the results are also reported in sections 5.2 and 7.5, respectively.

As final remark, it is worth mentioning that the choice of the CATANA beamline as the supporting hadrontherapy facility was mainly due to opportunity reasons (CATANA is the only facility available in Italy) and that the DoPET project is a proof of principle experiment. However, the opportunities of a dedicated project for eye-monitoring therapy has risen some interest in the CATANA group. As reminded in section 2.2, from one center to another, the beam characteristics (and then the adopted protocol) may slightly vary. Even if we are dealing with a well established technique, an additional device for treatment monitoring could help to refine the therapy protocol and further reduce the risk of failure in tumor control or of post-irradiation sight-limiting side effects.

In the perspective of a wider field of application, and considering also the existence of one facility for carbon ion therapy for ocular melanoma [11, 12], some efforts have been made to start a validation of the DoPET detector on plastic phantoms under ^{12}C irradiation, that induces activation of both target and projectile itself. The very preliminary analysis of the first data taking at the GSI synchrotron are presented in appendix B, and compared with the performances of the hadron-driven detector available there.

Contents

Chapter 1

Hadrontherapy and treatment quality

Radiotherapy is the therapeutic use of ionizing radiations. The energy delivered to the biological tissues through irradiation, in fact, is known to likely cause irreversible damages to cell DNA, and may therefore be used as "non-invasive" method to kill tumoral tissues.

The *absorbed dose* is a measure of the energy deposited in a medium by ionizing radiation. It is equal to the energy deposited per unit mass, and its SI unit is J/kg, indicated with the special name gray (Gy) [13]. The absorbed dose D is not a good indicator of the likely biological effect: appropriate weighting factors can be applied to reflect the different relative biological effectiveness (RBE).

The weighted quantities have the same physical units of the absorbed dose (J/kg), but a different name is given, to underline their biological meaning. The *biological effective dose* delivered by a certain radiation quality is usually normalized to the clinical benefits of γ photons from ^{60}Co and its unit of measurement is called GyE (gray equivalent) or CGE (cobalt gray equivalent).

Over the last five decades external radiotherapy with photon and electron beams has increased the conformity of the dose equivalent applied to the tumour by replacing traditional sources such as X-ray tubes (energy $\leq$ 200 keV) or radioactive isotopes e.g. ^{60}Co (average photon energy of 1.25 MeV) by modern high-energy (4 - 20 MeV) linear accelerators delivering irradiation from several directions (called *portals*). One of the major achievements in the field of radiotherapy, especially with photons, is the development of 3D conformal radiotherapy (CRT) [14], where the radiation field is geometrically shaped according to the volume of the tumour. The latest and most innovative form of photon CRT is in-

tensity modulated radiotherapy (IMRT) [14, 15], which uses dynamic geometrical field shaping so as to produce a spatially non-uniform photon flux for each of the several beam portals applied to the patient.

Despite all the advances in radiotherapy and the rapidly growing IMRT technique, the therapeutic effectiveness of conventional electromagnetic radiation is intrinsically constrained by its physical and radiobiological properties.

The indirectly ionizing beams, like photon (or neutron) beams, are exponentially attenuated during their passage through matter. As a consequence, (for each portal beam) the dose delivered to the patient skin is always higher than the one delivered in depth. Since total absorption for neutral radiation in matter corresponds to infinite material thickness, there is always also a consistent dose delivery beyond the region of interest.

The unfavourable depth dose profile and the lateral scattering impair the achievable physical selectivity and forbid high precision irradiation of tumours deep-seated and close to critical organs. Moreover, the low biological effectiveness is inadequate for the treatment of radioresistant tumours, despite all attempts to improve radiation response. Hadrontherapy, i.e., the use of light nuclei beams[1], may overcome the limits of conventional radiotherapy thanks to a more localized energy deposition (both in depth and transversally) and a higher relative biological effectiveness.

In figure 1.1 there are shown the typical in-depth profiles of energy deposit for photon and proton beams.

Heavy[2] charged particles mainly loose energy through Coulomb interactions with electrons of the crossed medium, slowly depositing energy during their passage through matter by multiple collisions. When almost all the energy of the charged particle has been transferred to the medium, and the particle velocity is then small, additional interaction processes makes the energy loss per unit length to increase. This phenomenon turns out into a well defined dose depth profile: a low dose delivery up to the end of the particle range (*plateau*), and then a sharp increase (*Bragg's peak*) followed by a rapid decrease after the particle is thermalized.

The depth of the peak in a specific material depends on the initial particle $\beta\gamma$ value (impulse divided by the ion mass), and the peak width is determined by the

[1] Among the hadrons used there are also neutron and pion beams, but such alternatives do not find large employment.

[2] For electrons, ionization loss by electrons and positrons differs from loss by heavy particles because of the kinematics, spin, and the Pauli principle. Moreover the Bremsstrahlung loss is not negligible at the typical therapeutic energies (few MeV).

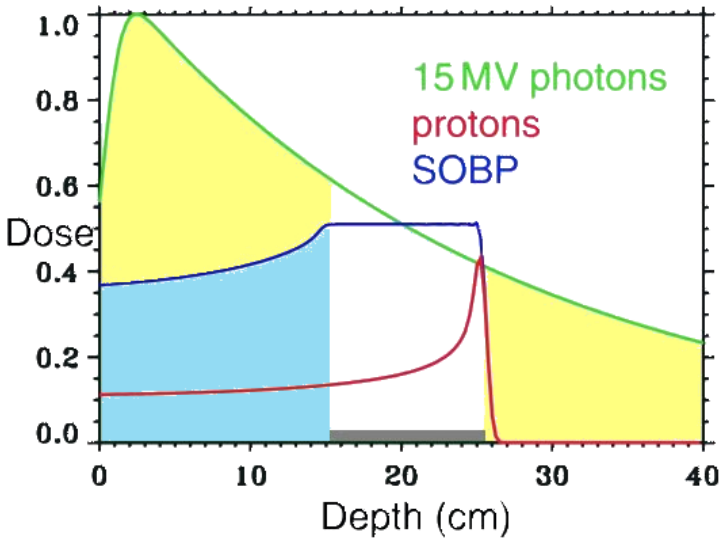

Figure 1.1: Depth dose profiles of proton (red curve) and photon (green curve) beams [16]. Through the superposition of many proton beams of different residual range it is possible to deposit a homogenous dose (blue curve) in the region of the tumor (in this case from 15 to 25 cm depth). One recognizes from the picture the potential of dose sparing of the protons in the entrance and exit region of the beam (the unnecessary dose is painted in pale blue for proton and yellow for photon).

spread in energy of the beam. By varying the beam energy (and the intensity) during the irradiation, one can superimpose several sharp Bragg's peaks, and therefore conform the dose profile to tumours extended in depth (SOBP: Spread Out Bragg Peak). This slightly degrades the favourable entrance-to-target dose ratio, but the advantage over photon depth profile is still remarkable. The energy modulation can be achieved by changing accelerator parameters (only in synchrotrons) or by interposing blocks of material of the suitable thickness to slow down the beam.

However, it is worth noticing that the advantage of heavy charged particles cannot be simply measured on the one-dimensional dose depth profiles. A comparison between IMRT and multi-portal hadrontherapy treatment plannings (see figure 1.2) still favours the latter in terms of number of portal beams and healthy tissue sparing.

All ions from hydrogen to neon can be used with similar results, the preferred choice being protons and carbon ions. At a fixed energy, the heavier is the ion, the shorter is its range in matter. Since protons are the lightest ion they require the

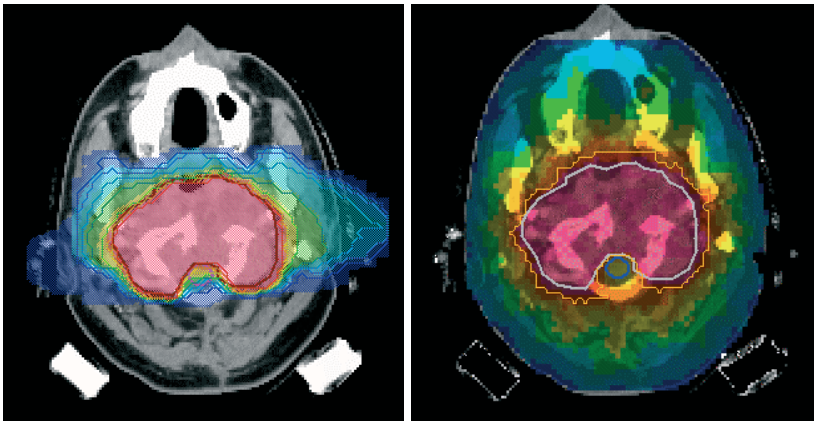

Figure 1.2: Comparison of treatment plans. Left: Carbon ions two fields. Right: IMRT nine fields. [17]

lowest energy to reach a chosen depth in tissue. Therefore they offer the advantage of the technique at the minimum production cost. Moreover, their sharp dose fall-off after the Bragg peak makes them the election method for pediatric tumours, where the risk of radio-induced tumour in healthy tissues is much higher. Carbon ions generally offer one of the best compromize between high radiation quality factor and good treatment accuracy. In fact, the increase in ion mass corresponds to an increase in relative biological effectiveness at a fixed energy with respect to proton beams. Moreover, since the lateral spread due to multiple scattering decreases with the increasing ion mass, carbon ions are favoured with respect to proton as for the transversal beam collimation. On the other side, heavier nuclei are more likely subjected to fragmentation: the low-Z fragments (mainly protons and alpha particles [18]) on average have a longer range than the primary particle. The carbon Bragg's peak is then followed by a "tail", that can impair the accuracy of the treatment. For ion heavier than neon, fragmentation is so relevant that makes the beam useless for therapeutic applications. Renewed interest has been recently registered for ions between carbon and hydrogen, expecially ^{4}He and ^{7}Li [19].

The high performing ion therapy demands in turn a high accuracy in monitoring of the applied treatment, especially when the target volume is located next to critical organs and a fractionated therapy is applied. In fact, minimal discrepancies from the therapy planning X-ray CT might lead to deviations of the ions delivery and produce dramatic spatial changes of the planned dose. Discrepancies may derive from local anatomical changes or variations in the positioning of the

patient between the CT acquisition and the treatment fraction. Uncertainties in the calculation of hadron stopping powers from the CT attenuation coefficients should also be taken into account.

In vivo information on the range of ions is desirable; however, the stopping of the ions in patient prevents the application of conventional electronic portal imaging [20] methods as used in radiotherapy for controlling the lateral field position. Moreover, since in ion therapy the formation of the Bragg maximum at the correct depth is crucial, imaging in the third spatial dimension is required.

Proton radiography [21], proton tomography [22], and hadron-driven PET [3] are among the most promising imaging methods for a more refined planning of the hadrontherapy treatment. These techniques are not yet used in the clinical routine[3], although their advantages are undisputed. In fact, proton transmission techniques could provide a precise measurement of the range of the hadrons in patient before the therapeutical irradiation, while PET provides an indirect information of the dose profile delivered after the treatment fraction.

1.1 Hadron-driven PET

Positron Emission Tomography (PET) is based on the simultaneous detection of the back-to-back 511 keV photons derived from the annihilation of a positron emitted by radioactive nuclei. Its standard application is functional imaging, i.e., the imaging of β^+ emitting radiopharmaceutical tracers. The precise signature of a double (in time coincidence) signal from an annihilation event, and the knowledge of the line-of-response without the need of collimators, makes PET a well established clinical technique.

The image reconstruction is based on analytical or iterative algorithms. The information available is the ”line of response” (LOR), defined by the point of detection of the two opposed photons[4]. When detectors are pixilated, the lines of response are substituted by tubes of response. A pixel pair, belonging to opposed detectors in the planar tomograph, defines a detection tube. The analytical method reconstructs *a posteriori* the activity distribution from the integrals of the activity detected along each tube of response. The second method statistically resolves the activity distribution based on a model of the tomograph geometry, i.e., of

[3]Except for few sites in the world which adopt the hadron-driven PET.

[4]The ”line of flight” (LOF) can be also defined, as the real unknown line determining the photons flight direction.

an *a priori* estimate of the potential contribution of each detection tube to the tomograph response.

The point of origin of the two annihilation photons is about 1-2 millimeter far away from the emitting atom, since this is the average range of the low energy positron before annihilation with an electron of the biological tissue for most positron emitters used in the clinical studies. In addition, when trying to recover the annihilation point from the LOR, one should take into account the deviation from γ-γ co-linearity due to non-at-rest annihilations[5]. The distribution width of the angular deviation is about 0.5° (FWHM) in water [23]. The imaging capability of a PET is then intrinsically limited in resolution by the physical process, even without taking into accounts the limits of the specific reconstruction algorithm adopted and the instrumentation effects which can be minimized (see section 5.1).

The first suggestion for the employment of PET as in-beam technique was based on a preliminary irradiation of the patient with low-intensity radioactive beams, of the same element used for the subsequent therapeutic irradiation [24]. The technique developed at the Lawrence Berkeley National Laboratory (LBL) was pursued until the clinical application was realized. However, the research was terminated by the shutdown of the accelerator.

The use of positron radioactive ions as projectiles for dose delivery is the approach followed at the Heavy Ion Medical Accelerator in Chiba (Japan), where a radioactive beam line delivering ^{11}C or ^{10}C ions has been installed [25, 26]. Such a radioactive beam delivers an activity density within the irradiated volume of 10^3-10^5 Bq·Gy^{-1}·cm^{-3} depending on the half-life of the isotope. Using this approach a very accurate (< 1 mm) range verification is obtainable. However, the method seems to be of minor relevance for practical therapy, since the production rate of secondary radioactive ions is of the order of 0.1-1%, which requires expensive measures for absorbing and shielding the primary beam.

The applications using radioactive beams are presently limited by the high cost of a facility producing them. The phenomenon mostly used is instead the target activation by stable beams, since such approach has the appeal to save the patient from any additional dose delivery besides the therapeutic one. All particles used in hadrontherapy, protons included, induce in the biologic material nuclear reactions which lead to the production of β^+ emitters, mainly ^{15}O and ^{11}C, from their parent stable isotopes which constitute the tissues. By using ions like carbon,

[5]The Fermi momentum of the electrons and the thermal motion of the particles (both electrons and positrons) produce a boost of the center of mass of the positron-electron system. In-flight annihilation, before positron thermalization, have only 2% probability. Another source of deviation from co-linearity is the formation of electron-positron bound states before annihilation.

oxygen or fluorine, there is a further production of other β^+ emitters, through the fragmentation of the projectiles themselves.

Since carbon and proton beams are the preferred choice in hadrontherapy, research for hadron-driven PET has focussed on the same beams. The activity density is rather low in both cases: for beam irradiation on PMMA there were measured few hundreds of $Bq \cdot Gy^{-1} \cdot cm^{-3}$ [27].

Motivated by the experience with proton- and carbon-driven PET and in connection with the rapidly growing number of ion beam therapy facilities worldwide, an increasing interest has been devoted to PET imaging for quality assurance not only of carbon and hydrogen ions but also of ^{3}He [28], ^{16}O [29] and even hard photon [6] beam [30, 31].

isotope	half life $T_{\frac{1}{2}}$ [s]	β^+ spectrum endpoint [MeV]
^{11}C	1222.8	0.96
^{15}O	122.2	1.73
^{10}C	19.3	0.90
^{13}N	597.6	1.19

Table 1.1: Main β^+ emitters induced by hadron irradiations. The order of isotopes corresponds to their relevance in PET image formation for a proton beam irradiation.

The main detectable β^+ emitters produced by tissue activation are listed in table 1.1. Their relative importance as contribution to the PET image is mainly determined by their half life. The half life of the emitters is a factor that strongly influences their importance for a PET imaging. Too rapid decays, in fact, drastically reduce the collected statistics if there is a delay between irradiation and measurement. On the other side, lifetimes longer than tens of minutes requires very long acquisition times which do not match with the patient confort and the rapid washout [32] of a large part of the produced activity through biological processes. The importance of activity contributions from each radioisotope also depends by production cross sections and parent isotope abundances in the target.

The activity distributions produced by stable beams is not directly proportional to the delivered dose, because of the different nuclear and atomic processes

[6] In fact, positron emitters can be also generated by (γ,n) photonuclear reactions between photons with energies above 20 MeV and nuclei of the tissue. The energy threshold is fulfilled up to now only in a few cases of therapeutic application, for example at the IMRT with pencil beams of hard Bremsstrahlung photons (E_{max} = 50 MeV) [14].

underlying β^+-activation and the dominant mechanism of energy deposition, respectively. The information about the beam range and the distal dose fall-off is primarily inferred from the distal edge of the activity distribution [33]. In the case of medium-Z ion beams, the additional emitter production due to projectile fragmentation leads to a higher correlation between distal dose fall-off and activity depth profile, with respect to very light ions, so that even the proximal edge of the activity distribution is a clear source of information (see figure 1.3).

1.1.1 Proton-driven and ^{12}C-driven PET

Two effects contribute to the weaker spatial correlation which characterizes the β^+ activity profile and the dose depth profile for proton therapy, as compared to medium-Z ion therapy. First, the β^+ emitter production is inhibited several millimetres before the location of the Bragg's peak, by the absence of projectile fragmentation and the 15-20 MeV thresholds characterizing proton-induced nuclear reactions. Furthermore, the different relative abundance of produced isotopes must be taken into account. Without projectile fragmentation, the main β^+ radioactive isotope produced derives from reactions with the most abundant element in tissue (^{16}O), while for ion beams the major contribution derives from isotopes of the stable beam. The positron emitted by ^{15}O has on average a higher energy and then a longer mean free path with respect to the positrons emitted by ^{11}C (see table 1.1).

Despite these limitations, PET imaging is relevant for low-Z as well as for medium-Z ion therapy. The total charge needed with protons to bring a given effective dose to the tissue is greater than the required one with carbon ions. In fact, it has been proven that the relative biological effectiveness of protons is lower than for carbon ions. As a consequence, for equal effective dose, irradiation with protons induces a higher β^+ activity with respect to the carbon irradiation [6]. The better statistics could allow the determination of the Bragg's peak position with the appropriate resolution from the position of the β^+ activity distal edge.

1.1.2 In-beam PET

For dose profile monitoring, the possibility of on-line measurements, i.e., immediately after patient irradiation, is of major importance since this is the only way to exploit the maximum statistics, by detecting also the activity contribution provided by short lived isotopes such as ^{15}O, and to reduce the acquisition time for a minimized discomfort of the patient. Moreover, in-situ measurements allow one

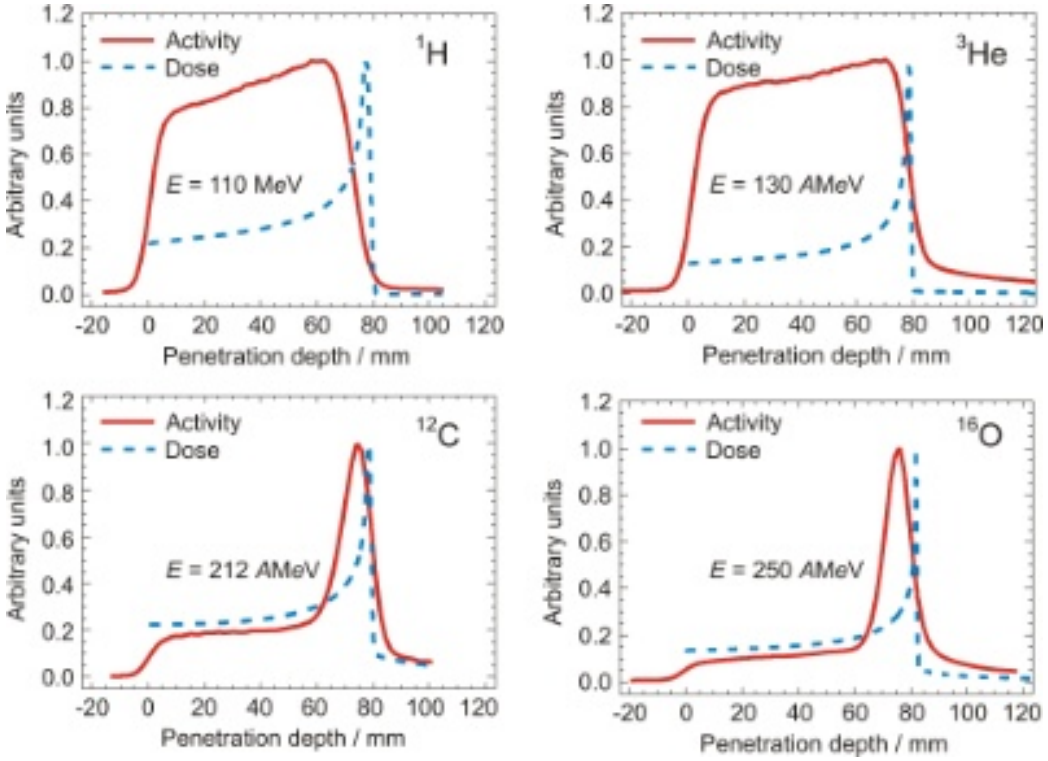

Figure 1.3: Normalized depth distributions of calculated dose (blue, dashed) and measured β^+-activity (red, solid) induced by beams of protons as well as ^{3}He, ^{12}C and ^{16}O ions in thick targets of polymethyl-methacrylate [34]. The prominent maxima in the cases of ^{12}C and ^{16}O are formed by positron radioactive projectile fragments, whereas the pedestals as well as the distributions generated by proton and ^{3}He are due to target fragments.

to minimize blurring effects due to patient motion during transport and to biological patways wash-out of the produced isotopes.

The positive clinical impact of in-beam PET with ^{12}C ions has already been demonstrated at Gesellschaft für Schwerionenforschung (GSI, Darmstadt) by using a commercial PET scanner adapted to the purpose [35, 36, 27]. A brief description of this device, called BASTEI, can be found in section B.1. The method used at GSI to verify particle beam dose delivery is to simulate the PET isotope activation and the obtained image and compare it with the actual PET image [37].

Besides the already clinically operated in-beam PET tomograph at GSI or the post-irradiation (”off-beam”) usage of commercial full-ring PET or PET/CT scan-

ners [38, 39], new experimental planar positron cameras suited for in-beam installation have been recently realised at HIMAC [40, 41], Kashiwa [42] and Italy [43], and another one is under construction in France [44]. This thesis focuses on the Italian system, whose first prototype has been designed as an eye-therapy monitor device. The DoPET project (Dosimetry with a Positron Emission Tomograph) funded by the Istituto Nazionale di Fisica Nucleare (INFN, Italy) aimed to realize a dedicated, high-resolution in-beam PET system. Construction, calibration and preliminary testing of DoPET detector are reported in this work.

Since proton-beam installations are more numerous, our primary goal is to overcome the difficulties deriving from the poorer activity-dose spatial correlation for protons, in order to be able to use the in-beam PET technique in proton therapy. The same groups interested in carbon-therapy monitoring are working on this subject [5, 45, 6]. The validation of the first small prototype was performed at the INFN Laboratori Nazionali del Sud (LNS) using 62 MeV protons stopped in PMMA phantoms, and the expected range resolvability of about 2 mm has been achieved.

However, in perspective of a future application of the clinical version of the DoPET detector for all the relevant ion beam modalities, it is important to validate the performances of the system also for the increasingly considered carbon ion case.

Chapter 2

The DoPET project

The aim of the DoPET project (Dosimetry with Positron Emission Tomography) was the realization of a PET system dedicated to proton-therapy monitoring.

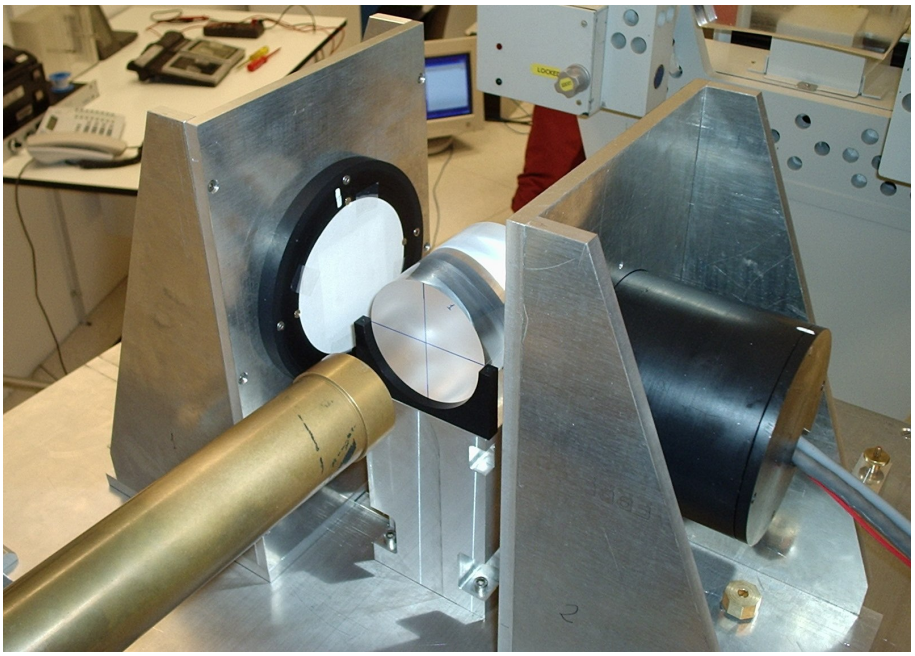

Figure 2.1: The installation of the experimental setup at the CATANA beam line. The brass nozzle is visible on the left, a cylindrical PMMA phantom is centered in the beam line, and the two detector heads are mounted at the phantom sides.

Such project is ongoing since the beginning of 2006 within an INFN collab-

oration, with the purpose of realizing a small prototype of a future clinical device. The system has been characterized at the laboratories of Pisa University - INFN, and validated through measurements on phantoms, at INFN-LNS (Istituto Nazionale di Fisica Nucleare - Laboratori Nazionali del Sud) in Catania, in the perspective of a future clinical application in tumour treatment monitoring at CATANA. The primary goal of this first stage was to reach a detection capability of deviations of the order of the millimeter for the proton range, i.e., only for one direction.

The essential elements of the detector are shown in figure 2.2, in the assembly adopted for the first test measurements. The tomograph consists of two planar heads, offering an active area of about 5 cm height x 5 cm width. In the final assembly two punched guides allows one to set the distance of each head at 5 cm, 7 cm, 10 cm and 15 cm from the center of the phantom undergoing irradiation. Distances have been chosen to be compatible with the purpose of investigating the application of the prototype for eye therapy monitoring.

For irradiations of about 15 Gy delivered within one minute on a volume of about 10 cm^3, in the clinical configuration of 20 cm distance between the detector heads, the tomograph provides a peak counting rate lower than 1000 events/s. By acquiring positron annihilation events over ten minutes, the resulting statistics is about 10^5 events.

By increasing the angular coverage, the statistics can be enhanced. At this stage, however, for cost reasons we have been forced to adopt an alternative solution to collect more statistics. We reduced to 14 cm the distance between detector heads, which approximately correspond to the same increase in geometrical efficiency that would have been obtained by doubling the detector size. The irradiation and acquisition times have also been extended, although this move us away from clinical situations where dose fractions are determined by therapy requirements, and patients cannot be kept immobilized for too long. The purpose of the experiment, however, is not yet to state the clinical performances of a dedicated PET device, but only to demonstrate the feasibility of the technique, which will be then refined (see chapter 8).

2.1 The tomograph architecture

Detector head The DoPET system consists of two planar heads. One head is made up of a squared position-sensitive photomultiplier (Hamamatsu H8500 [46]) coupled to a matrix of the same size of LYSO:Ce ($Lu_{2(1-x-y)}Y_{2x}SiO_5$:Ce_y,

$x \approx 0.1$, $y \ll x$) scintillating crystals ($2 \times 2 \times 18$ mm^3 pixel dimensions). Photomultiplier and crystal arrays have been glued together using thermoplastic Cargille Meltmount$^{\mathrm{TM}}$.

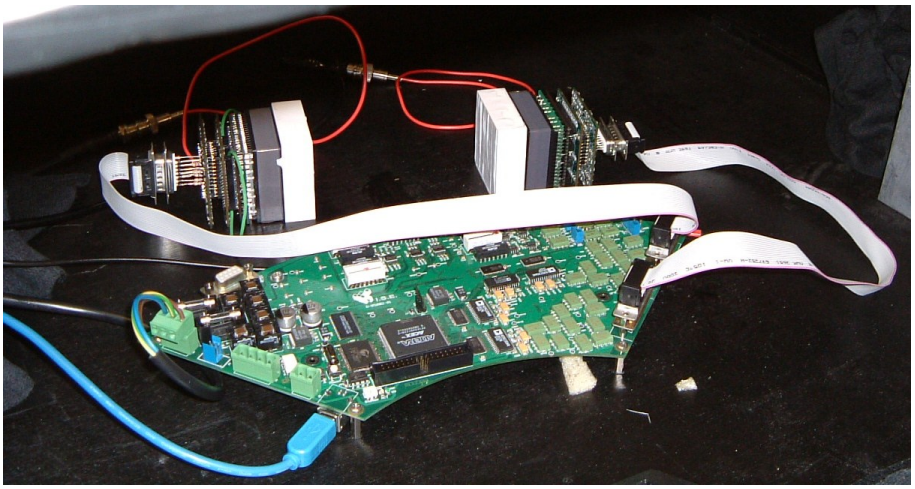

Figure 2.2: Raw materials used for the tomograph. The acquisition board and the USB connection are showed besides the essential elements of the detector heads, i.e., the scintillator arrays, the PMTs and the front-end electronics.

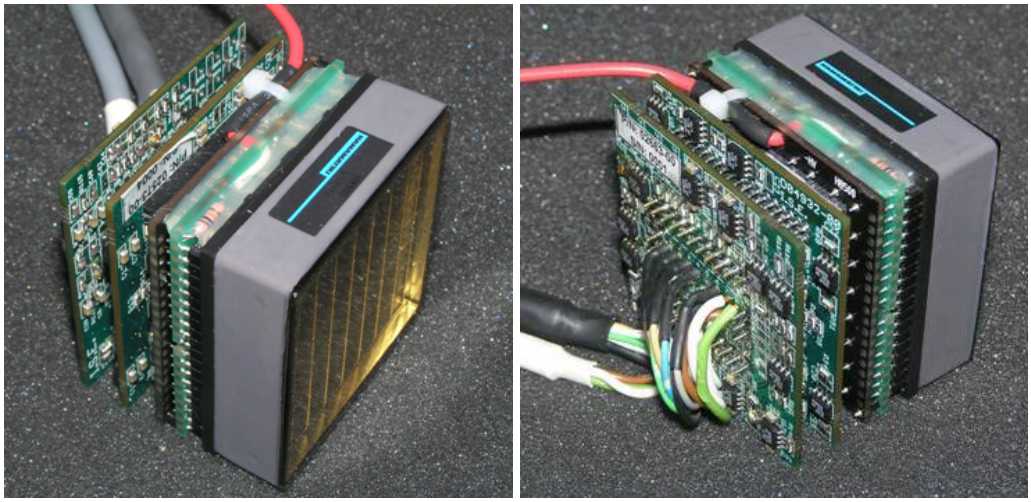

Figure 2.3: Front and back pictures of the Hamamatsu H8500 PMT assembled with the front-end electronics.

Hamamatsu H8500 PMT consists of a 12-stage metal channel dynode for charge multiplication and 8×8 anodes for charge collection and position cal-

culation. The external size is 52 mm $\times$ 52 mm $\times$ 28 mm and the active area is 49 mm $\times$ 49 mm.

Its choice satisfies also the requirements of modularity for the future extension to a larger device, made up of 2×2 PMT's for each head. In fact, this tube has a very compact size with metal envelope thickness of only 0.25 mm and it is designed to be assembled into an array to cover large detection areas, with an improved active area of up to 89%.

Each individual anode is 5.8 mm $\times$ 5.8 mm in size with a 0.28 mm inter-anode spacing, corresponding to an anode pitch of 6.08 mm.

It has been chosen to read out the multi-anode PMT through a multiplexed system mainly based on Symmetric Charge Division networks (SCD, see section 4.1 for details) which reduces to 2×2 signals the output of each tube. Dedicated, compact electronic boards are then used for the signal amplification and digitization. Thanks to the output data compatibility with older cross-wire style multianode PMTs, only minor changes are required for the connection to the data acquisition system that was originally developed for the small animal PET/SPECT scanner YAP-(S)PET [47].

The characteristics of scintillating crystals of the PMT and of the chosen front-end read-out will be described in more detail in chapter 4.

Acquisition system The scheme of the acquisition system for the PMT pair is shown in figure 2.4. As in the YAP-(S)PET scanner, the acquisition can be performed independently for the two heads (SPECT mode) or in coincidence (PET mode). The single-photon counting finds its utility in the phases of calibration of the electronics and characterization of the scintillating crystals. The last dynode output signals from the PMTs are amplified by fast, low-noise pre-amplifiers (the pre-amplification stage in figure 2.4) and sent to the board for fast timing coincidence when used in PET mode. A constant fraction discriminator (CFD) for each photomultiplier tube is used for amplitude independent timing in the time window generated by the gate. In SPECT, the output of each CFD directly generates the gate for the acquisition of the position signals. In PET mode, constant fraction discriminator outputs are sent to a coincidence module that produces a 10 ns gate signal. One of the CFD outputs delayed by 100 ns generates a delayed coincidence window. Events collected in this delayed windows in coincidence are random events and can be used to establish the rate of the randoms that affects the acquired data.

The four position signals from each tube are digitized by a system composed

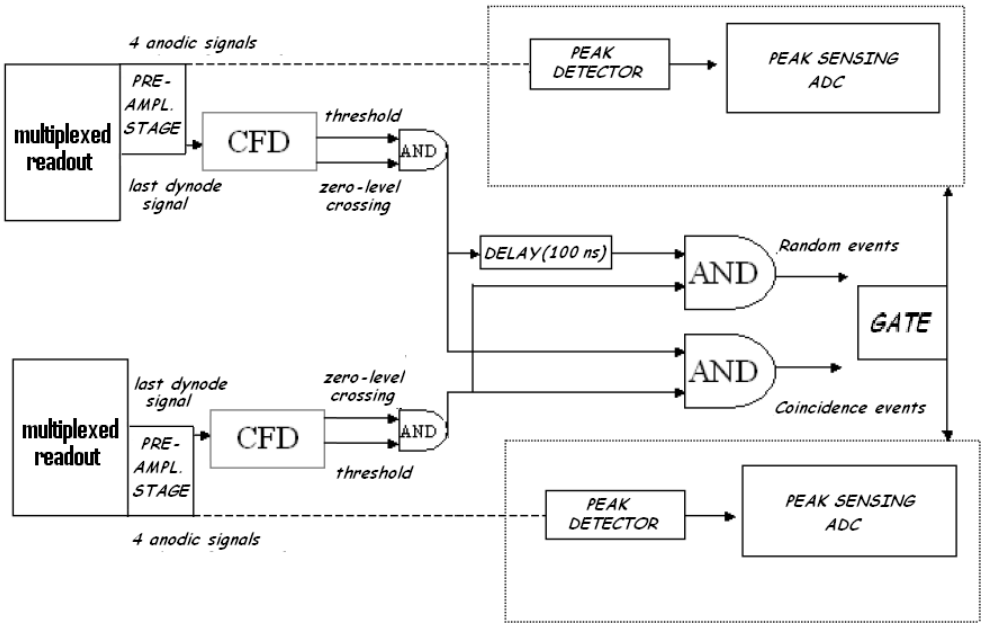

Figure 2.4: Schematic representation of the electronics for the data acquisition.

of a peak detector plus a peak sensing ADC. The digital data from both detector heads are then transferred to a local PC server and the point of interaction on the photocatode is then reconstructed off-line by software. When the acquisition system handles counts rate of the order of 300 kHz per head, the pile-up is about 15%. Coincidences cannot be efficiently acquired above 50 kHz. However, this is not a problem for this application, since typical coincidence rates during ”in-beam” measurements are of the order of one kHz or below.

The local PC server receives the acquisition data via USB2 connection. Remote-control of the acquisition is possible via LAN connection of a client PC to the primary one. During post-irradiation measurements at CATANA, the server PC has then been placed within the treatment room, and the acquisitions have been controlled from the beam-line control room.

From the YAP-(S)PET scanner we also inherited the graphic user-friendly interface, for the control of the acquisition and of the ”raw” analysis.

The raw spectra of each one of the four position signal and of the sum of them, as well as the map of events for each head can be generated. The possibility to select the raw ADC channel limits and to personalize the pedestal correction is foreseen.

The planar images of the event distribution on the detector area are derived through a center of gravity coordinate algorithm. A dedicated program tool helps then the calibration of the system by performing the crystal pixels identification on the planar images, and the energy calibration for the correction of the pixels gain the construction of the LUT (Look Up Table) variation.

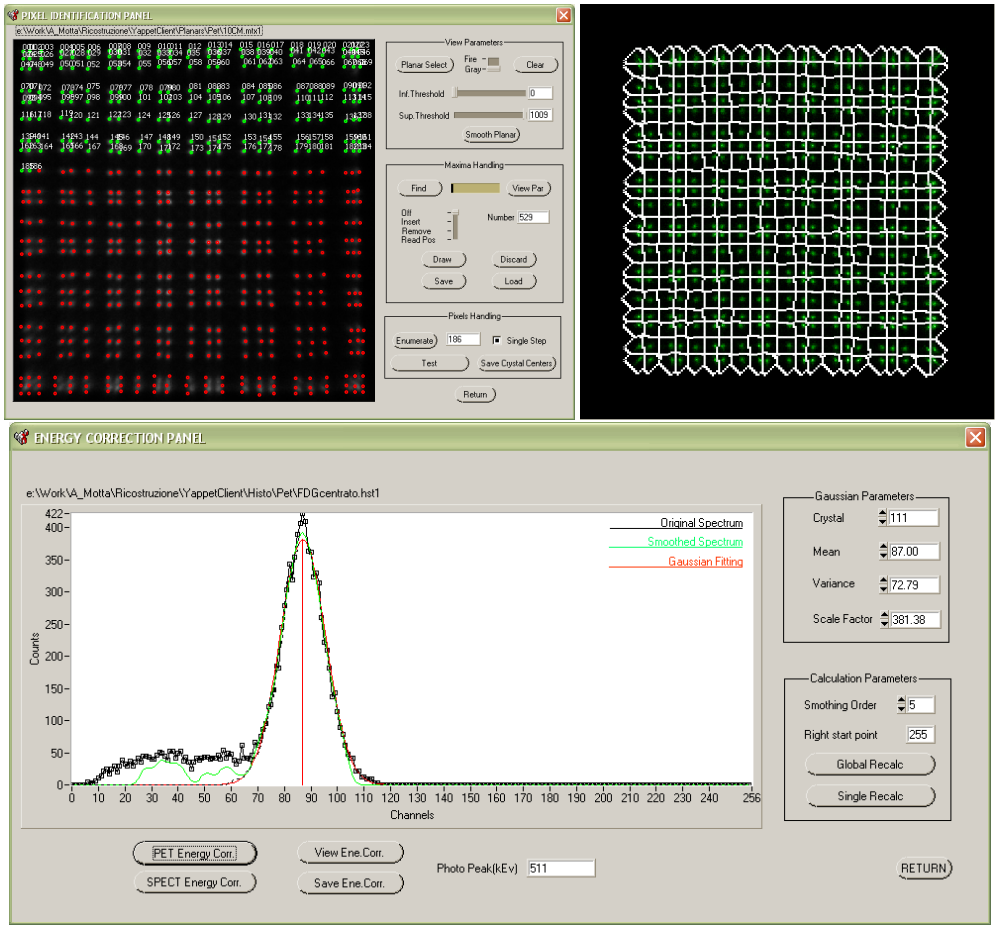

Figure 2.5: Examples of the output of dedicated DoPET software. Above, left: graphical interface of the pixel identification software, used to determine the pixel center of gravity and to assign the proper numeration. Crystal centers coordinates are then stored and used to build the map for assign each event to the right crystal pixel. Above, right: the grid used for event assignation to pixels is shown, superimposed to the planar image used to generate it. Below: a screenshot from the software used for energy calibration of single pixel spectra.

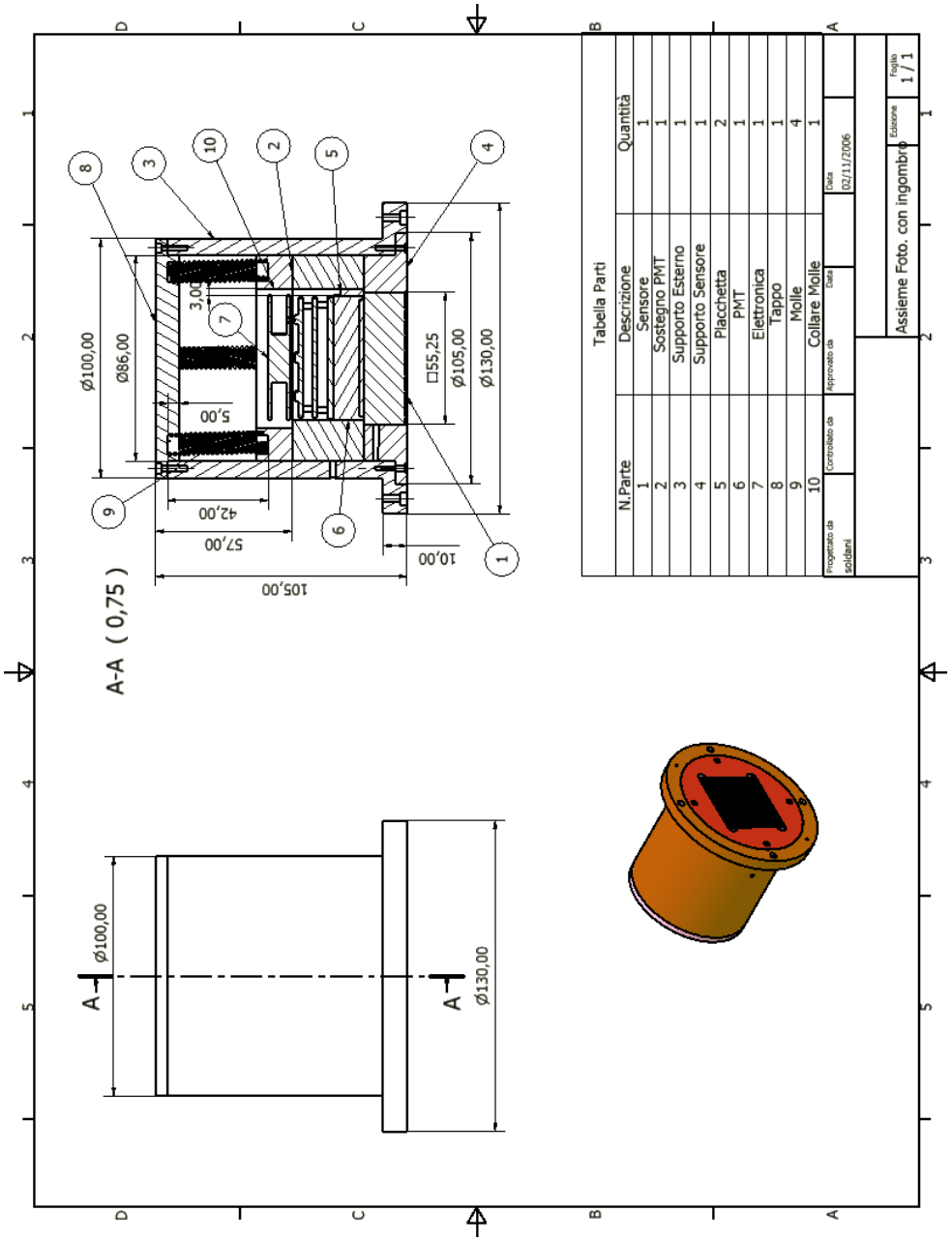

Figure 2.6: Mechanical design of one detector head. 1: scintillator crystal. 6: H8500 PMT. 7: front-end electronics boards.

Mechanical support A mechanical holder has been built in order to be able to position the detector heads with precision and reproducibility, both in the calibration and in the validation measurements. The main constituents of the detector head, i.e., the scintillator crystal, the PMT and the front-end electronics boards, are positioned in a cylindrical PVC envelope and fixed with the help of metal springs and teflon plaques. The mechanical design of the detector head is shown in figure 2.6.

Special attention was paid to position stability and reproducibility, and this allowed a reliable utilization of the system during the preliminary measurements, when optical grease was used to couple crystal and PMT, and the detector heads were often disassembled. The mechanical head frame has also provided a good support for the alignment of the elements during the gluing process. The cylindrical geometry of the head frame has been chosen for compatibility with a calibra-

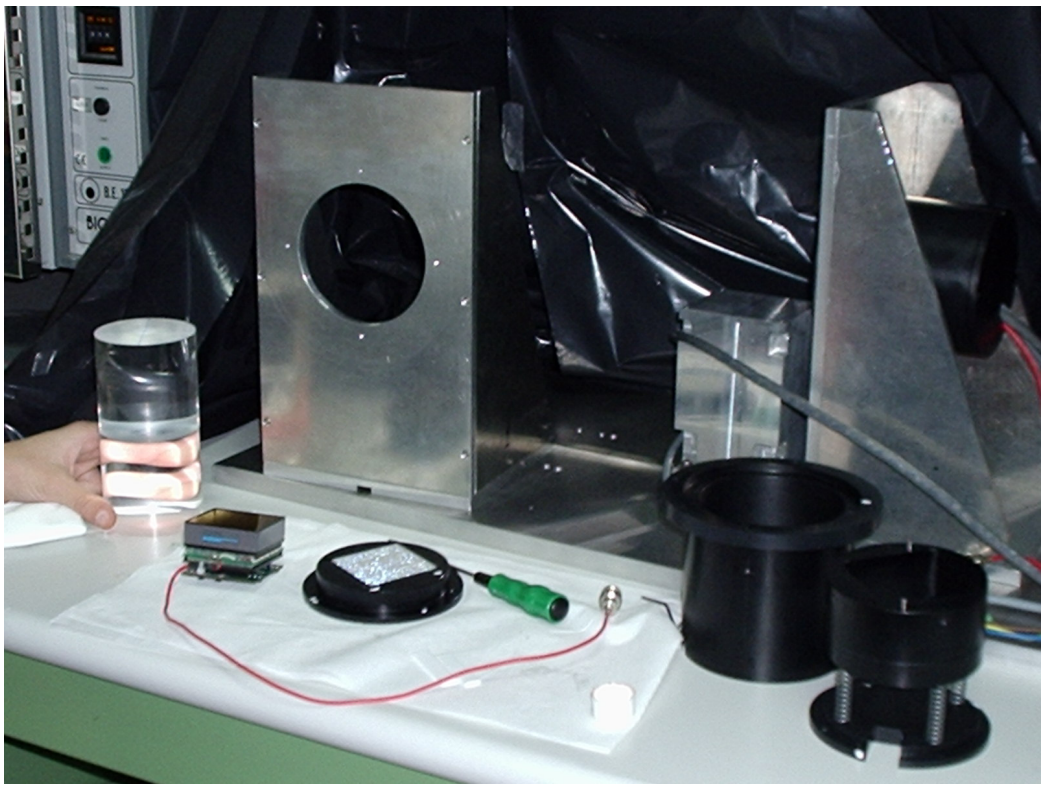

Figure 2.7: The detector components listed in figures 2.6 and 2.8 prepared for the assembly.

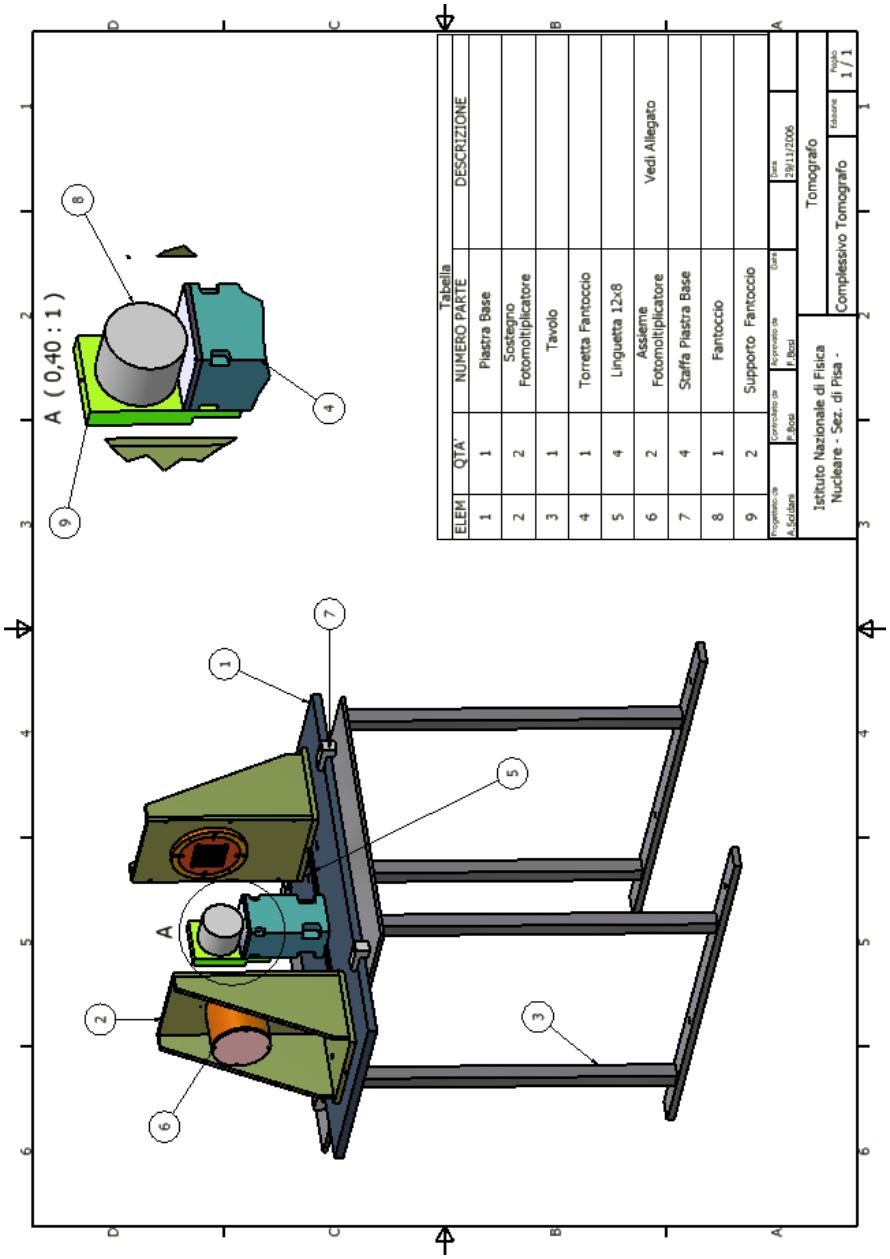

Figure 2.8: Mechanical design of the experimental setup. Details of element 6 (detector head) are reported in figure 2.6.

tion system that is being developed for evaluation of the spread in pixel sensitivity and PMT non-linearities.

The PVC frames are mounted on anticorodal supports, which allow the crystal matrices to be oriented within few mrads with respect to the vertical and horizontal reference planes. The anticorodal supports can then be placed on a anticorodal slab provided by a guide and reference holes, in order to center and align the detector heads at the chosen distance. Another anticorodal support can be mounted at the center of the slab, in order to place phantoms or point source frames at the proper height. The mechanical design of the entire apparatus is presented in figure 2.8. A picture of all the mechanical elements described above is shown in figure 2.7.

2.2 Radiation therapy for choroidal melanoma and CATANA project

Uveal melanoma is the most common primary intracular malignant tumor. Preservation of the organ and its function, as well as cosmetics, are important for patients diagnosed with it. Ophthalmologists are familiar with this disease entity, and several therapeutic options are available today in specialized centers [48]. Chemotherapy and hormonal therapy are primary treatment modalities used to control disseminated systemic disease [49]. If tumor progression, visual deterioration, or other significant ocular problems occur, subsequent local treatment may be necessary. For years, the standard form of local therapy was enucleation, but this has been replaced whenever possible by eye-"conservative" methods, such as brachytherapy, hadron (proton or helium ion) teletherapy, 4-6 MV photon teletherapy, local resection and transpupillary thermotherapy [50].

Radiotherapy is the preferred modality for local treatment of ocular tumors [51, 52]. The most commonly used forms of radiotherapy for local treatment of choroidal melanomas are ophthalmic plaque brachytherapy [1] and proton therapy: they can preserve or even improve visual acuity [53, 54], and can prevent enucleation for the rare patients with intractable pain [55].

With episcleral plaque therapy, radiation first travels through and is sequentially absorbed by the sclera, the tumor, the retina, the vitreous and finally by normal ocular structures as it exits the eye. Because radioactive plaques deposit most of their radiation within and around the tumor, and since most choroidal

[1] Using, e.g., ^{125}I, ^{106}Ru, ^{103}Pd or ^{192}Ir.

melanomas are found in the posterior pole, this may explain why radiation retinopathy may occur earlier after plaque therapy [56]. In fact, functioning of the eye is dose dependent for the critical structures of the posterior part of the eye, the fovea and the optic disc: radiation doses higher than 35 GyE to either one of these structures, mostly due to close tumor proximity, causes worse visual acuity after treatment [53].

When proton therapy was introduced in 1975, it was considered as a possible alternative to enucleation for large tumors that are unmanageable with brachytherapy. However, proton therapy allows for a homogeneous dose distribution within the whole tumor volume, and this has made the technique to be also considered as an alternative to brachytherapy for tumors located close to the optic disc or to the macula or both. In contrast to plaques, charged particle must pass through the lids, lashes, lachrymal system, conjunctiva, cornea, iris, lens, peripheral retina, vitreous, and the retina overlying the tumor prior to reaching a posterior uveal melanoma. Complications are then more often located in the anterior segment and are associated with pain.

As for the other conservative treatments, the aims of proton therapy in the management of uveal melanoma are, in descending priority, local tumor control and cure of the malignant disease, retention of the eye, and retention of a useful vision. Both local failure and complications led to subsequent enucleations.

Proton beam radiotherapy of uveal melanomas was first developed in Boston and is now performed in more than a dozen centers around the world [57]. Some centers use it for all patients; however, it is more expensive and time-consuming than brachytherapy and can also cause side effects in extraocular structures, such as eyelids, lachrymal gland, and the tear ducts.

In review of the literature on treatment of choroidal melanoma, there are not standardized methods of tumor classification, radiotherapy, or follow-up. Published accounts then largely represent anecdotal experience of individual investigators [58]. However, the main elements of the treatment procedure for proton therapy are always the same [58, 54, 59, 53, 60, 55, 61, 62, 63].

The patient is treated in the seated position, and the head is immobilized with an individually molded facemask and bite block. Eye gaze direction is established by having the patient look at a flashing light set at the position determined by the planning process.

Prior to treatment, tantalum clips (from 4 to 7) are sewn to the episclera around the base of the tumor in order to localize the targeted zone. These markers allow the radiation oncologist to radiographically locate the intraocular tumor with an anterior approach, and are not removed after the completion of the therapy.

The patients were asked to gaze at a small, red light positioned at the selected polar and azimuthal angles. When visual acuity impairment or field-of-view defect are present, patients had to fixate with the contralateral eye. Several candidate gaze directions are evaluated, from which the optimum was selected, that is, the one giving minimal radiation to optic nerve, lens, fovea, and lachrymal gland. Any visual limitations that might have prevented steady gaze during treatment is detected, and eventually a more suitable gaze direction is selected. After proper centering of the eye, orthogonal X-rays pictures were taken at each selected gaze direction. The coordinates of the eye center as well as the clips positions (i.e., tumor position) are transferred to the planning program, together with further information on ocular features.

Typical treatment margins include a 1 mm biological margin (for sub-clinical disease), plus a 0.5 mm patient movement allowance, plus 1 millimiter for the penumbral effect (the natural tendency of radiation to spread to the side, widening the beam portal) [58, 53]. However, the adopted safety margin ranges from 2 to 3 mm, and differences are mainly due to tumor location and to the variation in beam penumbra and distal fall-off measured in each center.

For the treatment, the portal beam is directed toward the patient's eye in line with the intraocular tumor as defined by the episcleral tantalum clips. Treatment portals vary from 10 to 35 mm in diameter, depending on the size of the lesion to be treated [60]. It must be also assessed whether to retract the eyelid or treat through the closed lid, in which case eyelid thickness and position were measured [60, 61]. Irradiation of the eyelid can be reduced or eliminated by lid retraction performed by the ophthalmologist. In fields without eyelid involvement, a lower distal margin is sometimes used [60]. The delivered dose ranges from 50 to 80 GyE, divided into a low number of daily fractions (from two to five). Irradiation time is few minutes per fraction.

CATANA The CATANA (Centro di AdroTerapia e Applicazioni Nucleari Avanzate) project [62] has developed a proton therapy facility to treat uveal melanoma, as well as less frequent lesions like choroidal hemangima, conjuntiva melanoma, eyelid tumors and embryonal sarcoma. The therapy facility has been realized starting from the 62 MeV proton beams from a Superconducting Cyclotron [10] at LNS, Catania (Italy). The project was born from the collaboration between Nuclear and Medical Physicists and Medical Doctors, and it is the first (and the only one, at present) Italian centre for the tumors treatment with hadrons.

All the informations obtained by diagnostic methods are elaborated by means

of three dimensional therapy planning program EYEPLAN, developed at the Massachussetts General Hospital for eye tumor therapy using proton beams. This software schematically displays a model of the patient's eye, including the lens, optic nerve and fovea, where the tumor is finally drawn by means of the specified measurements and position reference. Proton beams irradiate eye tumor, usually sparing optic nerve and optic disc.

So far, 141 patients coming from different Italian regions have been treated since February 2002. Follow-up data for 103 patients after at least one year after their treatment confirm the effectiveness of proton therapy (70% of patients show a tumour reduction and 96% of patients show a local control of the tumour). However only 40% of the patients maintains a good visual acuity [64].

In-beam PET and uveal melanoma The adoption of a monitoring technique as the in-beam PET does not appear strictly necessary in case of proton therapy of uveal melanoma, since we are dealing with a well established tecnique. However, sometimes a rigorous comparison of results from one center to another can be difficult and an additional device for treatment monitoring could help to refine the therapy protocol "ad-hoc" for each beam facility.

Risk factors for local tumor control failure related to the treatment procedure have been identified as a reduction of the safety margin, the presence of an eyelid within the irradiation field and an inadequate delimitation of the tumor border by tantalum clips [60, 65]. Therefore, only some specific topic, such as uncertainties related to eye-movement and presence of eyelids in the irradiation fields, could be further explored with the help of the in-beam PET. It is not believed that this technique will produce a benefit in eye-therapy monitoring when applied to an individual patient, but rather if it is adopted as a method of investigation to improve the evaluation criteria of the safety margin[2], so as to lower the risks of failure in tumor control or of post-irradiation sight-limiting side effects.

2.2.1 The proton beam line at CATANA

The complete layout of the CATANA proton-therapy beam line is shown in figure 2.9. A schematic representation of the main beam line elements is given in figure 2.10.

The accelerated proton beam exits in air through a 50 μm Kapton window placed at about 3 meters from isocenter. The first scattering foil, made of a 15 μm

[2]Reducing or more likely extending the margins presently adopted.

Figure 2.9: View of the treatment room at CATANA. For measurements on plastic phantoms the chair shown in the figure is replaced by the aluminum table shown as element 3 in figure 2.8.

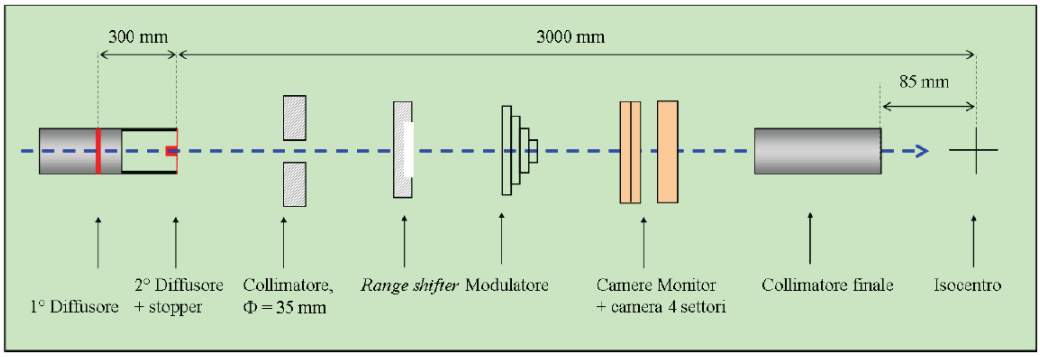

Figure 2.10: Schematic diagram of the beam path through the treatment line.

thick tantalum, is positioned before the exit window, under vacuum. The first element of the beam in air is a second tantalum foil of 25 μm thickness provided with a central brass stopper of 4 mm in diameter. The double foils scattering system is optimized to obtain a good homogeneity in terms of lateral dose distribution, minimizing the energy loss.

The selection of a specific proton beam energy with a correct energy modulation requires two devices: range shifter and range modulator. The former (a block of material of defined thickness) degrades the energy of the primary beam by a fixed quantity while the latter (a rotating wheel with various steps of increasing thickness) produces a spread out in the energy of the Bragg peak.

Two transmission monitor chambers and four sector chambers have the on-line control of the dose delivered to the patients and of beam symmetry, respectively.

The last element before isocenter is a patient collimator located at 8.3 cm upstream of the isocenter. The system for the isocenter identification and for patient centering during the treatment consists of two diode lasers, placed orthogonally. The emission light of a third laser is spread out to simulate the treatment field.

Two Philips Practics X-Rays tubes are used for the verification of the treatment fields: one is mounted on the back and the other at one side of the patient.

During the treatment phases, patients are immobilized on a chair, whose position is computer controlled. For test measurement in phantoms, the chair is removed and an aluminum support (element 3 in figure 2.8) is placed on the computer-controlled motors.

The dose measurements are performed in a water phantom, according to International Atomic Energy Agency Technical Report Series (IAEA TRS) 398 Code of practice. For such measurements the patient collimator is substituted with a 25 mm diameter circular brass collimator (reference collimator). A parallel-plate Advanced PTW 34045 Markus® ionization chamber is the reference detector for the absolute dose measurement, while gaf-chromic and radiographic films, thermoluminescent detectors, natural diamond and silicon detectors are used for the relative dosimetry, i.e., for three dimensional dose distribution reconstruction.

Depth dose curves and transverse dose distributions, either for the full energy and modulated proton beams, are acquired with a water-tank system provided of three fully computer-controlled step motors. A software, entirely developed at INFN-LNS, controls this system and provides the acquisition and dosimetric analysis data. Figure 2.11 shows a transversal and depth dose distributions obtained with the water-tank system.

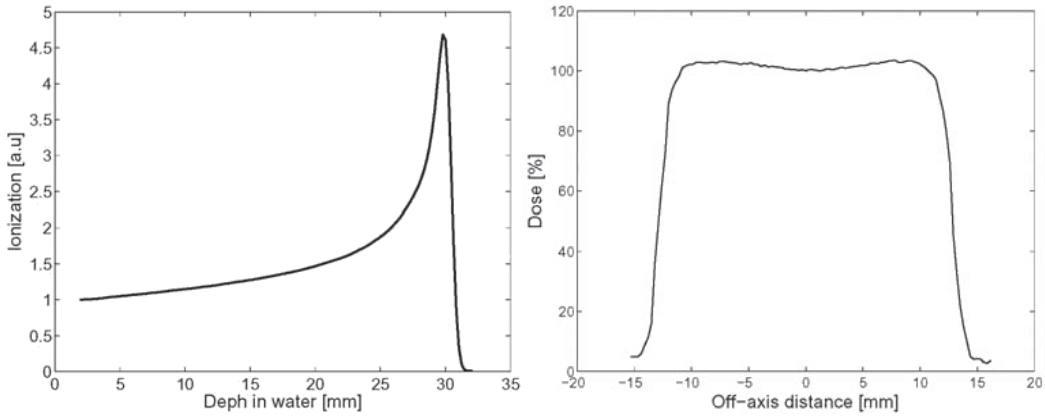

Figure 2.11: Dose profiles in the water-tank of proton beam at the energy of 62 MeV using 25 mm diameter circular brass collimator. Left: Longitudinal dose profile obtained with the Markus chamber. Right: Transversal dose profile obtained with silicon diode at at the treatment depth of 12 mm, corresponding to the middle of a Spread Out Bragg Peak (SOBP).

Chapter 3

Prediction of the detector performances

The Monte Carlo simulation is useful for the optimization of the detector design and for the generation of data to be used in the validation of the reconstruction algorithm. However, we will see in this chapter that Monte Carlo has not been the chosen solution for all the applications.

The evaluation can be splitted into four topics: the proton phase space produced by the CATANA beam line for each specific configuration, the 3D dose distribution delivered to targets, the 3D activity distribution induced by irradiations and the efficiency and the spatial resolution of the PET detector.

Regarding the detector simulation, a detailed representation of the DoPET device has been developed [66] with the SimSET [67] package. The proper active scintillator volume has been simulated, however no simulation of the reflecting material nor ^{176}Lu decays have been introduced. Typical LYSO characteristic parameters have been used and energy resolution of 15% at 511 keV has been assumed for both detector heads, on the basis of some preliminary measurements. The energy resolution obtained in the final setup is consistent with such estimate (see section 6.1). Three different head-to-head distances have been simulated, corresponding to positions that can be selected with the mechanical assembly. Due to differences in the geometry of pixel displacement (21 x 21 pixel with no dead space, i.e., 42 mm $\times$ 42 mm instead of 45 $\times$ 45 mm) with respect to the actual configuration, the simulation should provide an under-estimate of detection efficiency and an over-estimate of spatial resolution. Results are presented in chapter 6, and discussed after comparison with experimental data.

Irradiations of PMMA ($(C_5H_8O_2)_n$, ρ = 1.19 g/cm^3) and of tissue phantoms

must be simulated with proton beams in the energy range of 50-70 MeV, used in the treatment of ocular carcinomas at Catania. A theoretical comparison of activity and dose profiles for each configuration would provide a method to extrapolate dose distributions from activity ones.

Concerning the knowledge of the phase space of each proton irradiation, we have used the `Hadrontherapy` routine [68], developed by the GEANT4 collaboration to simulate the CATANA beam line. The routine is well described in section 3.1 and perfectly fits our requirements. The CATANA group kindly provided our collaboration with the results of the desired simulation, thus allowing us to spare simulation time.

In order to propagate the proton phase space into the target volume, so as to reproduce dose and activity distributions, the `Hadrontherapy` program would need to be refined, concerning the hadron inelastic processes. Although some small uncertainties in hadron inelastic physics do not produce significant changes in the dose distribution within the target, these could affect the results so that the required precision for evaluating the isotope-production distribution is not reached.

Attempts to adapt the `Hadrontherapy` for the prediction of activity distribution are presented in section 3.2. However we finally decided to adopt a semi-analytical approach, which is much faster than a GEANT4 based Monte Carlo, and is based on experimental cross sections rather than on theoretical models. The final method is described in section 3.3.

3.1 The `Hadrontherapy` routine

GEANT4 is a Monte Carlo simulation tool [69]. It is not a stand-alone executable but a toolkit of libraries; it was designed and developed by an international collaboration, formed by scientists from a number of cooperating institutes involved with High Energy Physics, space and medical experiments.

`Hadrontherapy` C++ code is provided with GEANT4 as an advanced example [70] of an application using the GEANT4 libraries. It allows the user to simulate the complete proton therapy beam line and to generate all the dose distribution curves of the possible beams.

In the application, all the elements of the CATANA transport beam line for proton therapy are defined, from the beam exit in air up to the isocenter. Such elements are the scattering and collimator system, the monitor chambers, the range shifter, the modulator wheel, the final collimator.

As a default, a water phantom, $40 \times 40 \times 40$ cm^3 in size, is placed in the isocenter. The loss of energy is sampled in detail (0.5 mm voxel side) only in a $4 \times 4 \times 4$ cm^3 block, which totally contains the 70 MeV proton range in the phantom. The absorbed energy profile is then stored into a text file.

It is possible to choose the characteristics of the incident beam: beam energy, energy spread, beam spot size and angular spread. One can also choose to simulate the whole beam line, or to start the simulation from the final collimator (using experimental data or previous simulations as input for the beam parameters).

Two different detectors can also be simulated: a Markus chamber (for the depth dose curves reconstruction) and a Gaf-Chromic film (for the lateral dose distributions). Validation tests have been performed for simulated depth and lateral dose on the basis of the experimental data acquired at the CATANA proton therapy facility.

As far as the physics processes are concerned, the best combination with reproduce the experimental dose profiles is described below.

The energy loss and straggling of primary and secondary charged particles due to interaction with atomic electrons is described via a set of models called Low Energy Electromagnetic Physics. The standard processes, which are optimized for high energy physics applications, rely on parameterizations of atomic shell cross section data. Because atomic shell structure is more important in most cases at low energies than it is at higher energies, the low energy processes make direct use of experimental data. The low energy processes include the photo-electric effect, Compton scattering, Rayleigh scattering, gamma conversion, bremsstrahlung and ionization. Multiple scattering due to electromagnetic interactions with atomic nuclei is also included in simulations. Fluorescence of excited atoms is considered. The energy range covered by the data libraries extends from 100 GeV down to 1 eV for Rayleigh and Compton effects, down to the lowest binding energy for each element for photo-electric effect and ionization, and down to 10 eV for bremsstrahlung.

Two kinds of nuclear interactions are considered: elastic scattering of projectile hadrons or nuclei on target nuclei, which dominate at low projectile energies, and inelastic nuclear reactions induced by fast hadrons and nuclei. The overall probability of nuclear interactions for nucleons and nuclei propagating through the medium depends on the total inelastic cross section for proton-nucleus and nucleus-nucleus collisions. Parametrized equations by Wellisch and Axen (1996) that best fit experimental data were used to describe the total reaction cross sections in nucleon-nucleus collisions. Systematics by Tripathi et al (1997) and Shen et al (1989) for the total nucleus-nucleus cross sections were used for calculating

the probability of nucleus-nucleus collisions. The inelastic interaction of nucleons below 20 MeV is simulated by means of data-driven models. Above 20 MeV the exciton-based precompound model is invoked for both neutrons and protons. For bibliography reference and more details, see [71]. Any of the de-excitation models of the compound nucleus available in GEANT4 can be selected with negligible differences in the computed dose distribution.

3.2 The `DoPET-Hadrontherapy` routine

The first change applied to the program has been the introduction of a more extended and optimized storage of simulation results. ROOT libraries [72] has been chosen as analysis toolkit. Two objects are inherited from `TTree` ROOT class for the storage of information. The ROOT "tree", similar to the HBOOK ntuple, offers data storage as single variables, arrays or even more complex objects, with a minimal memory occupation thanks to the good compression of binary ROOT files and an optimized data access.

The objects architecture is reported on table 3.1. The necessity of two independent tree structures arises from the different structure of dosimetry and activity information. While data of unstable isotope produced by the simulation need to be

`TTree` DoPET_ion			`TTree` DoPET_en		
`int`	ev_id	# of the parent proton track	`double`	X_bin	coordinates of bin, in the same axis reference of isotope production
`int`	nZ	Z of the unstable atom			
`int`	nA	A of the unstable atom	`double`	Y_bin	
`double`	x	point of production of the radioactive isotope			
`double`	y		`double`	Z_bin	
`double`	z				
`double`	t	time of production (from the start of simulated irradiation)	`double`	E_dep	bin energy deposit (MeV)

Table 3.1: Architecture of the classes DoPET_ion, which collects information of each radioactive isotope production, and DoPET_en, which stores dose distribution in the phantom.

individually available, we are interested only in the total energy deposition in each phantom voxel. In principle, the $80 \times 80 \times 80$ voxels dose information does not

need the complex tree architecture. However this choice simplifies a simultaneous activity and dosimetry analysis.

The main improvement to be done is the adaptation of the hadronic inelastic processes combination used within the simulation. Although the inclusive hadronic inelastic cross section are parametrized from experimental data, in GEANT4 the evaluation of the branching ratio for the single channels are extracted through theoretical models which can be selected by the user. For beam energies around tens of MeV this approach does not seem accurate enough; the excellent results obtained by the GSI group with FLUKA [73] should be our final goal in terms of accordance with experimental data.

3.2.1 Hadronic physics in Geant4

Although the default selection of physics processes well fits the dosimetry simulation, a more refined "physics list" is required to simulate a realistic distribution of β^+ emitters after proton irradiation.

In this section there are described the main features of the framework adopted in GEANT4 for the simulation of the hadronic interactions. More details about the hadronic inelastic processes, as well as a description of the main models implemented in GEANT4, are available on appendix A.

Geant4 requires the user to decide which particles are needed for a given application, which physics processes are to be assigned to each particle, what the secondary particle production cuts are (electromagnetic processes only). It is left to the user to choose the proper combination in the specific case.

Each model has an intrinsic range of applicability, and the models chosen for a simulation depends very much on the use-case. Consequently, there are no "defaults".

Geant4 Hadronic Physics offers both parameterisation-driven models and a variety of theory-driven models. A summary of the available models depending on the energy range is shown in figure 3.1.

Data driven models are available only for low energy neutron transport from thermal energies to 20 MeV.

For particles in flight, two sets of parametrized models exist for inelastic scattering: low energy (LEP, below 20 GeV), and high energy models (HEP, to TeV energies). Both sets are based originally on the GHEISHA package of Geant3.21, and the original approaches to primary interaction, nuclear excitation, intra-nuclear cascade and evaporation is kept. Fission, capture and coherent elastic scattering are also modelled through parametrised models.

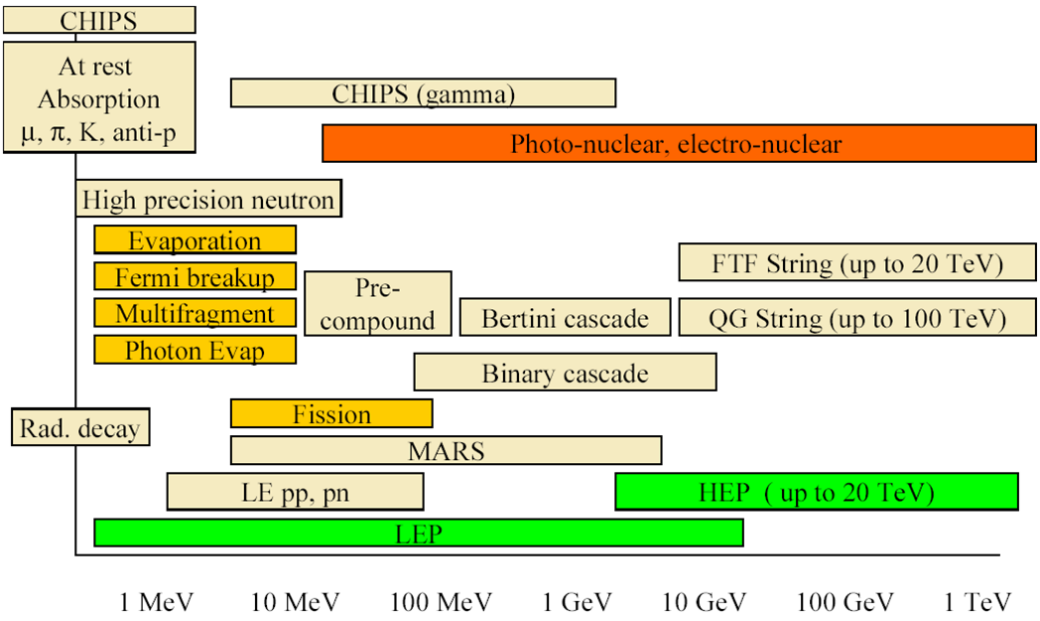

Figure 3.1: Geant4 Hadronic Physics Inventory.

Theory driven models are available for inelastic scattering in a first implementation. The current philosophy implies the usage of parton string models at high energies, intra-nuclear transport models at intermediate energies, and statistical break-up models for de-excitation.

Several models can be run together and their (geometrical and energetic) ranges of applicability can be steered at initialisation time. In this way, highly specialised models can be used in the same application, together with a more general code, in a coherent fashion. Although each model can be selectively applied to a specific geometrical region or to a particular incident particle, it is worth noticing that no selection can be applied for the target element nor for the reaction products. This turns into a strong limit for the application to our field of interest. In fact, as it is shown below, the limits of GEANT4 models are just on the division of the proton inclusive inelastic cross section into the single production channels. FLUKA users significantly improved the calculation of the isotope spatial distribution by combining the interpolated energy-dependent experimental cross-sections with the energy and position-dependent proton flux given by the FLUKA internal models [6]. User defined data driven model can be also introduced in the simulation. However, since only inclusive cross section can be modified, no

significant improvement can derive by the use of experimental cross sections.

All the efforts for Monte Carlo optimization were then focussed to find the model combination that best reproduce the cross sections of the production channels of interest for the "in-beam" PET.

3.2.2 Customization of the hadronic "Physics List"

The best combination of hadronic physics models which GEANT4 can offer for the simulation of target activation from 62 MeV protons is listed in table 3.2, following GEANT4 nomenclature. A description of each of the listed model can be found in section A.2, based on the Geant4 Physics Reference Manual and the related literature [71, 74, 75].

Only one main process has been added to the physics list described for the `Hadrontherapy` simulation. For hadrons and nuclei with the energies above 50 MeV, the binary cascade model (Folger et al 2004) has been employed. Excited nuclear remnants are created after the first cascade stage of interaction. The exciton-based precompound model and de-excitation models are then invoked as before. The preferred de-excitation models are the so-called "default Evaporation" and "Multi Fragmentation".

Particle	Model	Energy range validity
p, n, $\pi^{\pm,0}$	PreCompound + default Evaporation + Multi Fragmentation	0 eV - 170 MeV
p, n	Binary Cascade Model	0 MeV - 10 GeV
neutrons	Fission and Hadron Capture	0 eV - 100 TeV
^{2}H,^{3}H,^{3}He,^{3}He	LEP	0 eV - 100 MeV
^{2}H,^{3}H,^{3}He,^{3}He	Binary Ion Model	80 AMeV - 10 AGeV
ions	Binary Ion Model	0 AMeV - 10 AGeV

Table 3.2: Summary of hadronic inelastic processes enabled in the presented simulations. The energy ranges shown are the defaults of GEANT4, not the ranges used in our simulations.

The optimization of inelastic proton physics is the most challenging task. The development of such models is only at the beginning and no definitive validation is available. Therefore, the physics reference manual cannot offer a clear solution

for a correct selection of the physics processes to be activated, and even the energy range of validity is not completely clear.

Moreover, experimental data can be used in the simulation only for the inclusive proton cross section, while the single-channel probabilities are extrapolated at run time for each event in an implicit way.

For a better evaluation of the models, we settled a rough simulation of proton irradiation on thin targets of specific materials, and we used the simulation as an experimental setup to extrapolate the values of the cross section of interesting channels as inferred in the program by the model. Since we are mainly interested in the production of ^{11}C and ^{15}O, we simulated 2 mm targets of polystyrene and water, for evaluating ^{12}C(p,pn)^{11}C and ^{16}O(p,pn)^{15}O cross sections, respectively.

The cross section values have been extrapolated by using the formula:

$$\sigma[barn] = \frac{N_\beta}{N_p} \frac{1}{f_{comp} \cdot \rho_{target}[mol/cm^3] \cdot s[cm] \cdot N_A/10^{24}}, \tag{3.1}$$

where N_p is the number of simulated protons, N_β is the number of produced ^{11}C (or ^{15}O), ρ_{target} is the mole density in the target material, s is the target thickness, N_A is the Avogadro number, f_{comp} is the fraction of ^{12}C (or ^{16}O) atoms in the target molecule.

The experimental data used for comparison are reported in [76][1].

For each cross section value, 10^6 protons have been simulated, with a gaussian distribution (200 keV of r.m.s.) around the selected mean energy. Statistical errors on the cross section calculations are then extimated always lower than 5 mbarn.

The most critical parameters for an optimization of the simulation results are the width of the energy range superposition between precompound and binary cascade models, and the maximum atomic number allowed for the Fermi break-up fragmentation.

The precompound model alone produces cross section values always lower than 40 mbarn for ^{11}C and lower than 60 mbarn for ^{15}O. The binary cascade model, which is valid only above 15-70 MeV [74], reproduces the experimental data only at energies higher than 45 MeV for ^{11}C. In the same range, however, it overestimates the ^{15}O cross section.

In figure 3.2 are reported the extrapolated cross sections for minimal overlapping of models (only at 45 MeV).

[1] We remark that several sets of input nuclear reaction cross section data are available in literature, but they are significantly different from each other [77]. Therefore, no quantitative comparison will be presented in this chapter.

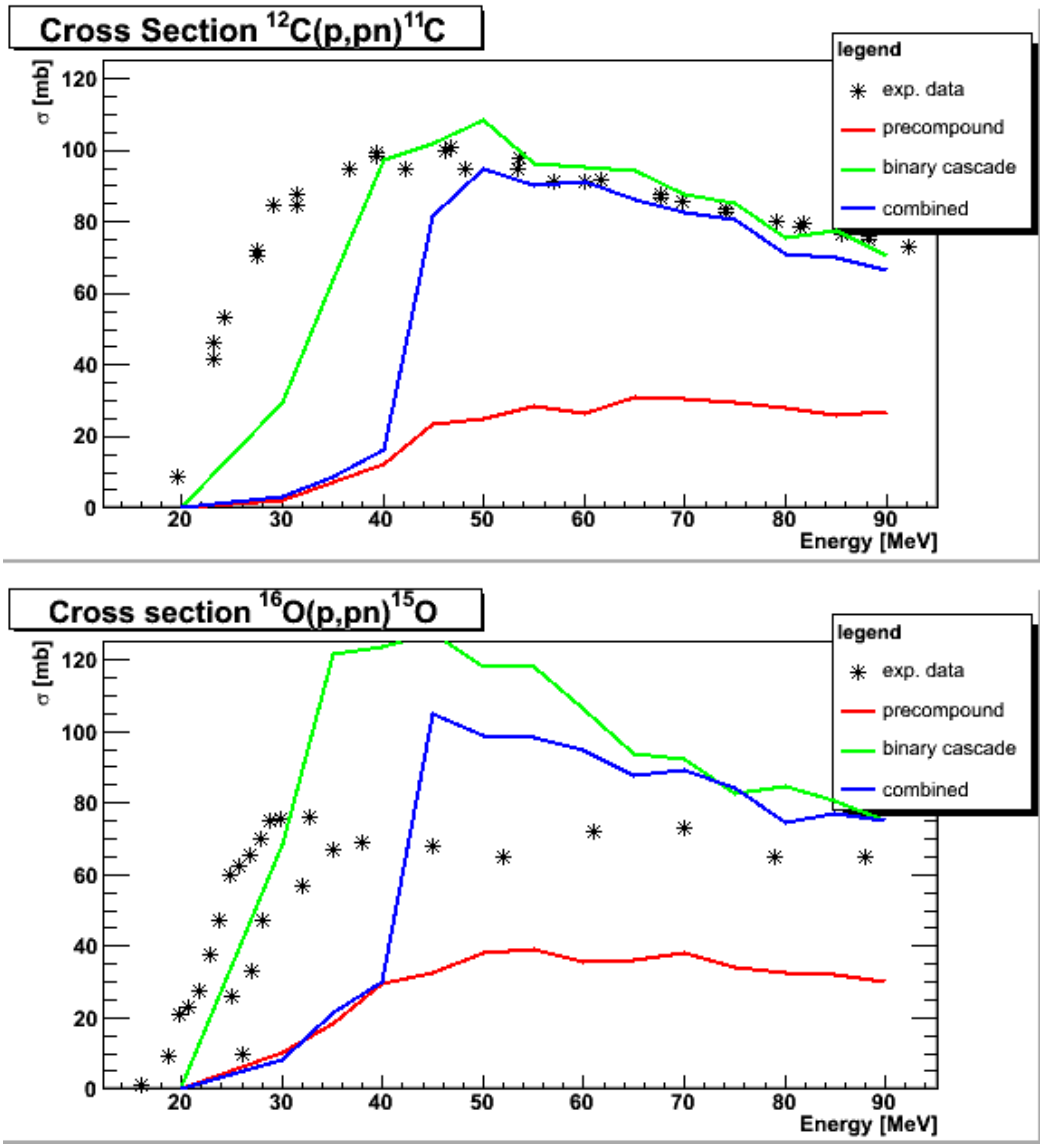

Figure 3.2: Extrapolated cross section for the main reaction leading to ^{11}C (top) and ^{15}O (bottom) production. Green line is a simulation with no binary cascade activated. Red line is a simulation with no precompound activated, but the binary model includes in itself a default precompound at low energies. Blu line is the simulation with the same physics list of table 3.2. Dashed lines delimits the range of experimental data available from [76].

For a process at energy x contained in the overlap interval $[a, b]$ of the energy ranges, the model used is randomly selected as $\frac{b-x}{b-a}\%$ of the model at low energies and $\frac{x-a}{b-a}\%$ of the other one. The passage between models results then "smoothed". Such smoothing would be useful for oxygen, but it is detrimental in carbon where it degrades the good results above 40 MeV. Differences between precompound and binary models below that energy are negligible.

The compromise is not satisfactory. In fact, if a simulation on a PMMA phantom is considered, only the total amount of each β^+ emitter is almost correct, while the wrong energy dependence in the simulated cross section leads to a wrong distal edge of the linear density profile of the isotope production. This would exclude the possibility of a correct correlation between activity and dose distribution.

Looking for a better solution in the low energy range, we studied in details the effect of "switching on" the Fermi Break-Up during Evaporation. By varying the maximum Z and A allowed for the compound atom, we obtained significative changes in the interested range (figures 3.3 and 3.4). A slight increase in low-energy production of the observed isotope is registered each time the parameters Z_{max} and A_{max} of the Fermi Break-Up are equal to the data of the parent compound nuclei (Z+1 and A+1, i.e., the parent isotope plus the impinging proton); in other words, each time the Fermi Break-Up is actually activated for the specific isotope. Since one would like to activate the Break-Up for all the tissue elements, we should set Z_{max} and A_{max} to their theoretical maximum, i.e., Z_{max}=9 and A_{max}=17. However, as can be seen from figure 3.3, a low-energy overproduction of ^{11}C (^{15}O) is then observed when Z_{max} and A_{max} of the compound nuclei enable the β^+ emitter production through the emission of an alpha particle. An overproduction of alpha particles is actually detected in the simulations. Due to the target composition used in simulation (see page 3.2.2, however, one should remember that in principle the compound nucleus cannot be different from (Z_{target}+1,A_{target}+1), therefore all the Z_{max} and A_{max} values higher than this should produce the same result.

The theoretical limits of the model set A_{max}=17 as the maximum mass number allowed, therefore the simulation with $A_{max} > 17$ presented here have not a rigorous explanation and are shown only for sake of completeness. Discussion with the GEANT4 Hadronic Physics group is still ongoing for a better understanding of the results.

In summary, to take into account the Fermi Break-Up for ^{12}C+p reactions, the setting Z_{max}=7 A_{max}=13 would be enough. If we want to take into account the

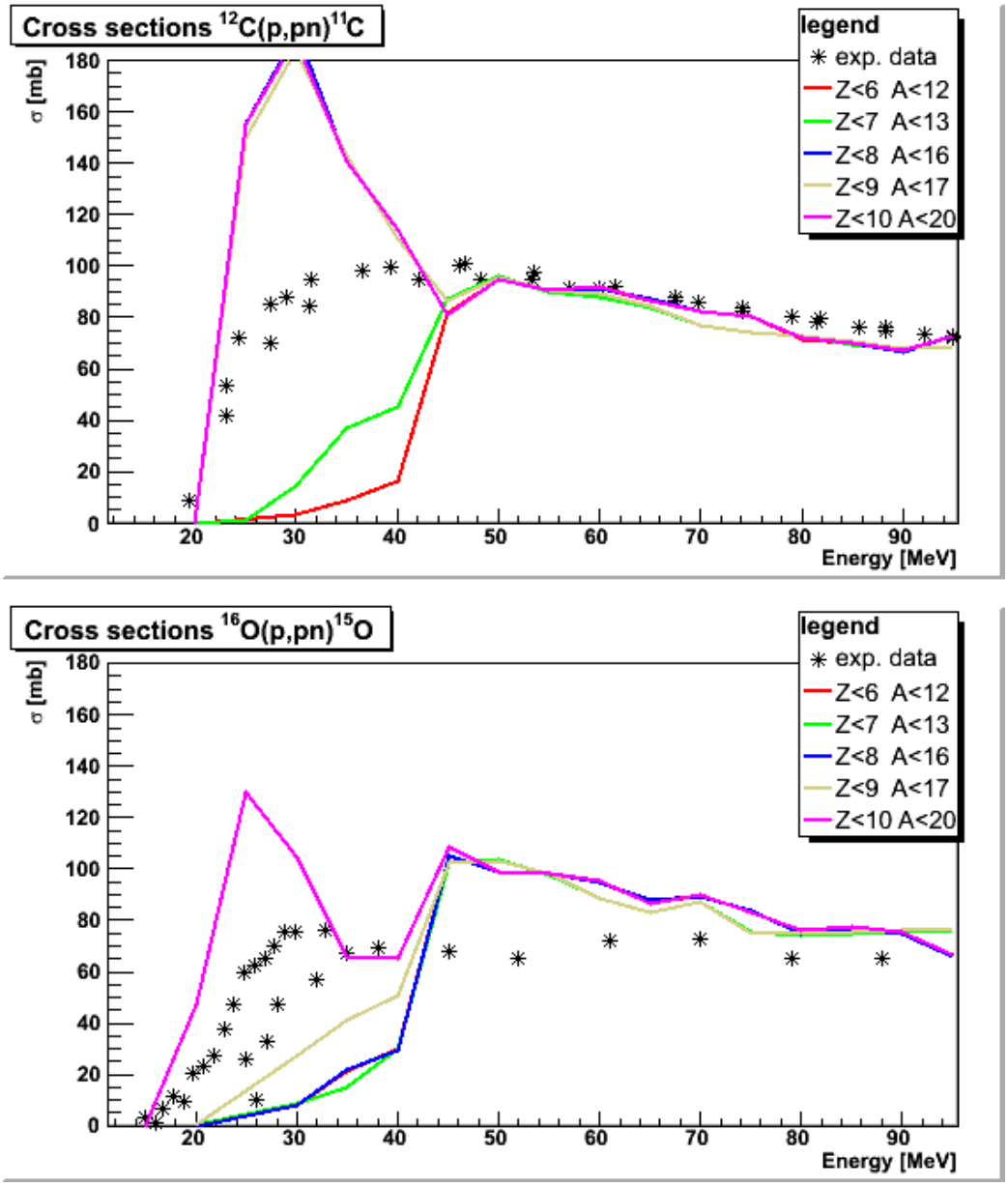

Figure 3.3: Extrapolated cross section for the main reaction leading to ^{11}C (top) and ^{15}O (bottom) production. Different colours correspond to different maximum Z and A allowed for the Fermi Break-Up in the target, as listed in the legend. Dashed lines delimits the range of experimental data available from [76].

Fermi Break-Up for ^{16}O+p reactions, we need to set Z_{max}=9 and A_{max}=17. This second setting, however produce an unexplained change in the ^{12}C(p,pn)^{11}C cross section, with dramatic effects on the ^{11}C density profiles (see figure 3.4). With the help of energy range overlap, the cross section curves can be smoothed, but not enough to produce good results.

3.3 Semi-analytical model

This second approach is based on the numerical integration of a Fokker-Plank equation for the longitudinal propagation of the proton energy distribution $f(E, z)$ through the matter:

$$\frac{\partial f}{\partial z} = \frac{\partial}{\partial E}[A(E)f] + \frac{1}{2}\frac{\partial^2}{\partial E^2}[D(E)f]. \tag{3.2}$$

The drift term $A(E)$ of the equation is the Bethe-Bloch (and Ziegler) parametrization of the stopping power for charged particles in matter, while the diffusion term is taken from the Vavilov theory [78].

Factorizing the problem into the evolution of the central axis and the lateral spread, it is possible to obtain a rather complete description of the effects the proton beam produces in the phantom. However, we will see later than only the axial dose and activity profiles is used in our analysis algorithm, therefore only the central axis evolution will be here presented.

Regarding the β^+ emitters density profile, this can be then obtained by a numerical integration of the experimental cross sections for each specific (interesting) reaction with the calculated $f(E, z)$:

$$\frac{dN^{react}}{dz}(z) = N_p(z) n_{el} \int_0^z \sigma^{react}(E) f(E, z) dE, \tag{3.3}$$

where n_{el} is the specific atomic density for the element el in the target, and $N_p(z)$ is number of protons at the depth z, calculated from:

$$\frac{dN_p}{dz}(z) = -N_p(z) \sum_{\substack{target \\ elements}} n_{el} \int \sigma_{el}^{tot}(E) f(E, z) dE. \tag{3.4}$$

Computation results depend strongly on the available nuclear reaction cross section data [77]. The sets of nuclear interactions cross sections that we used are

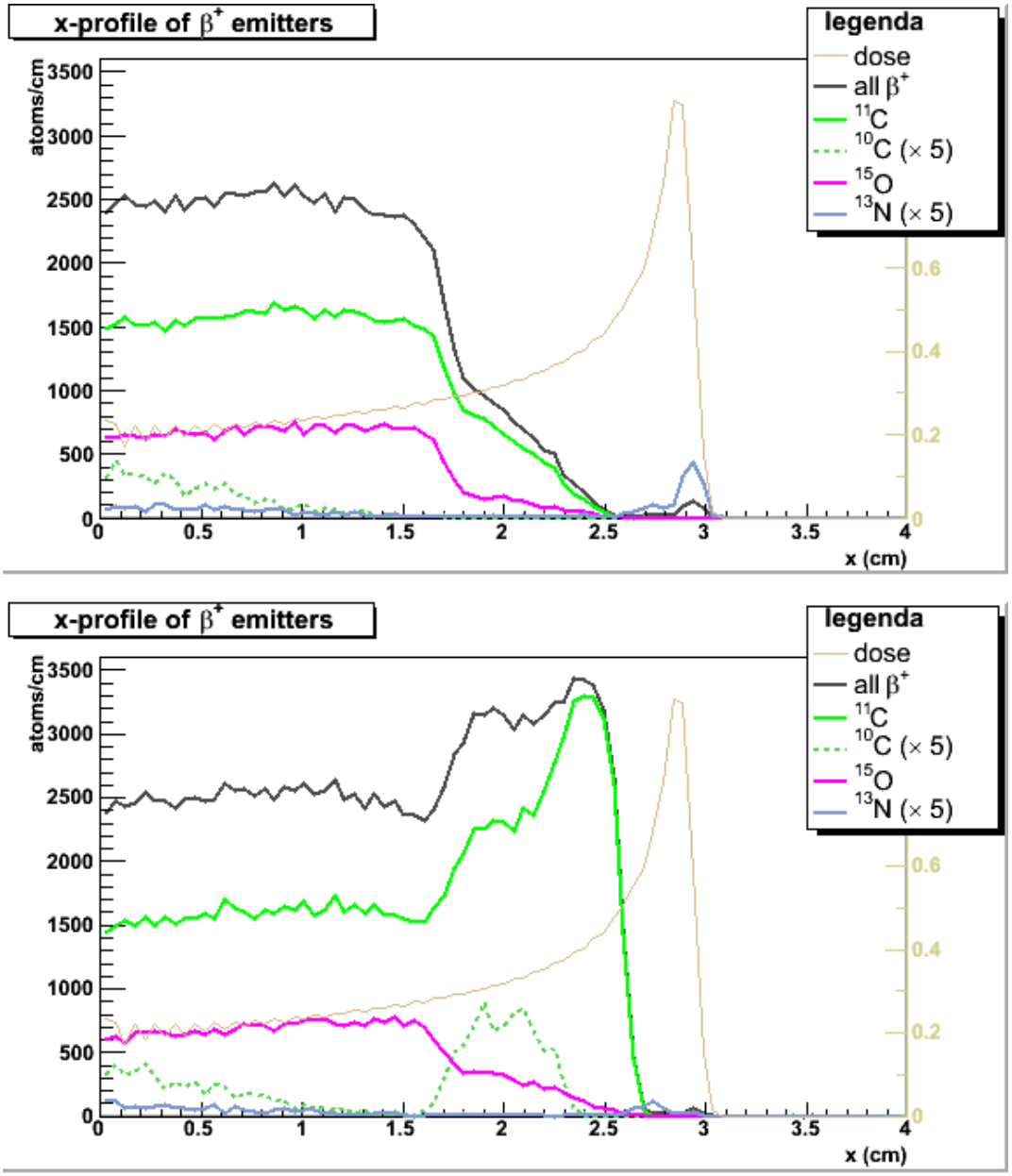

Figure 3.4: Comparison of the β^+ emitter density profiles in PMMA as generated by the simulation Z_{max}=7,A_{max}=13 (top) and Z_{max}=9,A_{max}=17 (bottom) for 62 MeV protons. Dose profile (arbitrary units) is also shown for comparison.

from "Experimental Nuclear Reaction Data File" (EXFOR) maintained by National Nuclear Data Center at BNL). So far we considered only the main (p,pn) reaction channels on carbon and oxygen, leading respectively to ^{11}C and ^{15}O production, which are the reactions determining the shape of the activity profile in our phantom experiments; in the future we can easily extend our results to more complex biological targets which may reasonably contain also nitrogen.

3.4 Conclusions

In table 3.3, the total amount of beta emitters produced by GEANT4 simulations are summarized and compared with results of the numerical approach presented in the previous section and those obtained by FLUKA based simulations presented in [79].

	62 MeV		70 MeV			
	GEANT4		GEANT4		FLUKA	ANALYTIC
	Z7-A13	Z9-A17	Z9-A13	Z9-A17	[79]	[66]
^{11}C / 10^6 p	6260	10182	7634	11052	7595	10716
^{15}O / 10^6 p	2569	2825	3103	3380	3919	2282
^{10}C / 10^6 p	108	271	193	361	70	-
^{13}N / 10^6 p	93	66	88	66	-	130

Table 3.3: Total amount of beta emitters produced by simulating proton irradiation with different codes. On the left: comparison between the two versions of GEANT4 simulation for 62 MeV protons impinging on PMMA. On the right: comparison between Monte Carlo and analytical codes, calculated for 70 MeV protons impinging on PMMA.

In figure 3.5 the β^+ emitters linear density for the "smoothed" version of the Z7-A13 and Z9-A17 Geant4 simulations is presented, and the FLUKA and numerical results are shown for comparison.

The worst simulation results are obtained with GEANT4 when using the more natural choice for Fermi break-up parameters (Z_{max}=9, A_{max}=17, labelled in figure 3.5 as "GEANT4 MC"). Simulation results using GEANT4 and Z_{max}=7, A_{max}=13 for the Fermi break-up (labelled as "GEANT4 MC (bis)" in figure 3.5) appear instead compatible to those obtained with FLUKA based simulation using only the internal models. Moreover, it is worth noticing that the application of such method is to predict experimental data corresponding to (total) activity profiles, not nuclides profiles. When the finite PET resolution and the different

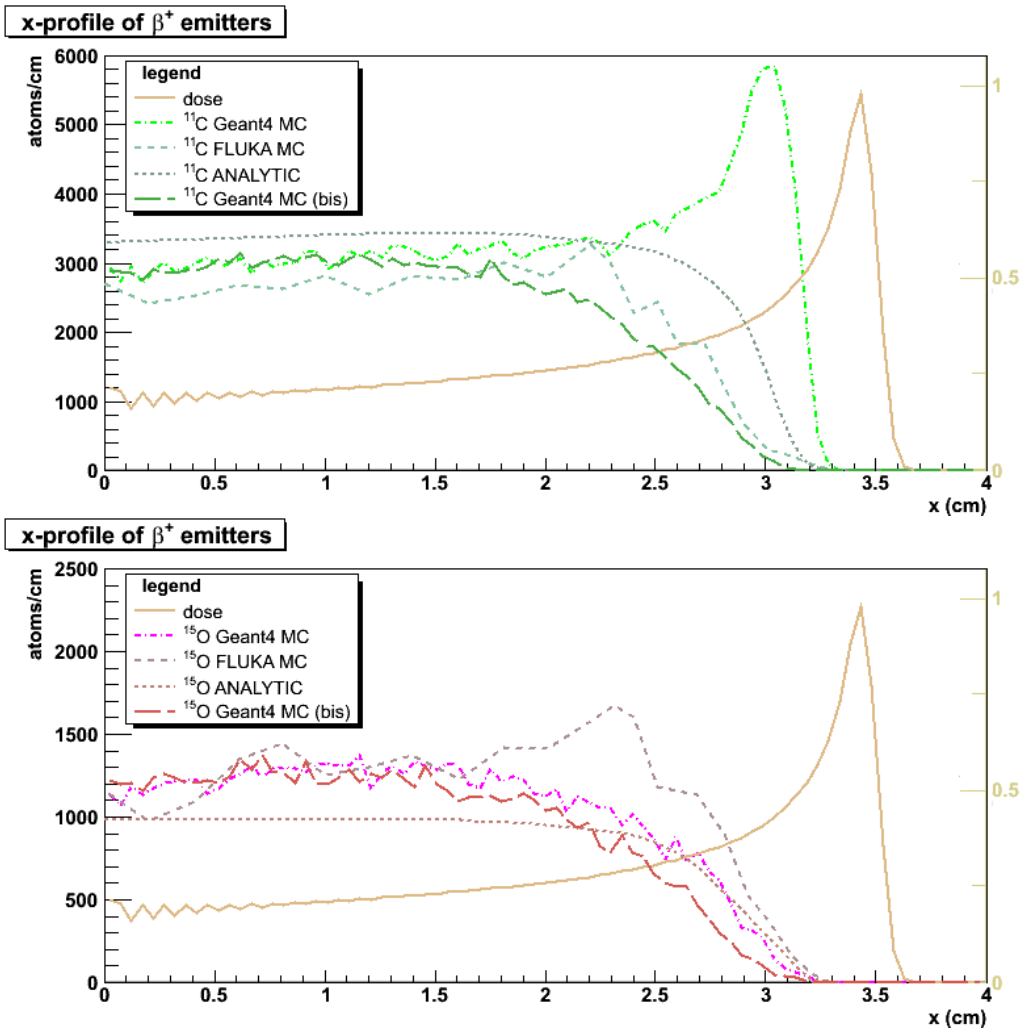

Figure 3.5: β^+ emitter density profiles of 70 MeV protons in PMMA: ^{11}C (top) and ^{15}O (bottom). Comparison of the results as generated by Geant4 MC (20-60 MeV overlap, Z_{max}=9, A_{max}=17 as limits for the Fermi break-up), a second version of Geant4 MC (labelled with *bis* in the legend, 20-60 MeV overlap, Z_{max}=7, A_{max}=13 as limits for the Fermi break-up), FLUKA MC [79] and the analytical approach [66]. The normalized dose profile is also shown.

half-time of each β^+-emitter are taken into account, the discrepancy between the activity profiles produced by any of the three prediction methods and the experimental data is almost negligible [80, 81].

The GEANT4 results, however, provides an inadequate agreement with the experimental data, concerning in particular the multiplicity of ^{11}C and ^{15}O fragments in the precompound model, and an unexpected behaviour of the Fermi break-up subroutine has been evidenced. The lack of a complete validation of implemented models and the difficulty to introduce data based corrections do not allow us to be confident in the GEANT4 application: some other deviations from experimental evidence could be present, which have not yet been identified. An additional reason to discard the Monte Carlo approach is the long time (more than one day) needed for simulation of a reasonable number of protons, with respect to the analytical computation, based on experimental cross section and lasting less than one hour.

In conclusion, we preferred to adopt the semi-analytical for the computation of activity (and dose) distributions. The application of the developed method will be presented in section 7.5.

However, the Monte Carlo approach has not been abandoned on a permanent basis. It will be further investigated for the future clinical application, and both the possibility of a FLUKA based simulation or a GEANT4 based simulation will be considered, depending on the future status of their reliability.

Chapter 4

The DoPET design

4.1 The front-end electronics

The H8500 "Flat Panel" PMT has an overall active area of 49×49 mm^2, and is characterized by a multi anode structure segmented into 8×8 independent pixels, each one of 6.08×6.08 mm.

Though the average anode sensitivity is rather high (55 A/lm), the metal channel dynode structure lead to a different gain for each anode pad. Such non-uniformity in the anodes response can reach relative ratios as high as $6 : 1$ in some devices, which might dramatically affects the PMT performances. In the so-called multi-anode readout the charge on each anode is individually read out and digitized. The subsequent event position calculation is performed via software. This kind of read out would allow an efficient compensation, since the Hamamatsu company provides a map of anodes gain with each tube. However, in the average cases of non-uniformities with a range of $3 : 1$, the distortion of the planar image does not impair pixel resolving, and then there is no strong need for the elaborate single-anode electronics.

[1] A preliminary note is required for results presented in this chapter. Measurements reported here have been performed before the mechanical support was available, and using the silicone optical grease from Bicron® for the optical coupling, instead than an optical-quality thermoplastic Cargille Meltmount™. Therefore neither reproducibility nor optimization can be assured. The refraction index of the silicon grease is 1.47, the one of the thermoplastic is 1.58. These must be compared with values for the photocatode glass window (about 1.5) and for the scintillator crystals (from 1.8 to 2.2).

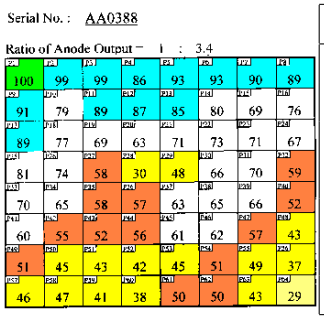

parameter	description	
Spectrad Response		300-650 nm
Peak Wavelength		420 nm
Window	1.5 mm	Borosilicate glass
Dynode	12 stage	Metal channel dyn.
Gain		10^6
Cathode Luminosity		55 μA/lm
Anode Luminosity		55 A/lm

Figure 4.1: On the left: a map of anodes gain, as provided by the PMT data sheet. Green: maximum gain=100; light blue: 99-85 relative gain; white: 84-61 relative gain; red: 60-50 relative gain; yellow: lower than 50 relative gain. On the right: detector parameters as provided by the generic PMT data sheet.

The charge multiplexed readout schemes electronically reduce the 64 anode outputs to four analogue signals. These signals are used to determine the deposited energy, and to calculate off-line the photon interaction point. Therefore, in contrast to a multi-anode readout, neither identification of multiple interactions nor software correction for anode non-uniformities are possible.

The individual anode readout is in principle more reliable than a multiplexed one, but it is electronically more cumbersome and expensive. In addition, a multiplexed solution enables us to use the multi-wire PMT readout previously developed for the Small Animal ScannerYAP-(S)PET [47], for the processing of the four positioning signals up to the image reconstruction.

Recent studies on planar images show that, through the selection of a suitable resistive network divider, spatial and energy resolution can be obtained that are comparable with multi-anode readout [82, 83, 84].

For sake of completeness, however, an absolute reference for the evaluation of the results has been derived by measurements with a multi-anode readout. For a detailed description of multi-anode readout setup used, see reference [85].

4.1.1 The choice of the multiplexed readout

We have initially evaluated the use of a discretized positioning circuit (DPC, [86]) 64-input/4-output multiplexed readout as described in the following. A great advantage of DPC is the low complexity of the resistive chain and its totally passive nature. Its major disadvantage is the asymmetry of the x/y charge division, that in particular could impair pixel identification along one direction. The drawbacks

of the DPC make it a non-optimal choice for the front-end read-out, and led us to explore new possibilities.

A recent multiplexed charge division scheme called symmetric charge division (SCD, [87]) overcomes the asymmetry of the DPC system in the image reconstruction. A 64-input/(8+8)-output circuit, followed by simple resistive chains to further reduce to four the number of signals, can be used in a setup similar to the one needed by the DPC chain.

The aim of the measurements presented here is the study of the intrinsic spatial resolution that can be obtained with the commercial version of Hamamatsu H8500 by using a SCD system readout as an alternative to the DPC one.

DPC Multiplexed Readout System

The discretized position-sensitive readout circuit (figure 4.2) is made of an array of resistors that divides the charge between 4 low-impedance op-amps. The last dynode output signal from the PSPMT is sent to a Constant Fraction Discriminator ORTEC model 534 for amplitude independent tresholding, followed by a gate signal generator for a 32-channel peak-sensing VME-based ADC. The four preamplified signals are sent to the input channels of the peak ADC. Digitized signals are then acquired through a local host computer and the event position is reconstructed by software.

$$\begin{aligned} X &= \frac{(V_A+V_B)-(V_C+V_D)}{V_A+V_B+V_C+V_D} \\ Y &= \frac{(V_A+V_D)-(V_B+V_C)}{V_A+V_B+V_C+V_D} \end{aligned} \tag{4.1}$$

See figure 4.2 for the legend of the signals.

SCD Multiplexed Readout System

The SCD circuit, for $N \times M$ input channels, requires $N + M$ op-amps to collect the charge, i.e., one for each one of the N rows and of the M columns. For the measurements presented, using one 64-anode PMT H8500, $N = M = 8$. After a charge-to-voltage conversion stage, a simple resistive chain is used to further reduce to 4 the output channels. Part of the readout system of the YAP-(S)PET Small Animal Scanner [47], i.e., the preamplification, the acquisition board and the image reconstruction software, has been used for the further processing of the

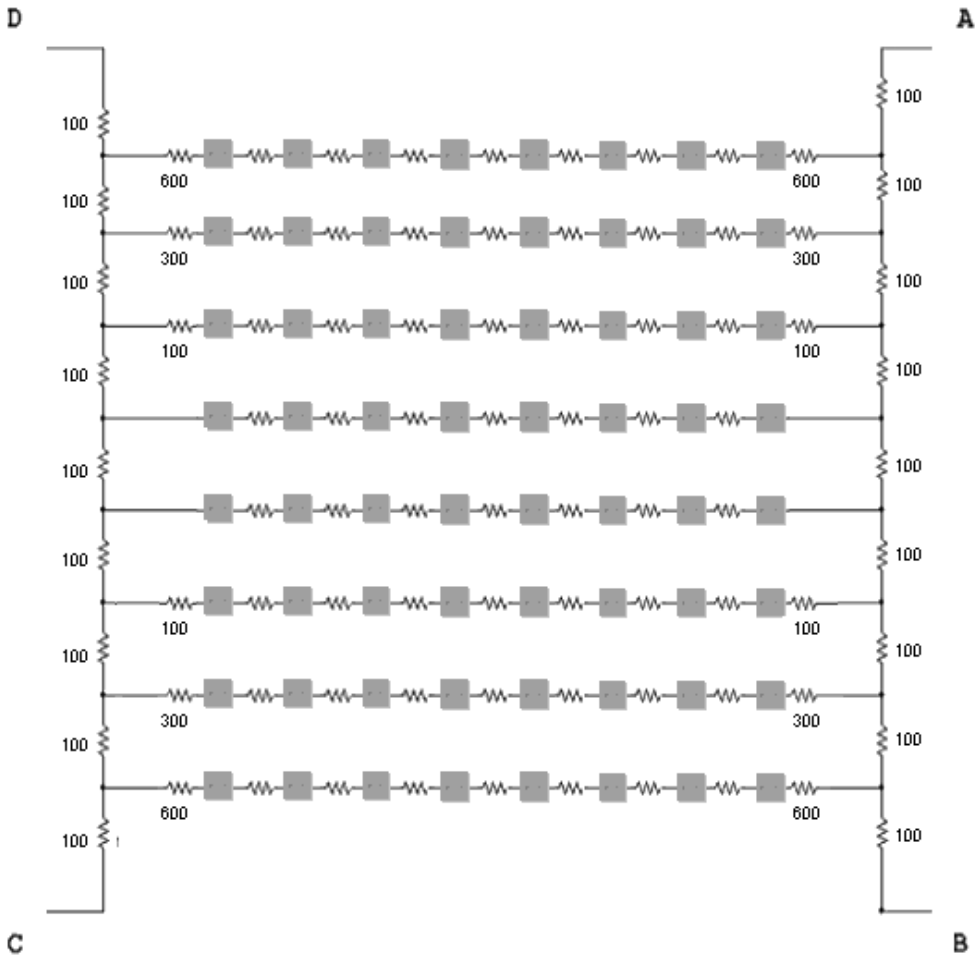

Figure 4.2: Schematic diagram of the Discretized Positioning Circuit. Resistor values not indicated correspond to 1 kΩ. Inputs (PMT anodes) are represented as grey squared pads), outputs are sent to the pre-amplification stage.

four position signals.

$$\begin{aligned} X &= \frac{V_{x+}-V_{x-}}{V_{x+}+V_{x-}} \\ Y &= \frac{V_{y+}-V_{y-}}{V_{y+}+V_{y-}} \end{aligned} \tag{4.2}$$

See figure 4.3 and its caption for the comprehension of the signals.

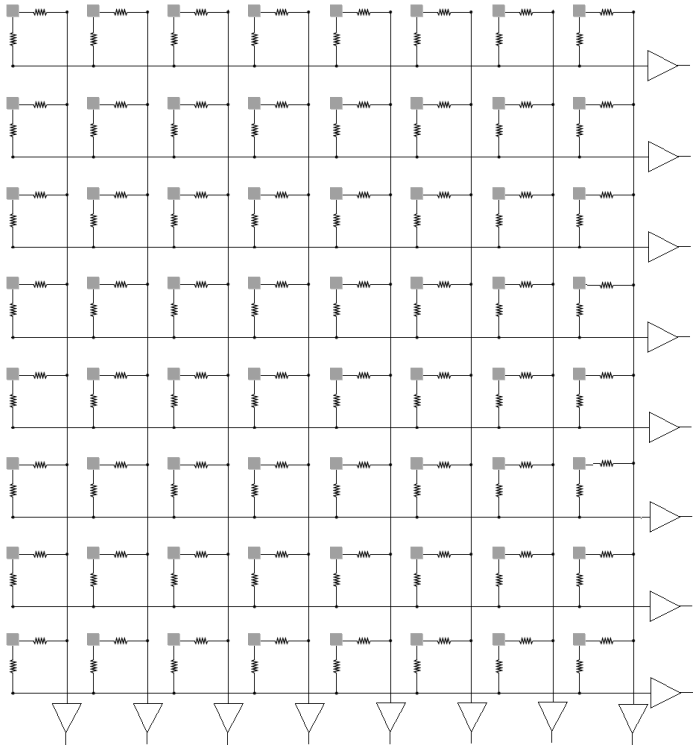

Figure 4.3: Schematic diagram of the Symmetric Charge Division Circuit. All the resistors have the same value, i.e., 1 kΩ. Inputs (PMT anodes) are represented as squared grey pads, outputs corresponds to the 8+8 op-amps. Row outputs are used to produce the V_{x^+} and V_{x^-} signals, column outputs are used for V_{y^+} and V_{y^-}. For the complete circuit, together with the final resistive chains, see figure 4.5.

It is worth noticing that in principle the same optimized acquisition board might have been used for the DPC chain, for a more rigorous comparison. However, the changes required to adapt the system would have required additional efforts for the new preamplification board design and the new version of the software (for implementing formula 4.1 in planar images).

Conclusion

The comparison presented here is based on the read-out of the H8500 PMT tube coupled with YAP:Ce scintillator matrices of different pixel sizes (2 mm and 1.5 mm). The analysis is done for flood field irradiation at the energy of 511 keV.

Table 4.1 summarize the results of comparison of the readouts using 2 mm pixels, in terms of the main parameters characterizing a flood field image of a pixilated crystal: peak-to-valley ratio (P/V) and spatial resolution. The first is

	Peak to Valley ratio	Peak FWHM	Crystal $\sigma_{res} = \sqrt{\sigma_p^2 + \frac{d^2}{12}}$
DPC	6.0	0.62 mm	0.64 mm
SCD	6.7	0.82 mm	0.68 mm

Table 4.1: Comparison of DPC and SCD multiplexed readout for ^{22}Na flood field irradiation of YAP:Ce crystal, 2.0 mm pixel, 2.01 mm pitch, 25 mm thickness. Comparison performed on image profiles along the horizontal axis.

measured as the average counts at peaks divided to the average counts at valley for a typical row (column). The second parameter is obtained as the average FHWM of the gaussian fits of each pixel distribution in a typical row (column). The third column presents the intrinsic spatial resolution σ_{res} computed from the measured peak width σ_p and the intrinsic crystal variance $\frac{d^2_{pitch}}{12}$.

Using a 2 mm pixel, results of the two readout are comparable. The horizontal direction, analyzed in the table, is the one with the worst performance for DPC readout. SCD has instead a symmetric behaviour in both directions. Therefore, considering the vertical direction (see figure 4.4, left), performances may be even better for DPC read-out.

However, using a 1.5 mm pixel (see figure 4.4, right) the DPC chain readout appears totally inadequate for imaging. The blurring in horizontal profile from an image using the DPC chain totally prevents from pixel resolving. The DPC preamplification stage could be further optimized to reduce the asymmetric behavior of the four signals. However, this asymmetry is an intrinsic characteristic of that chain and the advantage of an alternative symmetric setup is undoubtful. In fact, a detailed comparison of the results with multi-anode and DPC multiplexed readout was already performed [88], and the limits of the DPC readout were demonstrated.

Moreover, the optimization of the SCD board, after the final readout choice, led to even better performances.

The YAP-1.5 mm result with the SCD is without any doubts promising, especially for those PET applications where smaller pixels are not needed. As it will be seen in the following section, further improvements can be achieved with a crystal having a higher light yield.

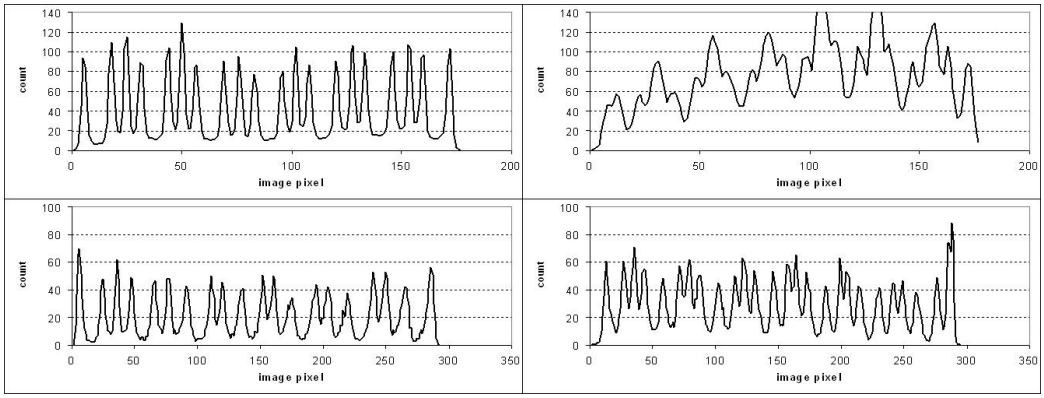

Figure 4.4: Comparison of image profiles for ^{22}Na flood field irradiation of YAP crystals (see table 4.3). On the left: vertical profile for finger crystals of 2 mm pitch. On the right: horizontal profile for finger crystals of 1.5 mm pitch. DPC results are presented in the first row. SCD are shown below.

4.1.2 Performance with the SCD multiplexed readout

Once the front-end read-out has been chosen, the design of final layout has been committed to an external industry, which designed and printed the circuits. At this stage, a significant change has been introduced in the multiplexing configuration. An alternative solution for the second multiplexing step has been introduced, in order to avoid the charge-to-voltage conversion of the 16 + 16 outputs of the SCD network, that would be required by the following linear resisting chains. We then followed the approach described in [89], since the proposers claim a better charge collection without inclusion of the noise contribution of the resistive readout chain.

Following that scheme, all of the individual amplified horizontal (vertical) SCD-network outputs are interconnected via coupling resistors. Resistors provide the signal distribution to the A and B summing amplifiers, and their values are determined based on equations 4.3:

$$R_n^A = \frac{R}{n} \tag{4.3}$$

$$R_n^B = \frac{R}{N - n + 1} \tag{4.4}$$

where R is the maximum resistor value in the resistive network, N is the number of readout channels ($N = 8$ in our read-out) and n is the channel index. The

conversion gain obtained with this setup changes linearly as a function of the input index. The average differential non-linearity measured by [89] is 10%. Figure

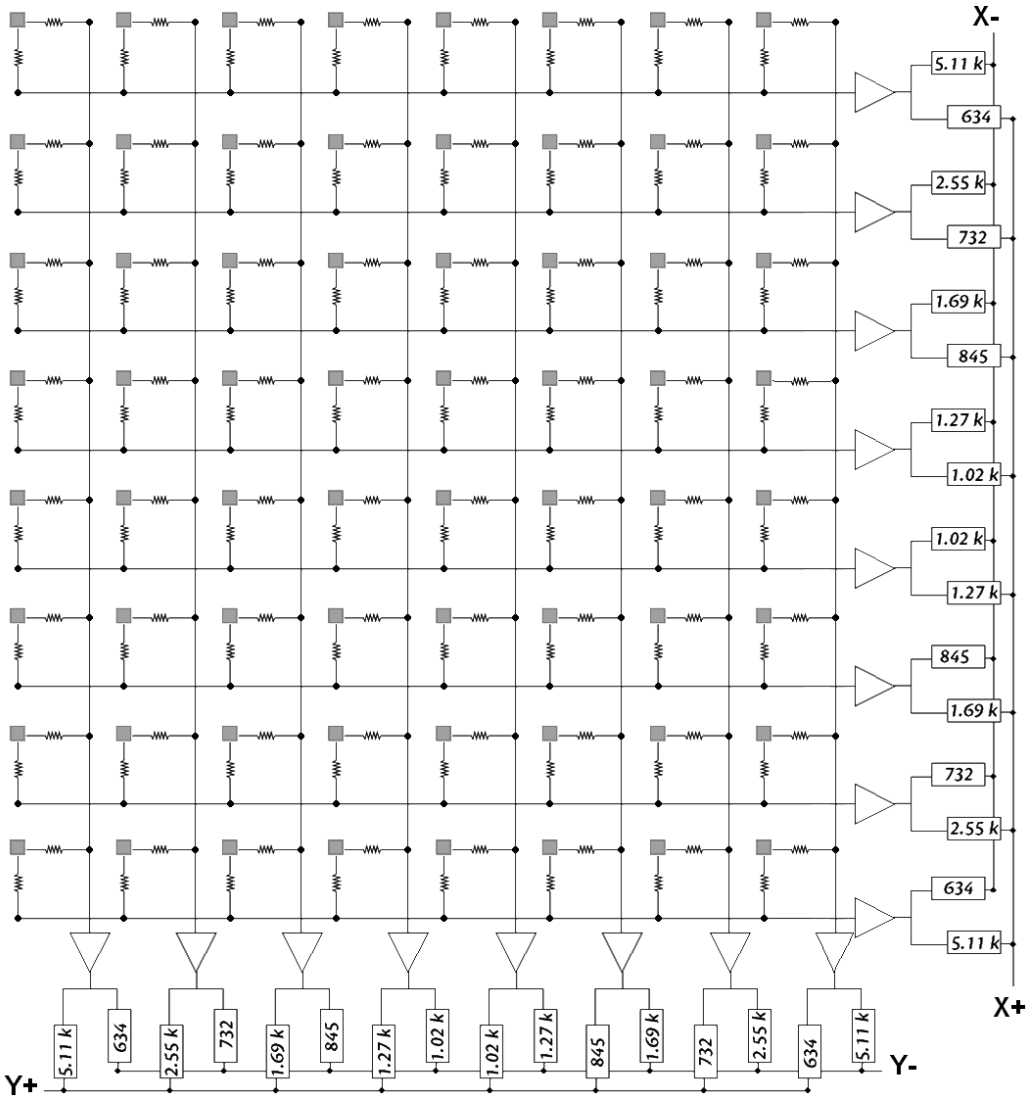

Figure 4.5: Schematic diagram of the final layout of the multiplexed read-out 64-input/(2+2)-output. Value of all the resistors is 1 kΩ. Input (PMT anodes) are represented as squared grey pads, outputs are labelled as x_A, x_B, y_A and y_B.

4.5 shows our implementation of the analog signal converter as final stage of the multiplexed read-out.

With the new electronics board, we have performed a more detailed evaluation of performances of the H8500 PMT coupled to different scintillator crystals and read-out through SCD multiplexed scheme. No comparison with the previous layout of SCD read-out was possible, due to the failure of the older electronics board.

First, a comparison has been performed on ^{57}Co flood field images obtained by multi-anode and multiplexed SCD. In table 4.2, the results of the measurements with NaI crystal (1.8 mm pixel, 2.0 mm pitch) are summarized.

	Energy res.	Peak to Valley ratio	Peak FWHM	Crystal σ_{res}
MA	11.4 %	7.4	0.93 mm	0.70 mm
SCD	16.2 %	6.8	0.83 mm	0.68 mm

Table 4.2: Comparison of multi-anode and SCD multiplexed readout for ^{57}Co flood field irradiation of NaI(Tl) crystal, 1.8 mm pixel, 2.0 mm pitch, 10 mm thickness.

The multiplexed SCD system has then been used for measurements with matrices of different crystals (BGO, YAP and LYSO) irradiated with 511 keV radioactive sources. The characteristics of the matrices are summarized in table 4.3.

Crystal	pixel (mm)	pitch (mm)	thickness (mm)	reflective layer (μm)	reflective layer type
BGO	1.5	1.7	11	200	epoxy
YAP:Ce	1.5	1.5	12	10	aluminum
LYSO:Ce	1.5	1.7	20	200	epoxy

Table 4.3: Summary of characteristics for crystals used in the measurements.

Measurement results are summarized by figure 4.6 and table 4.4. YAP and LYSO matrices can be easily identified with pixel pitches down to 1.5 mm.

Crystal	Energy resolution	Peak to Valley ratio	Peak FWHM	Crystal σ_{res}
BGO	n.a.	1.37	1.66 mm	0.83 mm
YAP	21.0 %	3.55	0.70 mm	0.53 mm
LYSO	16.8 %	6.35	0.57 mm	0.50 mm

Table 4.4: Summary of results obtained with the SCD multiplexed readout.

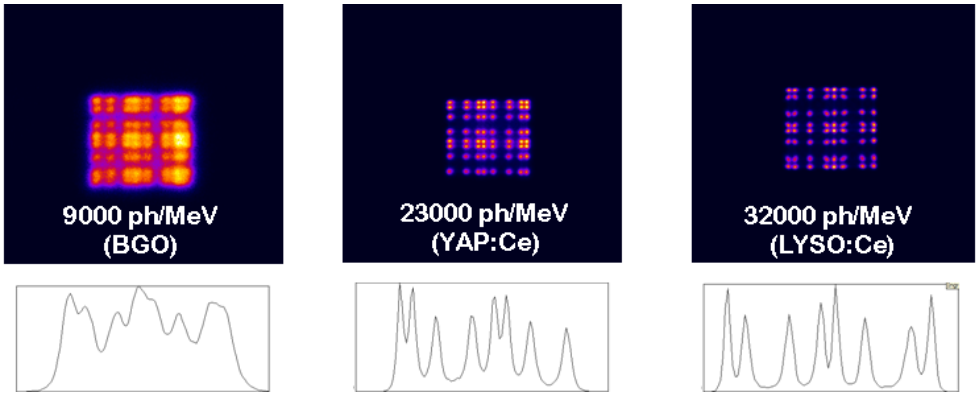

Figure 4.6: Imaging performance with crystals of different light yield.

As a final remark, in figure 4.7 there is shown the effect produced at the image edges by crystal matrices as large as the H8500 effective area. This effect is almost independent from the choice of the read-out electronics. The interaction position is well determined when the light is divided between few anodes and the subsampling can be used. For events at the edge this does not happen even for the crystals with a large light distribution, like NaI. The light of the last two or three pixels is partially lost, since no further anode is present beyond the end of the matrix. The center of gravity algorithm calculates, in these cases, a position ”shifted” towards a direction opposed to the light loss. The effect is a worsening of pixel resolution at the border of the photocathode, and therefore a worsening of the spatial and energy resolution in the last few millimiters of the detector area.

4.2 The scintillator crystals array

Scintillators utilize the energy of detected particle to generate optical photons. Energy is generally deposited in the crystal by ionization, either directly by charged particles, or by the conversion of photons into electrons or positrons which subsequently produce ionization. This energy is transferred to the luminescent centers which then radiate a fraction of it as scintillation photons. Beside scintillation also fluorescence can happen: the initial atom excitation takes place via the absorption of a photon, and de-excitation by emission of a longer wavelength photon.

Absorption of X- or γ- radiation energy by materials occurs through three processes: Compton scattering, photoelectric effect and electron-positron pair pro-

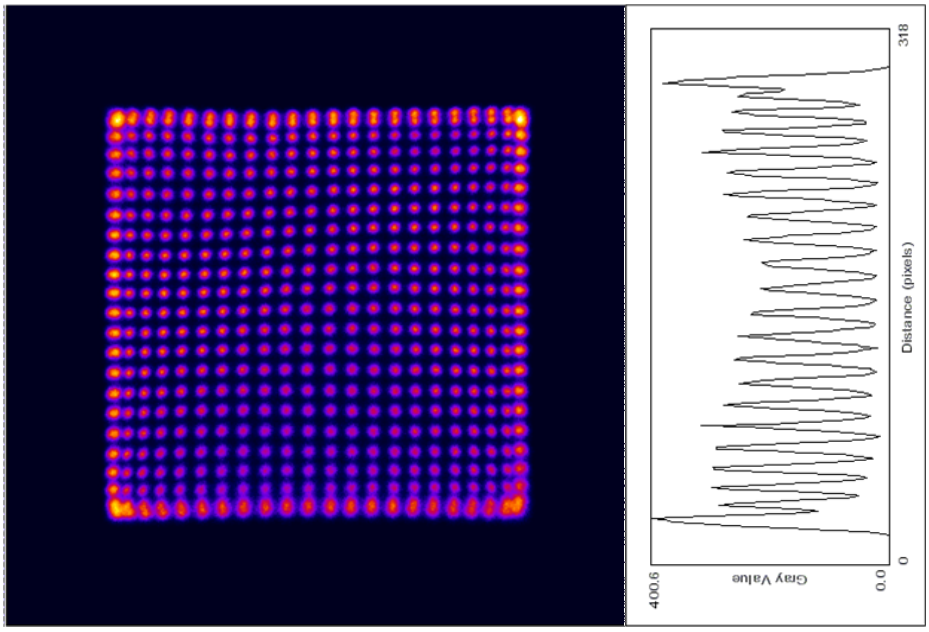

Figure 4.7: Effect produced at the edge of crystal matrices as large as the H8500 effective area. ^{57}Co flood field irradiation of NaI(Tl) crystal, 1.8 mm pixel, 2.0 mm pitch, 10 mm thickness. The first and the last peaks in the image profile are both the sum of two pixels.

duction (for energies above the 1.022 MeV energy threshold, i.e., not in the case of 511 keV photons). The Compton scattering process, at sufficiently high photon energy, depends only on the number of electrons in the scintillator and not upon the nature of the nuclei. This process deposits only a fraction of the ionizing photon's energy in the absorbing medium and thus the resulting scintillations are not a simple function of the initial energy. The photoelectric effect results in the conversion of the photon's energy into kinetic and potential energy of electrons in the target material. The stopping power of common materials for such electrons is great enough so that, for practical size bulk scintillators, all of the initial photoelectron energy is absorbed. However, as a consequence of the hole left in the atom shell that originated the photoelectron, part of the photon energy is not transferred to the electron and is emitted as fluorescence characteristic radiation, thus becoming useless for the scintillation conversion. The energy of fluorescence radiation depends on the atom species and is of the order few keV.

4.2.1 Comparison among most common PET scintillator materials

The optimal scintillator material must satisfy several requirements, which are determined by the specific application of the light detector.

The requirements for the ideal PET scintillator crystal are optimal energy resolution, high detector efficiency for 511 keV photons, high light yield, short decay time, perfect matching of the scintillation spectrum and the maximum photodetector quantum efficiency. Such requirements, for PET applications, find the best answer in inorganic scintillation materials.

The cross section of both Compton scattering and photoelectric effect depends on the effective atomic number (Z_{eff}) of the scintillator crystal. In particular, a higher Z_{eff} value increases the number of photoelectric occurrences with respect to Compton scattering in the crystal, since the cross section for photoelectric effect increase at least[1] as Z_{eff}^3 and the Compton scattering increase only linearly with Z_{eff}. Events with an energy release lower than 511 keV may also be due to photons that have undergone a scattering in the patient and then might be a source of false lines of flight. Since the photon scattering in the patient is one of the main source of error in reconstruction, events which are not within a certain energy interval around the photopeak are usually rejected. Therefore, the optimal peak-to-Compton edge ratio provided by a a high Z_{eff} crystal allows to reject the scattered events with minimal loss of real lines of flight for the image reconstruction.

Thick crystal are more efficient, but excessively long ones degrade the spatial and energy resolution. In fact, a large thickness introduces parallax errors, reduces the collection of light through self-attenuation and enhances the probability of multiple Compton interactions. When a high detection efficiency is necessary, the best crystal to be used are those with a very high absorption coefficient, i.e., with high Z_{eff} and density. The crystal can be then few radiation lengths thick, without impairing the detector resolutions.

The scintillator should also provide a fast response, so that the coincidence between the two photons is efficiently detected in a short time window, reducing the possibility of random coincidences, pile up and dead time.

In table 4.5 there are listed the characteristics of the most common inorganic scintillator used in PET.

[1] The cross section increase as Z_{eff}^5 when the energy of the incident photon is much higher of the bound energy of electrons for the specific material.

material	density ρ $[g/cm^3]$	effective atom. num. Z	light yield [%NaI]	decay time [ns]	peak wavelength [nm]	refraction index n
NaI(Tl)	3.76	51	100	230	410	1.85
CsI(Tl)	4.51	54	45	1000	565	1.80
BGO	7.13	75	15	300	480	2.15
GSO:Ce	6.71	56	26	600	430	1.85
LSO:Ce	7.40	66	75	40	420	1.82
LYSO:Ce	7.10	63	90	40	420	1.81
YAP:Ce	5.37	34	55	27	370	1.95

Table 4.5: Basic characteristics of scintillator crystals commonly used in PET scanners. A change in doping material and concentration can produce some variation in the listed values.

For our specific application, due to the low rates available and the large noise produced by target activation, fast and efficient detection of each event is even more important. GSO and CsI are then not appropriate because of the long decay constants.

As already seen in the previous section, BGO has too poor a light yield for the performances of our multiplexed PMT readout. In fact, when using a PSPMT with such a large anode size as H8500, a very narrow light distribution of crystal causes a subsampling for crystal pixels that are coupled close to the centre of an anode. This has been found [90] to be the reason of the small, regular non-linearities in the image which makes it visible the anode structure of the H8500 tube: events are ”pulled” towards the centre of the anode and pixels are shown with a periodicity equal to the ratio of anode and pixel pitches. The effect is visible also with YAP scintillator, although in that case it is less pronounced.

The better look-up-table of NaI, as it has been observed in figure 4.7, is due to a wider intrinsic light profile, but also to the glass window, that protect the hygroscopic crystal and increases the spread of the light distribution. NaI has one of the highest light yield, and even the deterioration introduced by a glass window does not affect too much its performances. However it must be excluded for our application because of its low density and Z_{eff}.

Among those crystals listed in table 4.5, LSO e LYSO appear as the best compromise for a fast scintillator, with high light yield and good detection efficiency. Such scintillators suffered at the beginning from high cost and low availability,

but their application is now rapidly expanding.

The choice of scintillator material has then fallen on LYSO ($Lu_{1.8}Y_{0.2}SiO_5$) matrices of 18 mm thickness (equal to 1.5 attenuation lengths) for high photon absorption. Hilger Crystal company is the one which provided us the offer with the best compromize between crystal quality and price. The pixel size, 2 mm$\times$2 mm, has been chosen on the basis of the spatial resolution limits given by the PMT and the PET reconstruction algorithms.

By preliminary theoretical consideration we concluded that we preferred aluminization as method for the optical isolation of pixels, since it reduced to minimum the dead spaces in the array. Matrices were then ordered and delivered, but the samples that we initially received resulted totally unsatisfactory. Crystal light yield was totally incompatible with what was expected for LYSO. We believed that the low performance of such crystals arrays were due to an inefficient light reflection within the crystal and then we decided to make some experimental evaluation in collaboration with the Hilger Company to confirm our assumption and find an alternative solution. The measurements performed and the final conclusions are reported in the following section.

4.2.2 Choice of the reflective material

In order to evaluate the best compromise between dead space and light yield, we received by the Hilger Company three sets of LYSO pixels. They have the same size of those used for the arrays, i.e., $2 \times 2 \times 18$ mm^3, but each set was wrapped in a different reflecting material: aluminum, white epoxy resin, and teflon.

We measured the light output of the pixels by coupling them to the Photonis XP2020 PMT [91], a reference tube for γ-spectroscopy. Bicron BC630 Silicon optical grease was used for the coupling. The signal gate for the acquisition was generated with NIM modules by every last dynode signal higher than 70 mV, the digitalization of the PTM signal was performed with a VME module 32-bit QDC CAEN V792. The acquisition itself was performed by a home-made LabView routine. ^{22}Na and ^{57}Co point sources were used. Since the 511 keV photons produce much light in LYSO crystal, we attenuated the PMT signal with a resistive attenuator module.

Data were taken in single mode, and the results are presented in figures 4.8 and 4.10 and summarized in table 4.6. Within each set, results are rather homogeneous. For a better evaluation of data spread, as an example the data from the white epoxy set is shown again in figure 4.9 and the error band [mean-σ,mean+σ] is superimposed. The reflective material induces large differences between the

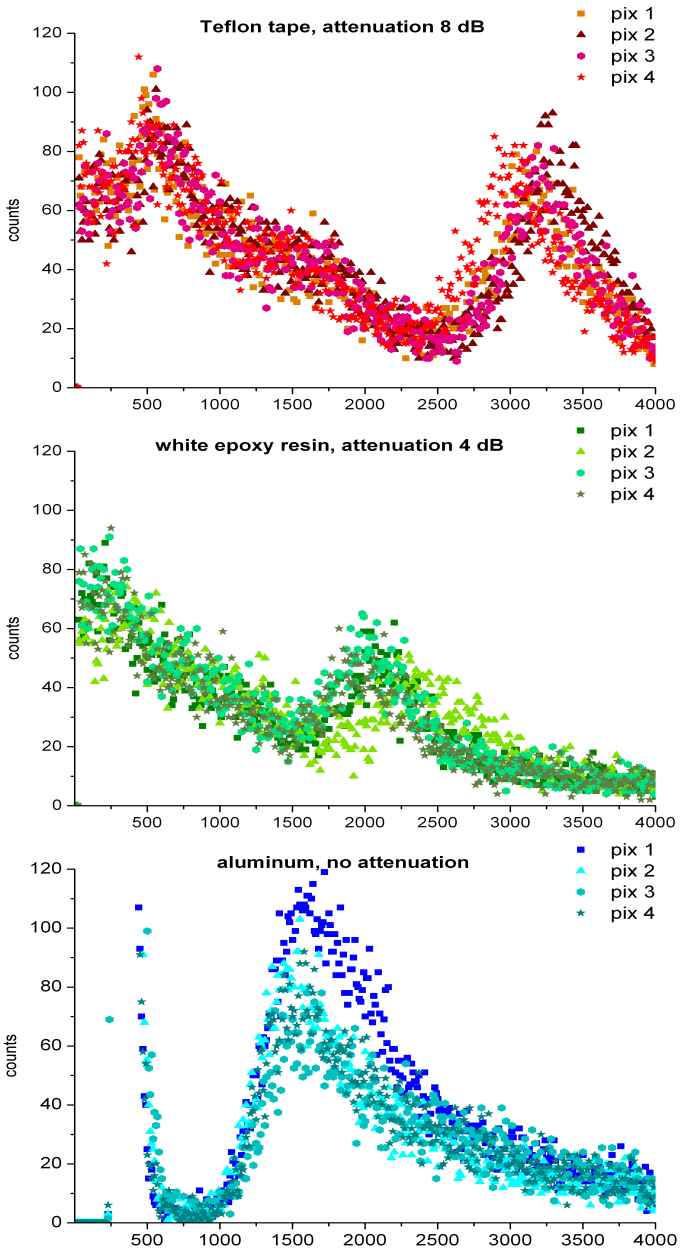

Figure 4.8: Spectra obtained by ^{22}Na irradiation from pixel wrapped in teflon (top), white epoxy resin (center), and aluminum (bottom). Pay attention to the different attenuation used for each measurement set. QDC channels on the horizontal axis.

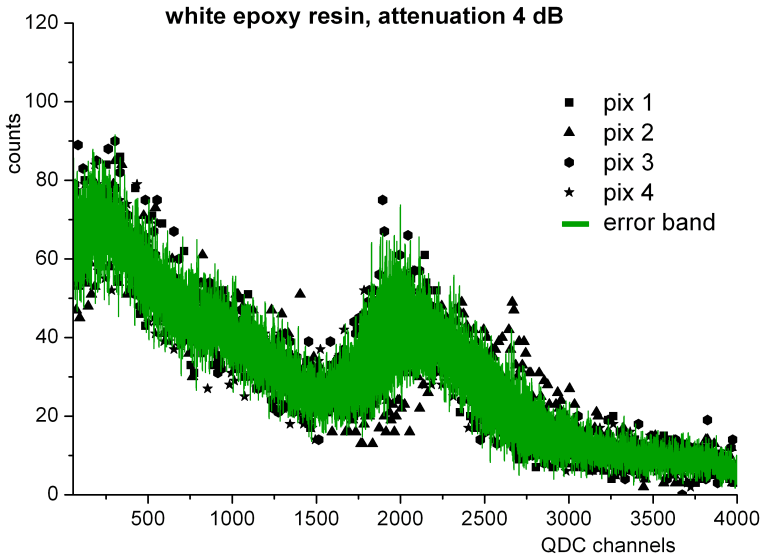

Figure 4.9: Spectra obtained by ^{22}Na irradiation from pixel wrapped in white epoxy resin. QDC channels on the horizontal axis. Data are the same already presented in the previous figure. An error band is here superimposed, computed as the average of the four spectra $\pm$ the standard deviation.

spectra of different set. First of all, one notices the different attenuation factors required in the measurement: 8 dB for the pixels wrapped with teflon, 4 dB for those wrapped with white epoxy, no attenuation for the aluminized pixels.

The spectra obtained from the aluminized pixel showed the anomalies which were already evidenced in the initially delivered aluminized matrices. Neither Compton edge nor photopeak are observable. Furthermore spectra obtained from ^{22}Na and ^{57}Co sources appear totally similar.

Wrapping material	Teflon	white epoxy resin	aluminum
Relative light yield	1	0.4	$<$0.2

Table 4.6: Average light yield obtained from the three sample of pixels, normalized to the value obtained from the Teflon-wrapped pixels.

We confirmed that the lack of reflection is due to the absorption of light, rather than its transmission, because wrapping the aluminized pixel with teflon did not lead to any improvement in light amount.

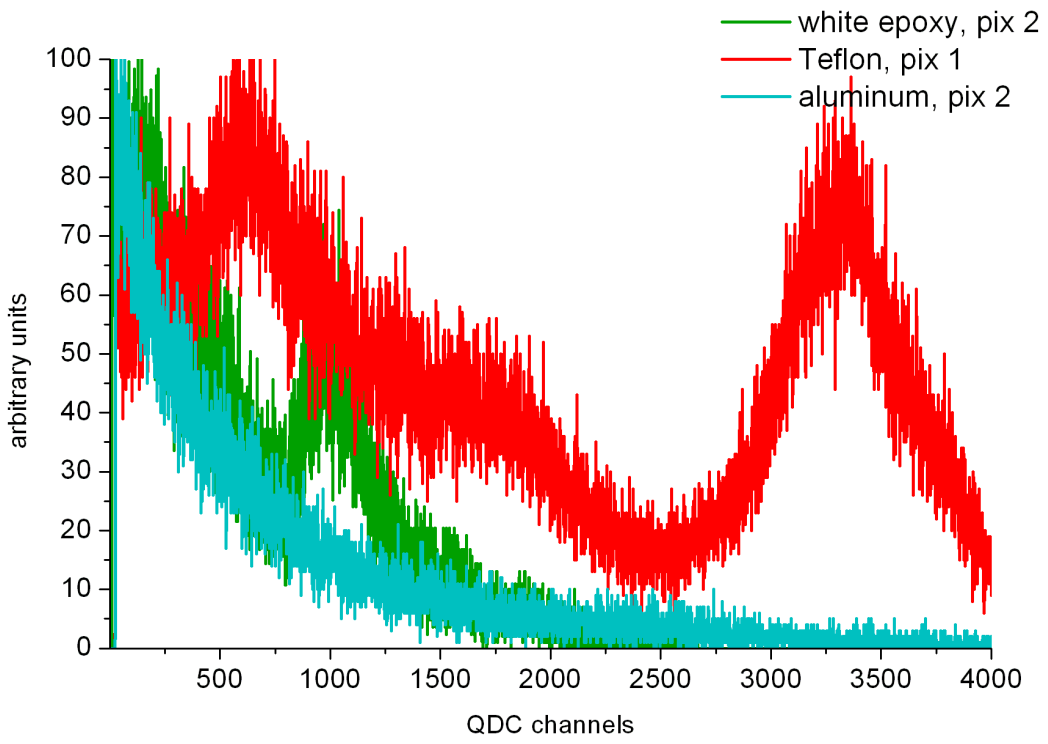

Figure 4.10: Comparison of the spectra obtained by ^{22}Na irradiation from pixel wrapped in different reflected material, after rescaling for the attenuator factor applied in the measurement. Aluminized pixel spectra shown is obtained from a measurement with 8 dB attenuation. Spectra are rescaled in the x axis, but no rebinning has been done, so the histogram counts are not normalized.

As a final test, we polished one of the aluminized pixel ($\#3$) up to the complete removal of the reflective material. As is shown in figure 4.11, the results of the measurements performed with such pixel wrapped in teflon are coherent with the original teflon-wrapped pixels.

After this final check, we asked the company to reprocess the aluminized matrices. The separation of crystal pixels from the original plastic frame required a heating of the crystals up to about 400 °C. After pixel aluminization has been removed with mechanical polishing, and pixel have been inserted in a new matrix frame. Since they do not provide teflon as reflective material for arrays, we were forced to choose white epoxy resin and to accept an increase of the dead space up to about 10% of the active area.

The refurbish of the two matrices has been completed in November 2006,

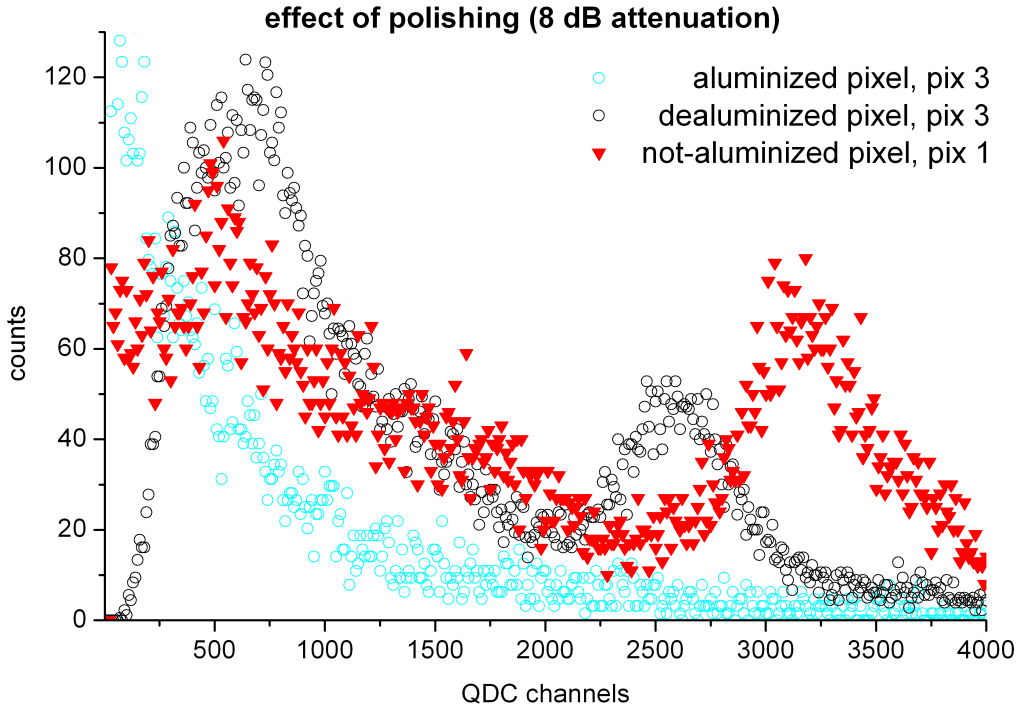

Figure 4.11: Spectra of pixel #3 before and after de-aluminization. Comparison with a not-aluminized pixel is shown. Both the de-aluminized and the not-aluminized pixel were wrapped with Teflon tape during the measurements.

just in time to perform the first measurements in Catania, which were planned on December 2006. However, time was not enough to perform characterization of the new arrays and calibration of the entire system before the run of December. Therefore the first set of measurements is less reliable than the following ones in terms of acquisition optimization and background rejection.

4.2.3 Characterization of the final scintillating arrays

After the refurbishing, the overall dimensions of the crystal array became larger than the PMT active area. Moreover, as already shown in section 4.1.2, the effective active area that can be used for a single PMT is less than 49 mm $\times$ 49 mm. In the first measurement run, the number of pixel used was 23$\times$23, corresponding to a detector area of about 49.3 mm $\times$ 49.3 mm. However pixel identification and energy calibration was almost impossible for the external rows, so

that the noise made totally useless the additional information. After several tests of alignment and optimization, it was concluded that no more than 21×21 pixel per matrix could be correctly identified. The exceeding pixel have been blinded by painting with black varnish the surface coupled to the PMT photocathode and the crystal arrays have then been glued to the PMTS with thermoplastic Cargille Meltmount^{TM}. The final detection area of each head is then 45 mm × 45 mm. The gluing process and the pixel blinding are reversible, therefore further optimization are still possible in the case of electronics improvements or if the PMTs should be recovered for the clinical version of the device.

The final version of the crystal arrays was of LYSO pixel (2 mm × 2 mm × 18 mm in size), polished on all sides and inserted in a white epoxy resin frame. The front and the back side of the matrix were polished and free of any cover. Since Teflon resulted a better reflecting material than white epoxy resin, we preferred to use three layers of white PTFE reflector tape from Saint Gobain Crystal to cover the back of the matrix. Alternative solutions, as white paint, paper, or Tyvek® have been also tested, but the Teflon has been confirmed as the best solution. In order to protect the detector head from the environmental light, once the detector elements are installed in the head and the Teflon layers are placed on the back of the matrix, a black sheet and two layers of black tape are used to close all the parts of the detector which could be hit by the light.

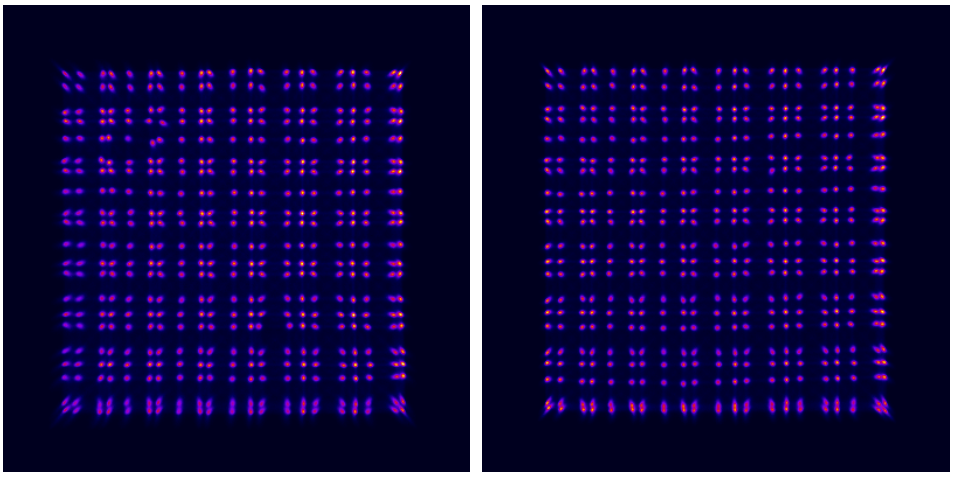

Figure 4.12: 511 keV flood field images of head #1 (left) and head #2 (right), acquired in coincidence in the final detector configuration: 21×21 LYSO scintillating crystals, 2 mm pixel, 150 μm white epoxy resin as reflective material.

An example of the flood field images obtained after such processing is shown in figure 4.12. The measured average peak-to-valley ratio is 7.2 and the average intrinsic spatial resolution is 0.7 mm.

After the completion of the assembly, pixel gain and sensitivity calibrations have been performed, following the procedure described in sections 1 and 3 of chapter 6. We give here only few numbers more related to detector hardware than to tomograph performances. The spread in calibration coefficient, measured as normalized standard deviation, is 2.1 for head $\#1$ and 1.2 for head $\#2$. The map of calibration coefficient for head two is represented in figure 4.13, and compared with the map of anode gains for the related fotomultiplier tube.

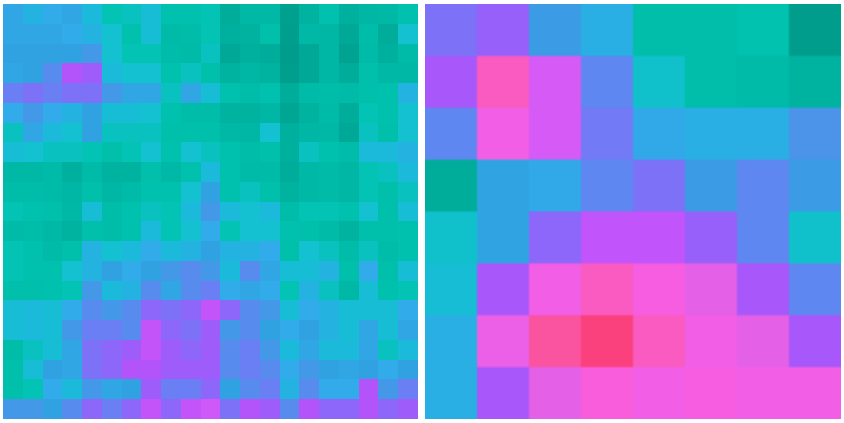

Figure 4.13: Map of energy calibration coefficients of crystals for head $\#2$ (left), compared with the map of anodes gain spread of the PMT used in head $\#2$ (right). Pink is the maximum for calibration coefficient and the minimum for anode gain, green is the minimum for calibration coefficients and the anode with the best gain.

Such comparison, for both detector heads, demonstrate how the leading effect in pixel gain spread is derived from the anode gain spread.

Despite its many advantages as a scintillator for PET, the lutetium in LYSO contains approximately 2.59% ^{176}Lu, a naturally occurring radioisotope with a half-life in the order of 3.8×10^{10} years.

Since the LYSO density is 7.1 g/cm^3, the LYSO molar mass is about $M_{LYSO} = 440.8$ g, and the Lu moles per LYSO mole are 1.8, the ^{176}Lu content in our crystal is about

$$N_{^{176}Lu} = f_{^{176}Lu}\nu_{Lu}\frac{\rho_{LYSO}}{M_{LYSO}}N_A = 4.5\cdot10^{20}\ \text{atoms/cm}^3,$$

and then the ^{176}Lu activity density is $A = \lambda N_{^{176}Lu} = 262$ Bq/cm^3. Our measurements, with an hardware threshold of about 70 keV, leads to a measured background rate density of approximately 270 cps/cm^3.

The experimental measurement is consistent with the theoretical estimation. The measured excess is due to the presence in the matrices of $25 \cdot 2 + 21 \cdot 2$ border crystals which have been blinded, but whose ^{176}Lu activity cannot be eliminated.

The ^{176}Lu decay scheme is shown in figure 4.14, together with the calibrated energy spectra of natural radioactivity measured in our LYSO matrices.

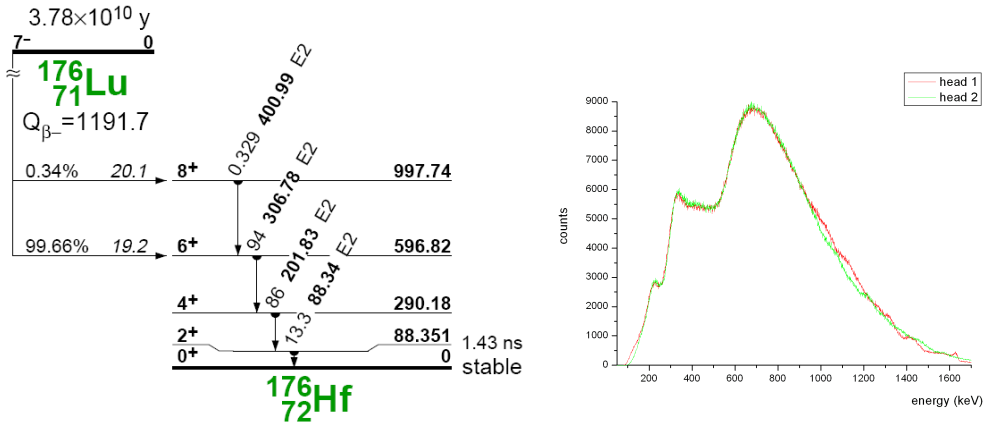

Figure 4.14: On the left: Decay scheme of ^{176}Lu into ^{176}Hf by β^--emission taken from [92]. On the right calibrated energy spectra of natural radioactivity from our Hilger LYSO matrices obtained by using our detector heads in single-count mode without source.

The shape of the background spectrum from LYSO is thought to arise from γ-ray absorption within the crystal itself, mostly by photoabsorption but also by Compton scattering. This results in a shift to higher energies of the background spectrum with respect to the β^-- energy curve, whose endpoint would be at 1.2 MeV. The peak at approximately 700 keV results most probably from the simultaneous detection the β^-- particle, with a most probable energy value of about 400 keV, together with the γ-lines with energies of 202 and 88 keV.

In order to estimate the background rate expected with a LYSO/PMT detector two energy windows typically installed in PET systems were considered: 150 - 850 keV and 350 - 850 keV. Within the wider energy window the activity density for each matrix is about 160 cps·cm^{-3}, whereas the narrower energy window yields about 50 cps·cm^{-3}.

Chapter 5

Algorithms for data analysis

5.1 Image reconstruction

Positron emission tomography is based on the detection of a pair of 180°-apart photons, generated by the annihilation of a positron with an electron. The aim of the reconstruction step is to reproduce the β^+ activity distribution starting from the measured coincidence data in the detectors. The tomograph, however, does not detect the β^+ emission point, nor the positron annihilation point but the two annihilation photons, and the acquired data are then the coincidence lines, named LOR's (Lines of Response). Among the main source of errors there are the positron range before annihilation, the photon attenuation by the materials in which the activity is embedded, and the deviation from γ-γ co-linearity which makes the annihilation point be outside of the straight LOR connecting the photon detection points. Angles different from 180° can be due either to the angular distribution of non-at-rest positron annihilations (see section 1.1) or to scattering of one of the photons before detection.

A pixel pair, belonging to opposed detectors in the planar tomograph, defines a detection tube. For simplicity, each detection tube defined by a pixel pair is collapsed onto its own axis and each LOR can be identified just from the two coordinates of each pixel in the array. The natural parametrization of PET data uses indices (d_a, d_b) of the two detectors in coincidence to store the two intersection points between the line and the opposite detectors. *Planogram* data storage is based on this parametrization. For rotating detectors, the information of view angle must be added and this increases the number of planogram bins by a factor equal to the number of acquisition views. As an alternative, raw data can be

interpolated into a *sinogram* parametrization, where LOR data are identified by their angle and position with respect to the tomograph axis. The choice of data parametrization depends on both the detector geometry and the reconstruction algorithm adopted. For planar non-rotating detectors, the planogram-based data coding offers the more compact parametrization.

Regarding the choice of reconstruction method, iterative algorithms offers an improved image quality with respect to analytic algorithms. This is obtained thanks to the possibility of an accurate modelling of the acquisition system and of the statistical distribution of the acquired data.

In our specific application the system is underdetermined, because of the limited angular acceptance of the prototype. In this case iterative algorithms provide an optimal reconstruction of at least one sub-system: the exact reconstruction of the image in all three dimensions cannot be achieved, but a good result in the xz central slices of the FoV can be obtained, i.e., in the plane parallel to the detectors surfaces. This limitation can be tolerable for the purpose of verifying the utility of in-beam PET[1], since the depth profile is the most critical issue in proton therapy, when the transversal section is well determined by the final collimator. Our primary goal is then to reach a detection capability of deviations of the order of the millimeter for the proton range, i.e., only for one direction.

Dealing with low statistics, it is essential to use effectively the limited data set. To avoid software rejection of data during the reconstruction, resulting in a reduced sensitivity, we adopt a 3D ML-EM reconstruction which uses all of the collected LOR's. Details of the implemented algorithm are given in the following sections.

5.1.1 ML-EM algorithm

Let $\lambda(x, y, z)$ be the spatial distribution of activity in the region of interest. The goal of the reconstruction is to obtain the discretized distribution of β^+ sources in the N voxels of the FoV:

[1]The effect of a partial-3D image reconstruction, however, is an aspect which will need to be deeply analyzed before a clinical trial. Due to a coordinate mixing effect, in facts, also the performance in the xz central plane is affected by some inaccuracy if the activity configuration is highly y-dependent. On the other hand, the larger dimensions foreseen for the clinical device and a further upgrade of the reconstruction algorithm [93] will reduce the influence of this effect. A quantification of the coordinate mixing effect will be then postponed to a more mature phase of the project, and only a brief comment on the present situation will be given later (sections 6.4, 7.6 and B.1) by a qualitative point of view.

$$\lambda_i = \int_{(voxel\ i)} \lambda(x,y,z)d\vec{x} \qquad i = 1, \cdots, N. \tag{5.1}$$

Let δ_j^* be the number of photons coincidence recorded in the tube j,where the j-index covers the detection tubes, $j = 1, \cdots, M$. The aim of reconstruction process is to find the distribution λ^{max} which maximizes the probability $P(\delta^*|\lambda)$ with the known δ^* distribution. This method is known as *Maximum Likelihood* (ML).

Let p_{ij} be the probability that photon pairs emitted from the voxel i are detected in the j^{th} tube.

We can indicate the number of photon pairs emitted from the i-voxel and detected in the j-tube with d_{ij}, whose mean value is $p_{ij}\lambda_i$:

$$\langle d_{ij} \rangle = p_{ij}\lambda_i \tag{5.2}$$

Direct and inverse relation between d_{ij} and δ_j^* can be expressed as follows:

$$d_{ij} = \delta_j^* \cdot \frac{p_{ij}\lambda_i}{\sum_k^N p_{kj}\lambda_k}, \qquad \delta_j^* = \textstyle\sum_i^N d_{ij} \tag{5.3}$$

The probability to obtain a certain distribution from the unknown activity is obtained as the product of several independent probabilities. As a consequence of the Poissonian nature of the radiation emission, the distribution of the $\{d\}$ values is then:

$$P(d|\lambda) = \prod_i^N \prod_j^M P(d_{ij}) = \prod_i^N \prod_j^M e^{-\lambda_i p_{ij}} \frac{(\lambda_i p_{ij})^{d_{ij}}}{d_{ij}!} \tag{5.4}$$

By considering all the possible decompositions of a detected δ_j^* value in the independent set of variables $\{d\}$, the probability to obtain the recorded δ^* distribution from the unknown activity λ can be seen as a function $L(\lambda)$:

$$P(\delta^*|\lambda) = \sum_{\{d\}} \prod_i^N \prod_j^M e^{-p_{ij}\lambda_i} \frac{(p_{ij}\lambda_i)^{d_{ij}}}{d_{ij}!} \equiv L(\lambda). \tag{5.5}$$

One possible succession converging to the problem solution is generated by the *Expectation Maximization* (EM) method [94]. A converging algorithm can be derived from the solution of the equation system $\frac{\partial[\ln\{L(\lambda)\}]}{\partial\lambda_i} = 0$. Each new λ_i is given by the previous element by

$$\lambda_i^{\nu+1} = \frac{\lambda_i^{\nu}}{\sum_j^M p_{ij}} \sum_l^M \frac{p_{il}\delta_l^*}{\sum_k^N p_{kl}\lambda_k^{\nu}}. \tag{5.6}$$

Other members of the EM algorithm family can be found by studying another equation system for maximizing the likelihood $L(\lambda)$, or by adding boundary conditions to the problem. The solution 5.6 is the most prominent in the literature. Further to concavity, convergence and speed, its main properties are:

- monotony: $P(\delta^*|\lambda^{\nu}) \geq P(\delta^*|\lambda^{\nu-1})$,
- retainment of the count number: $\sum_i^N \lambda_i^{\nu} p_i = \sum_j^M \delta_j^*$, and
- semi-defined positiveness: $\lambda_i^{\nu} \geq 0 \; \forall i = 1, \ldots, N$

at each iteration ν.

The initial distribution λ^0 is generally chosen uniform and equal to unity. A different choice mainly affects the convergence speed, but does not change the final result in a significant way. As a general rule for all the iterative algorithms, by starting from a uniform initial distribution, first iterations of reconstruction localize positions and dimensions of large structures. In the second phase, the algorithm searches all the local solutions in the image, but in this step the low frequency solution is not conserved. Iterative methods can then cause false emission source points in a uniformly empty field, if the number of iterations is excessive.

One important remark is that convergence is verified only when reconstructing noise-free data. By increasing too much the number of iteration in noisy data, the instabilities induced by noise corrupts the image estimates by high-frequency "checkboard-like" artifacts. Besides pre-reconstruction and post-reconstruction filtering, the only solution to avoid instabilities is to stop the algorithm after ν iterations, and use λ_i^{ν} as solution estimate. Methods to automatically estimate an appropriate number of iterations have been proposed, though usually implementations determine ν empirically. For our low-statistics reconstruction, we have adopted $\nu = 3$.

5.1.2 The probability matrix

Iterative methods could model the response of the tomograph and exploit the relationship between emission and detection. The reconstruction can be *a priori* optimized by modelling the detector, the scattering, several noise sources, and so

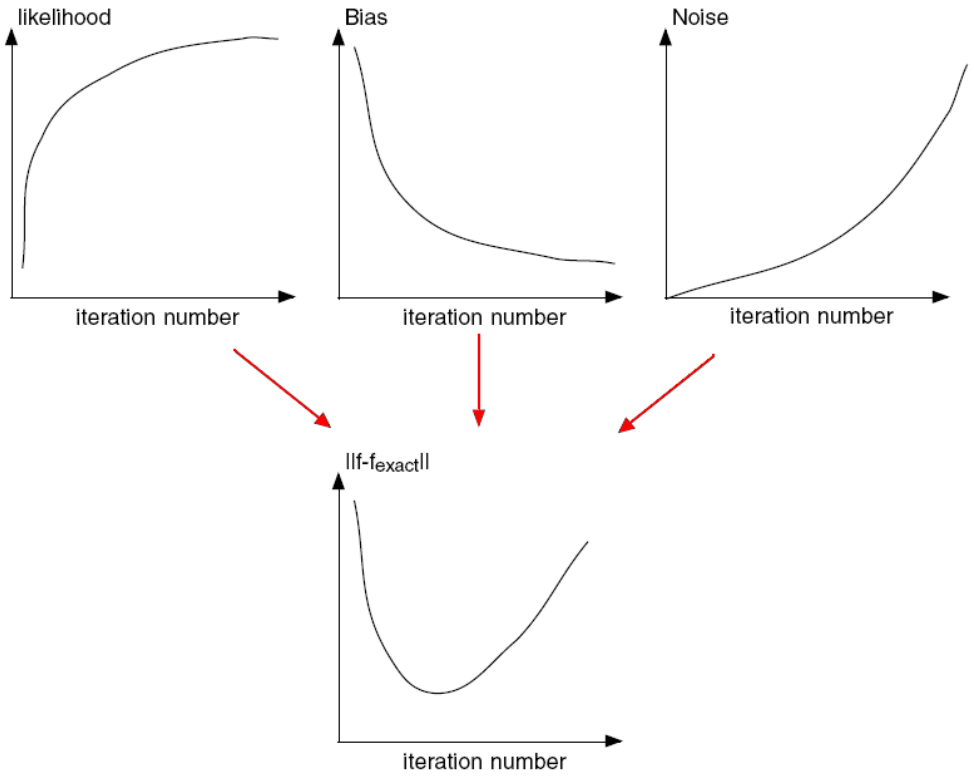

Figure 5.1: Typical convergence behaviour of the ML-EM algorithm: the likelihood is monotonical increasing, the bias introduced by the initial distribution is rapidly removed after few iterations, the noise instabilities increase with the number of iterations. The combined effect is that a too high number of iteration can produce large deviations of the reconstructed image from the real one.

on. The core of the iterative reconstruction is then the probability matrix $\mathbf{P}$ which correlates positron emission and photon detection.

The number of p_{ij} elements is given by the product between the number N of voxels that are used to divide the FOV and the number M of coincidence tubes. Such number of elements is usually too big to be stored, and then the single p_{ij} element is generally computed on-line during reconstruction steps when required. The traditional 3D EM reconstruction requires to make several times the computation of the voxel/LOR correlation matrix, or probability matrix p_{ij} and it is highly time-consuming. A commonly adapted solution is to rebin the 3D data set into 2D, so as to reduce the computational time by about two orders of magnitude, but

this introduces distortions to the point spread function (PSF). Fourier rebinning algorithms better preserve the reconstruction accuracy, but reintroduce long computation time just for the appropriate rebinning. Since our system has a very low number of LOR's and voxels with respect to the standard tomograph, storage of the probability matrix is not a problem, and no rebinning nor on-line computation are required.

Theoretically the $\mathbf{P}$ matrix should include all the parameters to exactly describe the tomograph. Simple, spatially invariant models are also adopted, solely based on geometric considerations, such as the length of the j^{th}-LOR that lies within the i^{th}-voxel. The geometric component, however, can be enhanced by incorporating spatially variant system response function, which can be analytically derived, measured or simulated. More recently, Monte Carlo simulations have been used to set up the entire system model, but this approach is limited by time-consuming computations required to obtain an acceptable statistical accuracy.

Initially, a purely geometrical version of the DoPET probability matrix has been used for the algorithm implementation. The approach was already adopted in positron emission mammography (PEM) with compressed breast [95] and had led to promising results. Recently, a more refined algorithm has been completed and the original algorithm is now used only for quick "on-line" reconstruction during data taking sessions. The last software version is the only described in detail below.

A Multi-Ray approach has been adopted for the generation of the probability matrix for the DoPET system. The method has been proposed and developed [96] for 3D PET reconstruction of data acquired with the planar-head YAP-(S)PET scanner. Detailed analysis on simulated and measured data have shown that the multi-ray method comes very close to the Monte Carlo results, if the crystal depth and crystal scattering is taken into account, i.e., if enough integration points are used.

Only minor changes were required to apply the method to our device, in particular crystal scintillator characteristics have been modified and planar head rotation during acquisition has been suppressed. By choosing appropriate rays, geometrical properties, crystal depth as well as physical properties such as crystal scattering and positron range can be incorporated in our model. At present, geometrical properties and crystal depth are incorporated.

Derivation of the model Let D_a and D_b be two planar detectors heads. Our goal is to calculate the matrix element $p_{ij} = P_{i,(a,b)}$ equal to the probability that

a positron emitted in voxel i is detected in the LOR j connecting the two crystals a and b located in D_a and D_b, respectively (see figure 5.2). The DoPET detectors are planar crystal arrays orthogonal to the y-axis and interactions can happen at any point of the depth d_y of the crystals. We assume that the voxel i is contained between the two detectors, i.e., within the y interval $[y_{b,in}, y_{a,in}]$, and we define the following vectors:

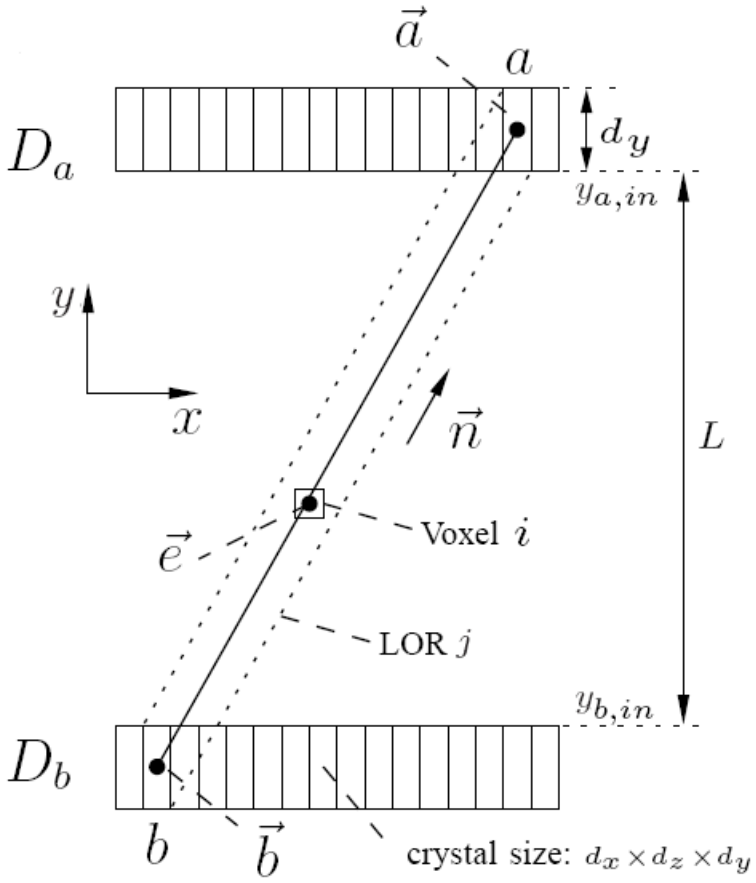

Figure 5.2: Geometry of the two planar detectors D_a and D_b.

- $\vec{e} = (x, y, z)$ as the point of emission of a positron
- $\vec{a} = (x_a, y_a, z_a)$ as the first interaction point in D_a
- $\vec{b} = (x_b, y_b, z_b)$ as the first interaction point in D_b

- $\vec{n} = (\sin\theta\cos\phi, \sin\theta\sin\phi, \cos\theta)$ as the unit vector along the momentum of the photon reaching crystal a. We assume colinearity, so the photon reaching crystal b has momentum along $-\vec{n}$.

We also define the distances $l_a = \|\vec{a} - \vec{e}\|$ and $l_b = \| \vec{b} - \vec{e} \|$ between the emission point and the position of the first interaction of the photons within the detectors, and the distances $l_{a,in}$ and $l_{b,in}$ between the emission point and the intersection of the LOR with the entry planes.

The general formulation for the computation of DoPET matrix element is the the 7D-integral $P_{i,(a,b)} =$

$$= \int_{\text{voxel i}} d\vec{e} \int_{4\pi} d\vec{n} \int_{\vec{a}\in D_a} dl_a e^{-\mu(l_a - l_{a,in})} s(\vec{n}, \vec{a}, a) \int_{\vec{b}\in D_b} dl_b e^{-\mu(l_b - l_{b,in})} s(\vec{n}, \vec{b}, b) \tag{5.7}$$

where μ is the linear attenuation coefficient of the 511 keV photons in the crystal and $s(\vec{n}, \vec{a}, a)$ is the probability that a photon oriented as $\vec{n}$ and having its first interaction at $\vec{a}$ is finally attributed to crystal a. $s(\vec{n}, \vec{a}, a)$ is a step function (1 if $\vec{a} \in a$, 0 otherwise), when scatter between crystal pixels is neglected. The same notation is used for detector D_b.

By neglecting scatter and doing some reasonable approximations for l_a and l_b [96] we can rewrite the matrix element as:

$$P_{i,(a,b)} = \left(\frac{cos\bar{\theta}}{L}\right)^2 \int_{\text{crystal } a} d\vec{a} \cdot e^{-\frac{\mu|y_a - y_{a,in}|}{\cos\theta}} \int_{\text{crystal } b} d\vec{b} \cdot e^{-\frac{\mu|y_b - y_{b,in}|}{\cos\theta}} k_i(\vec{a}, \vec{b}) \tag{5.8}$$

where k_i is the length of the intersection with voxel i of the line connecting the two points of first interaction $\vec{a}$ and $\vec{b}$and $\bar{\theta}$ is the polar angle of the line connecting the centers of the crystals a and b.

To calculate 5.8, a $n_x \cdot n_z$ point Gaussian quadrature is used for the integral on the crystal variables (x_a, z_a) and (x_b, z_b). A standard composite n_y point trapezoidal rule is used to approximate the integral over the exponential function along crystal depths y_a and y_b. The typical number of integration points in matrices used for reconstruction presented in the following chapters are $n_x = n_z = n_y = 8$. For the results presented here, we have a voxel size of $1.076 \times 1.076 \times 1.076$ mm^3 and a total number of $N = 42 \times 42 \times 42 = 74088$ voxels which is reconstructed from $M = 21 \times 21 \times 21 \times 21 = 194481$ LOR's.

5.1.3 Data corrections

In order to obtain quantitatively correct images, detector efficiency variations, scattered and random coincidences, attenuation and other physical effects must be accounted for. With the ML-EM algorithm, data pre-correction must be avoided because it would destroy its Poisson character and thereby could bias the reconstruction. This means that all physical effects should be included during reconstruction, in the system matrix. A fast, approximate, procedure consists of including only the most significant effects in the system matrix and pre-correct the data for all the other effect. This approach is particularly suitable for multiplicative corrections α_j (like attenuation or normalization for detector efficiency variations), which can be easily incorporated in the ML-EM iterations as shown by [97]:

$$\lambda_i^{\nu+1} = \frac{\lambda_i^{\nu}}{\sum_j^M \alpha_j p_{ij}} \sum_l^M \frac{\alpha_l p_{il} \delta_l^*}{\sum_k^N \alpha_l p_{kl} \lambda_k^{\nu}}. \tag{5.9}$$

When true coincidences data are extracted as the difference between the prompt and delayed coincidences (see sections 2.1 and 6.2), the Poisson nature of the data should be restored. One method (shifted Poisson [98]) is to reconstruct a new set of data, obtained from the acquired data plus an offset which will restore the equation $< \gamma_i^2 >=< \gamma_i >^2$. We preferred another method [99], which is developed on the basis of interpretation of convergence in the formula 5.6: when the reconstructed image tends to the real activity λ_i^{true} the sum $\sum_k^N p_{kl} \lambda_k^{\nu}$ tends to the projection data δ_l^{true}. However, if the δ_j^* are not pre-corrected for random background, we obtain that the progression factor in formula 5.6 will not tend to 1 but to $\sum_l^M p_{il} \frac{\delta_l^*}{\delta_l^{true}} / \sum_j^M p_{ij}$. A possible solution for restoring the convergence is then to correct the denominator so as it will tend to the real projection data δ_l^*, including randoms, rather than to δ_l^{true}. This can be implemented as:

$$\lambda_i^{\nu+1} = \frac{\lambda_i^{\nu}}{\sum_j^M p_{ij}} \sum_l^M \frac{p_{il} \delta_l^*}{\sum_k^N p_{kl} \lambda_k^{\nu} + r_l}. \tag{5.10}$$

Where r_l is a low variance estimate of the random background. The additional poissonian source of background deriving from ^{176}Lu (see sections 4.2.3 and 6.2) can be treated in the same way. By combining 5.9 and 5.10 and doing some simplifications, we finally obtain :

$$\lambda_i^{\nu+1} = \frac{\lambda_i^{\nu}}{\sum_j^M \alpha_j p_{ij}} \sum_l^M \frac{p_{il} \delta_l^*}{\sum_k^N p_{kl} \lambda_k^{\nu} + q_l / \alpha_l}, \tag{5.11}$$

where q_l is the summed contribution from random and ^{176}Lu coincidences.

Scattering correction have not yet been implemented, however preliminary analysis based on image profiles of point sources in air or embedded in PMMA have shown (see section 6.3) that the photons detected after scattering within the small phantoms used for proton irradiations are a small part of the total.

5.1.4 Final considerations

A system model with 512 integration points per crystal can be computed offline in about three days on a 3 GHz AMD Opteron Processor, and fits still in memory (4.1 GB if no detector symmetries are used, 1.5 GB when data storage optimization is applied). The computation of data correction and image reconstruction after the 3^{rd} iteration could be produced in few minutes only on the same processor. The previous version of reconstructed algorithm allowed a much faster computation of system matrix (purely geometrical), which can be produced on a standard laptop in few seconds. Anyway, data correction and image reconstruction steps needed several minutes for completion. Due to logistic necessities, however, the old version of the algorithm is still being used for online reconstruction, immediately after data acquisition, just for a rough check before switching to the next beam line configuration. However, rigorous off-line data analysis can be done only with the final version of the reconstruction algorithm.

5.2 The deconvolution algorithm

As was mentioned above, more than just image reconstruction is needed for clinical application: the correlation between dose and activity profiles must be extracted in order to derive from the measurements the information of dose distribution. At the beginning it was initially intended to pursue the interactive approach successfully applied at GSI, where the dose information is obtained by comparison of the measured activity data with a tunable simulation of the delivered beam. The symmetries and smoothness of activity distributions obtained during eye therapy irradiations brought us to explore an alternative and more satisfying solution based on an analytical approach. Under reasonable assumptions, the PET image can be described as a convolution of the dose distribution with a filter function. Parodi and Borfield [39] have developed a formalism to derive the filter function analytically from simulated data. The approach, fast and reliable, is developed assuming that the absorbing medium is homogeneous near the distal fall-off region,

but a generalization to inhomogeneous situations is also possible in the case of cyclotron-based proton facility with passive beam shaping systems as available at CATANA. Passive beam shaping systems, in fact, do not pose the complication of dynamic formation of the activity for each individually delivered pencil beam building up the total dose distribution, such as for some active beam scanning systems. The authors showed the substantial uniqueness of the filter in the [70, 230] MeV range of beam initial energy, within the activity reconstruction uncertainties. Based on the assumption that the convolution could be inverted, it should then be possible to derive the dose distribution from the measured activity through the filter approach.

The key point is the introduction of a family of analytical functions $\{\tilde{Q}\}$, defined as the convolution of a Gaussian with a powerlaw function P_ν.

$$\begin{aligned} & & G(x) &= \tfrac{1}{\sqrt{2\pi}} \exp -\tfrac{x^2}{2}, \\ \tilde{Q}_\nu(x) = G(x) * P_\nu(x), \text{where} & & P_\nu(x) &= \begin{cases} \frac{1}{\Gamma(\nu)} x^{\nu-1}, & \text{if x} \geq 0, \\ 0, & \text{otherwise.} \end{cases} \end{aligned} \tag{5.12}$$

Such functions results particularly suitable to approximate the dose and activity profiles [39, 100]. As an example, it can be mentioned that the Bragg curve of the full energy[2] therapeutic beam of the Northeastern Proton Treatment Center (NPTC) at Massachusetts General Hospital (MGH , Boston, USA) is reproduced by a single $\tilde{Q}$ function, while the linear combination of two $\tilde{Q}$ functions is enough for a good fit of the activity profile produced by such beam.

The filter which converts dose curves into the related activity distributions (or viceversa), is the solution of a Fredholm equation of the first kind. At this point the approximation of the distributions through $\tilde{Q}$ functions find its utility, since the convolution of two $\tilde{Q}$ functions is another $\tilde{Q}$ function, following the rule:

$$Q_{\nu_1}\left(\frac{x-a_1}{\sigma_1}\right) * Q_{\nu_2}\left(\frac{x-a_2}{\sigma_2}\right) = \frac{\sqrt{(\sigma_1^2+\sigma_2^2)}^{\nu_1+\nu_2-1}}{\sigma_1^{\nu_1-1}\sigma_2^{\nu_2-1}} Q_{\nu_1+\nu_2}\left(\frac{x-a_1-a_2}{\sqrt{(\sigma_1^2+\sigma_2^2)}}\right) \tag{5.13}$$

An algebraic computation can then extrapolate a $\tilde{Q}$ filter function from the $\tilde{Q}$ approximation of dose and activity distribution. Such method is much easier than solving exactly a Fredholm equation, and the approximations do not produce significant differences with the ideal result.

[2]We mean the beam obtained from the beam line without the introduction of passive range shifter or modulator wheel.

The DoPET collaboration has evaluated the feasibility of such an approach in the energy range of interest at CATANA; this energy range is somewhat more critical because of the larger uncertainties in the nuclear cross sections below 70 MeV which affect the precision of the activity distribution calculation.

The calculation of the filter function to unfold the dose distribution requires the a priori knowledge of both delivered dose and induced activity for some reference beams with a given energy distribution. The filter invariance (for each isotope species) with beam energy is required to assure the possibility to have an general algorithm which do not depend from the beam configuration. Before starting with the theoretical evaluation of activity and dose distributions, we have tested the reliability of this approach by extrapolating a $\tilde{Q}$ global filter from the experimental full energy dose and activity profiles. Such filter has been then applied to the dose profiles of other measurements performed. The results obtained were encouraging enough to justify the effort to explore a theoretical way for the filter evaluation, which is described below.

The isotope relative contributions to the total activity profile is determined by the irradiation and observation times: the slower we irradiate, the more nuclei will be decayed before starting the acquisition, the longer we acquired, the more decays will be detected. Since isotopes have different lifetimes, depending on the irradiation[3] and acquisition time, the relative contribution to the overall activity will be different. Moreover, since the shape of the activity distribution of a specific radioisotope is determined by the specific energy dependence of its production cross section, a change in the isotope relative contributions will correspond to a change of the overall activity distribution shape. The linear combination of each isotope filter would produce the proper filter for deriving activity distribution from dose distribution. Each weight coefficient of the linear combination is the fraction of activity assigned to the given isotope for the specific acquisition time.

The theoretical evaluation of the filter function requires the simulation of both the dose curve and the associated activity profile, for any proton energy spectrum of interest. The semi-analytical model already described in section 3.3, is reliable enough to this purpose. The estimate of the β^+ emitters is then smoothed with a Gaussian point spread function of 1.7 mm FWHM (see chapter 6) to account for the spatial resolution of the PET prototype.

The first step required is an evaluation of the spread of filter function parameters to assure the validity of energy-independence approximation for each isotope filter. Simulations of dose and activity profiles of monoenergetic proton beams

[3]This contribution is neglected in the present work.

have been performed for seven initial energies, spanning the range [40-70] MeV. Data have then been used to compute the filter functions for the two main reactions inside PMMA inducing a β^+-activation of the target: ^{12}C(p, p+n)^{11}C and ^{16}O(p, p+n)^{15}O.

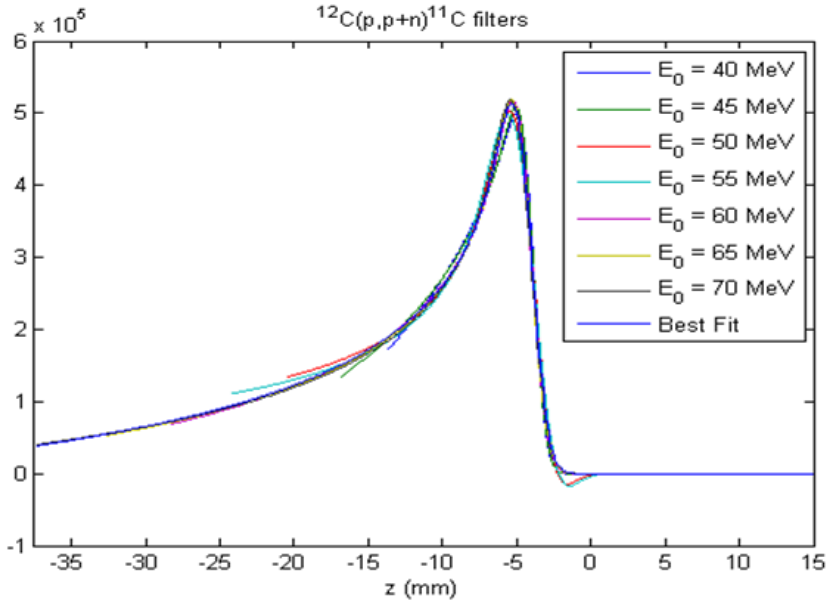

Figure 5.3: Filter functions evaluated for ^{12}C(p, p+n)^{11}C reaction at different energies.

In figure 5.3 there are shown the filters calculated for ^{11}C activation: all the filters coincide within the numerical uncertainties of the profiles fitting process. The same happens for the other β^+ emitter analyzed, ^{15}O. These results support the feasibility of the unfolding by means of dose filtering. An average of the seven $\tilde{Q}$ filters is used as energy-independent radioisotope filter in the following steps.

As a further check, simulated activity profiles produced by monoenergetic beams have been compared with those obtained as filtered dose using the average filter. Results shown in figure 5.4 confirm the agreement between simulation and filtering process using a unique filter function at each beam energy.

Figure 5.5 then shows the activity profiles predicted by applying the filter to dose profiles measured for energy modulated beam configurations (see figure 7.3). Shifts of 2 mm and 1 mm in dose distal edge correspond to equivalent shifts in the distal edge of predicted activity, then in principle 1 mm shifts could be detected by a PET acquisition.

The comparison of filtered dose with measured activity will be presented in detail in section 7.5, and conclusions will be drawn.

The work is still in progress: further possible optimization are the selection of a different cross section data set or a Monte Carlo approach (either with FLUKA or with a upgraded version of GEANT4), in order to improve the agreement between the analytical calculation and experimental data. Moreover, we underline again that the fundamental step of inverting the convolution procedure must be concluded before being able to state the feasibility of dose unfolding from DoPET data.

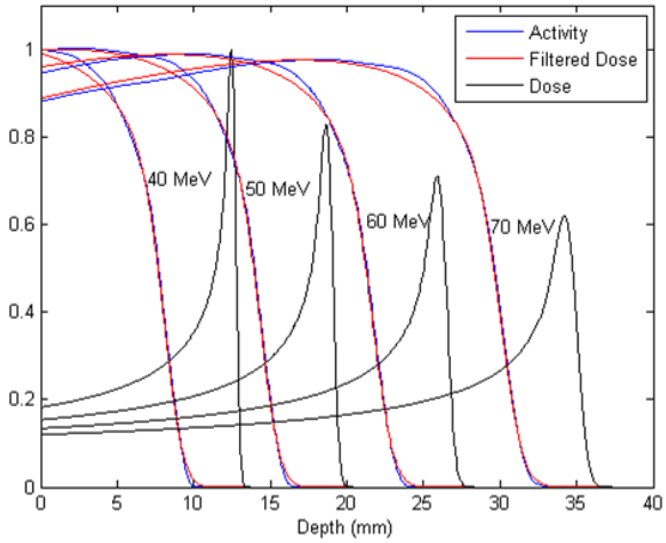

Figure 5.4: Normalized in-depth profiles (integrated over the whole lateral field extension) of simulated ^{11}C activity compared to filtered dose profiles. In-depth profiles of simulated dose are also shown.

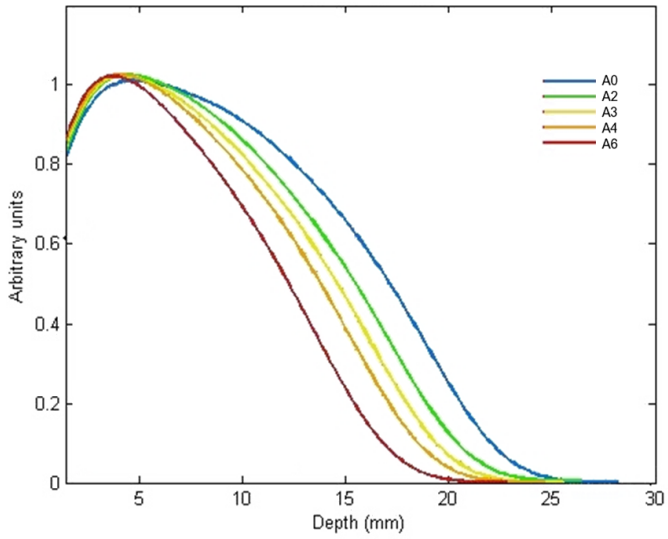

Figure 5.5: Convolution result of $\tilde{Q}$-based expression of dose profiles with the $\tilde{Q}$-based expression of the filter function. Experimental dose profiles used for the computation are the 10.8 mm spread-out Bragg peaks shown in figure 7.3. Legend label correspond to the different Bragg peak depths in PMMA phantom: A0=26.4 mm, A2=24.7 mm, A3= 23.7 mm, A4=22.8 mm, A6= 21.0 mm.

Chapter 6

Performances of the DoPET prototype

After the detector optimization described in chapter 4, the final assembly has been reached and a complete calibration of the detector has been performed. Before presenting results of the calibration measurements, some information on detector configuration is given.

The characteristics of the PMT used for each head are listed in the table 6.1. The values of high voltage supply have been chosen in order to best profit of the dynamic range of the ADCs. Slight adjustment (of few tens of volts) are necessary depending on the supply used to power the electronics boards. Therefore energy calibration and noise spectrum acquisition must always be performed before a new set of measurements.

head	anode luminosity [A/lm]	anodes gain spread [max/min]	dark current [nA]	PMT supply [V]
#1	44.1	2.1	1.86	1015
#2	160.0	1.7	0.78	840

Table 6.1: Specific parameters of the PMT used in the final detector.

The matrices are composed by 21×21 LYSO finger crystal, which determine about $1.94 \cdot 10^5$ LOR's in a FOV of $4.5 \times 4.5 \times 14$ cm^3. Relative distance of the heads was usually set to 14 cm. Standard pixel calibration and high energy cut (850 keV) are applied before data analysis. Two low energy cuts (150 keV or 350 keV) have been evaluated.

6.1 Energy Resolution

For the calibration in energy of the detector, sources centered in the field of view have been used, so as to obtain a good uniformity in pixel irradiation. Once the LUTs have been registered, each coincidence event is assigned to the proper pixel pair. Pixel spectra are then built for each head, and the photopeak position for each pixel spectrum is used to evaluate the energy scale factor for the events belonging to the selected pixel. All the events are then properly scaled and summed up together to obtain a calibrated spectrum as those shown in figure 6.1.

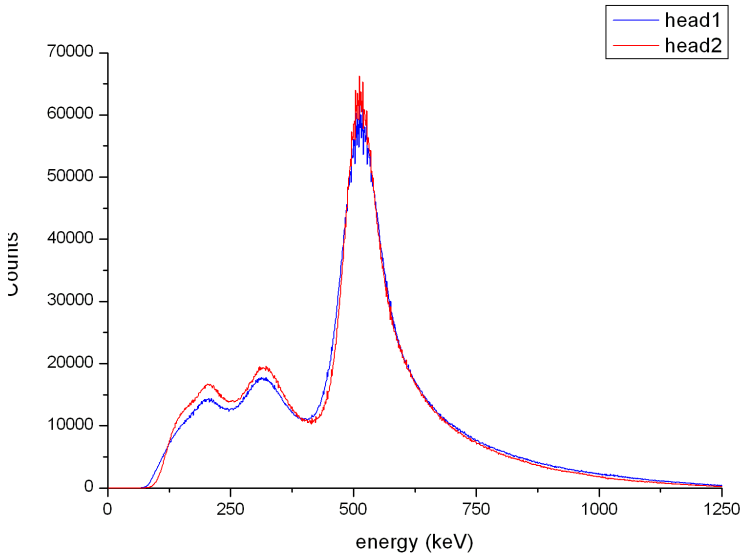

Figure 6.1: Calibrated energy spectra for ^{22}Na point-source at the center of the FOV.

Several source activities and both ^{18}F and ^{22}Na sources have been used with similar results. Two peaks are visible on the Compton continuum, and they correspond to the 201 keV and 306 keV γ-emissions of ^{176}Lu contained in the scintillator crystals. The events occurrence is too high to be explained as ^{176}Lu-^{176}Lu random coincidences, which are only 2 per second. It is shown in the next section that the registered events are true coincidence events deriving from a single ^{176}Lu decay.

The long tail above the photopeak energy has no clear explanation. Its presence in the ^{18}F spectrum exclude a contamination derived from the Compton continuum of the 1.022 MeV γ-emission of ^{22}Na. On the other side, the tail is almost

totally absent from the pure ^{176}Lu coincidence spectrum. A combined source-background effect has been also excluded by changing the used activity for 511 keV sources: while at fixed number of acquired events the ^{176}Lu contribution almost disappear[1], the high energy tail is still present.

The matrix reprocessing from aluminized pixel to white epoxy reflector material is known to produce some degradation effect in the detector material in terms of crystal light yield (see figure 4.11). In the same way, a degradation of linearity in light yield response cannot be excluded. As alternative, non-linearities can be also introduced by the acquisition system.

Before the evaluation of the energy resolution, ^{176}Lu events are acquired for long times from a PET acquisition with no source. The calibrated background spectrum is then scaled to the acquisition time of the calibration measurement, and it subtracted to the β^+ source spectrum. A gaussian fit is performed on the resulted energy spectrum, and the FWHM obtained from the fit is presented in table 6.2.

head	energy resolution (FWHM)
# 1	15.6 ($\pm$0.4) %
# 2	15.2 ($\pm$0.4) %

Table 6.2: Energy resolutions of the two detector head, measured from the calibrated ^{22}Na spectra shown in figure 6.1.

In the hypothesis that the tail events just derive from energy calibration non-linearities, the present analysis set the upper energy threshold to 850 keV to include a large part of the tail events. The choice of the lower energy threshold will be discussed presented in the following sections.

6.2 Random coincidences and ^{176}Lu radioactivity

In order to produce a planogram of the real coincidences, one should deal with all the possible sources of noise during the acquisition. First of all, one must take into account the possibility that a single event randomly happens within the coincidence time window generated by another single one.

[1]When comparing acquisitions which has collected the same statistics, a higher β^+ activity requires a minor time for measurement completion. Since the ^{176}Lu activity is almost constant in time ($T_{\frac{1}{2}} = 3.8 \times 10^{10}$ years), a shorter acquisition reduces the number of ^{176}Lu events collected.

The random coincidences occur to a rate which is $R_c = A_1 \cdot A_2 \cdot 2\tau_c$, where A_i are the rate of acquired events in single mode, and $\tau_c = 10\ ns$ is the coincidence time window. The acquired event rate -in absence of other sources of background- would be then $D_c = T_c + R_c$.

The random circuit described in section 2.1 allows one to estimate -during the acquisition itself- the occurrence of random coincidence for each specific LOR, i.e., for each planogram bin [x1][z1][x2][z2]. Such information is stored in the listmode file, and can be used during the generation of the planogram for the appropriate correction of the random event contribution from each LOR.

Random coincidences, however, are not the only source of noise in our acquisitions. As described in the section 4.2.3, the major drawback of LSO and LYSO crystals is the natural occurrence of the radioisotope ^{176}Lu within the crystal material.

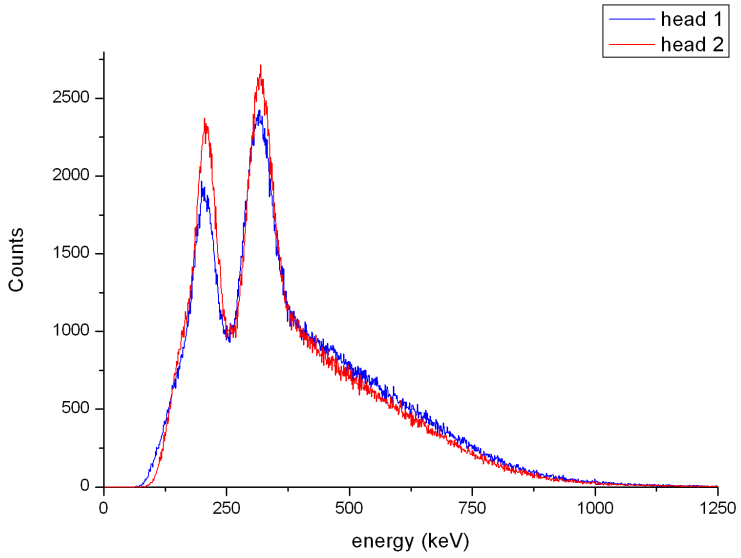

Figure 6.2: Calibrated energy spectra for ^{176}Lu source contained in the crystal itself, when acquired in coincidence.

Since the self-triggering event rate measured for each matrix is about 8500 cps, (see section 4.2.3), the random coincidence rate expected from ^{176}Lu decays within a 10 ns coincidence window should be $R_c^{Lu} = A_1^{Lu} \cdot A_2^{Lu} \cdot 2\tau_c = 1.5$ ev/s.

Since the measured background coincidence rate is much higher (see below), it has been drawn the hypothesis that the measured coincidence are due by the

simultaneous detection of the same decay event by both heads, i.e., the β^- is detected within the pixel crystal where the decay has happened, while (at least) one emitted γ is detected in other crystals of the opposite detector.

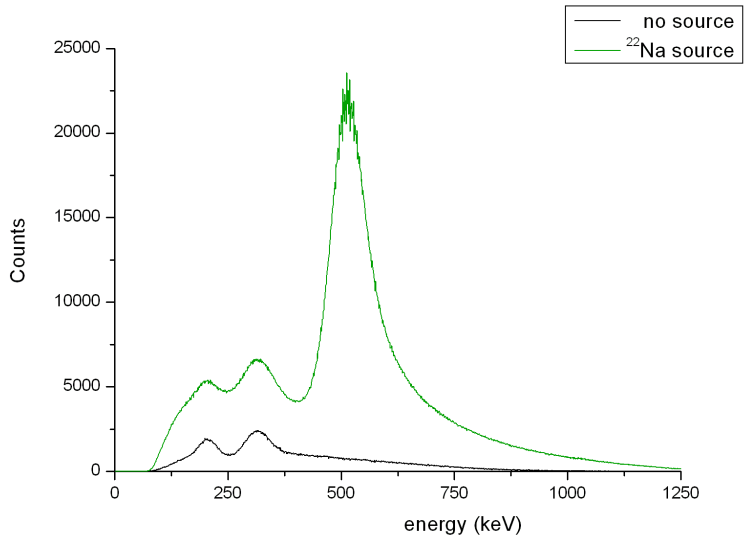

Figure 6.3: Comparison between the calibrated energy spectra of head 1 with and without ^{22}Na source (3 hours-long PET acquisitions).

In order to demonstrate such thesis, several acquisition have been performed with the detector heads placed at various distances from each other, with no source inserted in the FOV. Two energy windows were considered: 150 - 850 keV and 350 - 850 keV, corresponding to a selection of events within 511 keV$\pm^{66\%}_{70\%}$ and 511 keV$\pm^{66\%}_{31\%}$, respectively.

Results of raw data acquisition rates and event contamination after the energy cuts are shown in table 6.3. The coincidence rate decrease with the increasing distance between the detector heads, and drop to less than 1 ev/s when the detectors are placed very far from each other. The trend is consistent with a $\frac{1}{r^2}$ decrease in a first approximation, as shown in figure 6.4.

While the ^{176}Lu-^{176}Lu random coincidence are negligible, when detector heads are placed at 14 cm distance the ^{176}Lu self-coincidences introduce a significant background rate which must be appropriately dealed with during the data processing and image reconstruction.

acquisition setup	hardware trigger rate $>\approx$70 keV [cps]	selected rate [150,850] keV [cps]	selected rate [350,850] keV [cps]
0.3 cm*	1385	1103	129
8.0 cm	147	108	13
10.0 cm	102	74	9
14.0 cm	58	42	6
14.0 cm$^{\diamond}$	61	43	6
20.0 cm	31	21	3

*The Teflon layers for light reflection and the black tape for light shielding prevent a perfect contact between scintillator crystals

$^{\diamond}$The anticorodal phantom support has been introduced within the FOV, in order to evaluate backscattering effects.

Table 6.3: Contamination of coincidence rates due ^{176}Lu self-coincidence. Average rate, evaluated on acquisition few hours long. Statistical fluctuations produce uncertainties lower than 1 ev/s for each of the presented measurements.

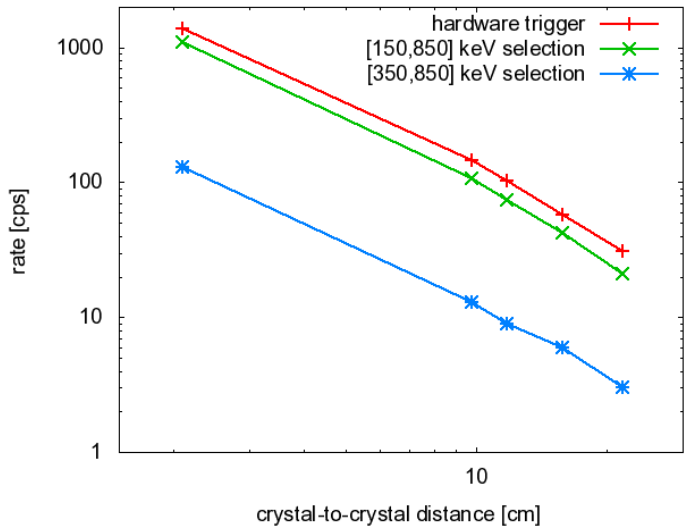

Figure 6.4: Plot of data presented in table 6.3. Crystal-to-crystal distance is defined as the head-to-head distance plus half of the crystal depths (0.9 cm + 0.9 cm). Logarithmic scale is used to put in evidence the power-law trend.

The coincidence rate during a general acquisition is then

$$\begin{aligned} D_c^{all} &= T_c^{all} + R_c^{all} = \\ &= T_c^{\beta^+} + T_c^{Lu} + R_c^{all} \end{aligned}$$

Since $R_c^{all} = A_1^{all} \cdot A_2^{all} \cdot 2\tau_c$ and $A_i^{all} = A_i^{Lu} + A_i^{\beta^+}$, doing multiplications one obtain that

$$R_c^{all} = R_c^{Lu} + R_c^{\beta^+} + (A_1^{Lu} A_2^{\beta^+} + A_2^{Lu} A_1^{\beta^+}) \cdot 2\tau_c$$

and then

$$D_c^{all} = T_c^{\beta^+} + T_c^{Lu} + R_c^{\beta^+} + R_c^{Lu} + R_c^{\beta^+/Lu},$$

where $R_c^{\beta^+/Lu} = (A_1^{Lu} A_2^{\beta^+} + A_2^{Lu} A_1^{\beta^+}) \cdot 2\tau_c$.

From the acquisition data one can estimate D_c^{all} and R_c^{all}. From an acquisition without source, it is possible to measure $D_c^{Lu} = T_c^{Lu} + R_c^{Lu}$ and R_c^{Lu}. As a conclusion, we can isolate the true coincidences for a proper image reconstruction by using acquired data and a background acquisition. In fact $T_c = D_c^{all} - D_c^{Lu} - R_c^{all} + R_c^{Lu}$. Since the low A_i^{Lu} rates produce a very small number of random coincidences, R_c^{Lu} contribution is neglected in the practical implementation and we use:

$$T_c = D_c^{all} - (D_c^{Lu} + R_c^{all}). \tag{6.1}$$

After the integration of the rates for each LOR j, using the notation introduced in chapter 5, the background correction can be written as:

$$\delta_j^{ideal} = \delta_j^* - (r_j + l_j). \tag{6.2}$$

The actual implementation of correction for Poisson background contamination has been already described in section 5.1.3.

6.3 Efficiency

6.3.1 Overall detection efficiency

The efficiency of the DoPET tomograph is evaluated through the acquisition of a β^+ point-source of known activity, placed in the center of the field of view. The efficiency is defined as the ratio between the number of detected events (after random and lutetium corrections) and the number of decays which are known to occur for the used source during the same time interval.

A ^{22}Na point-source of 960 kBq has been placed at the center of the FoV (CFoV) and a statistic of $6.3 \cdot 10^5$ coincidences has been collected for each measurement. A branching ratio of 0.9055 has been considered for β^+ emission from ^{22}Na decay. Results are shown in table 6.4, and compared with the estimates derived from Monte Carlo simulations.

	10 cm		14 cm		20 cm	
	exp.	sim.	exp.	sim.	exp.	sim.
E> 150 keV	1.7 %	2.7%	1.0%	1.6%	0.5%	0.8%
E> 350 keV	1.2 %	2.2%	0.7%	1.3%	0.4%	0.6%

Table 6.4: Overall CFoV detection efficiency evaluated at different distances of the detector pair. Comparison with simulation results are shown.

The simulation results overestimated the detection efficiency, while an underestimation was expected from geometrical considerations (see page 37). Possible explanation of such disagreement could be in the energy cut: in the simulated energy spectra, in fact, the high energy tail shown in figure 6.1 is not taken into account. A second possibility can be an overestimation of the coincidence window τ_c, which cannot be directly accessed for measurements in the acquisition board. Work is still ongoing for the comprehension of the simulation results.

At the preferred distance of 14 cm, a measurement at the edge of the FOV (EFoV) along the x direction has been also performed, in order to estimate the spread in efficiency from the proton entrance surface to the Bragg peak position in the irradiation measurements (see next chapter). For [150-850] keV and [350-850] keV energy windows, EFoV efficiency obtained are 0.8% and 0.5%, respectively.

Other measurements have been performed in the clinical configuration for eye-therapy, i.e., with a head-to-head distance of 20 cm and with the target region asymmetrically placed along the y direction. Results are shown in table 6.5.

(5 + 15) cm	CFoV	EFoV
E> 150 keV	0.31 %	0.16%
E> 350 keV	0.22 %	0.11%

Table 6.5: Overall detection efficiency evaluated in a clinical configuration of the detector geometry.

All the measurements presented here have been repeated with the ^{22}Na point-source embedded in 7 cm $\oslash \times$ 7 cm PMMA cylinder, obtaining a relative decrease

in detection efficiency of about 27% for the [150-850] keV energy selection and of 26% in the [350-850] keV energy window, when the head-to-head distance was set to 14 cm. These variations should be compared with the estimation of the fraction of photons that can scatter in the PMMA cylinder.

The probability that one photon emitted at x from the phantom surface exits the cylinder without interacting is $e^{-\frac{x}{\lambda}}$, the maximum probability for the opposed photon is $e^{-\frac{7\ cm-x}{\lambda}}$. With a photon scattering length of about 10 cm in PMMA, then more than $e^{-\frac{7\ cm}{\lambda}} = 50\%$ of emitted photons pairs exit the cylinder without being scattered, and then the remaining 50% of coincidences could be detected in the wrong LOR or not detected at all. The efficiencies measured in PMMA, then, indicate that only 23% of the scattered events are retained for image reconstruction after [150-850] keV energy selection. The analysis of the asymmetrical configuration 5 + 15 cm shows an even more favorable scattering/true ration in the events selected for reconstruction.

6.3.2 Normalization of planar sensitivity

Due to unavoidable crystals non-uniformities and to the low statistics available for image reconstruction, a normalization of the detection efficiency of each pixel is mandatory, in order to reduce reconstruction artifacts. Rather than single pixel efficiency, their combined efficiency for each LOR is easier to measure and to introduce as correction in the reconstruction algorithm. The sensitivity normalization is performed by acquiring a β^+ source whose activity distribution is known a priori[2]. The expected (voxelized) activity is projected into detector LOR's through the probability matrix, and the coefficient for the normalization of the j^{th}-LOR is then extrapolated as the ratio

$$c_j^{\epsilon} = \frac{\delta_j^*}{\sum_w^N p_{wj}\lambda_w}.$$

In order to keep constant the overall statistics, the correction coefficients will be normalized as follows:

$$\alpha_j = \left(\frac{\sum_l^M \sum_v^N p_{vl}\lambda_v}{\sum_k^M \delta_k^*} \right) c_j^{\epsilon}$$

[2]Quantitative calibration could be also performed if the total activity of the source is also known. Work is still ongoing on this step.

so that reconstructed images will retain quantitative information of the acquired coincidences:

$$\sum_j^M \frac{1}{\alpha_j}\delta_j^* = \sum_j^M \left[\left(\frac{\sum_k^M \delta_k^*}{\sum_l^M \sum_v^N p_{vl}\lambda_v}\right)\frac{\sum_w^N p_{wj}\lambda_w}{\delta_j^*}\delta_j^*\right] =$$

$$= \left(\frac{\sum_k^M \delta_k^*}{\sum_l^M \sum_v^N p_{vl}\lambda_v}\right)\sum_j^M \left[\sum_w^N p_{wj}\lambda_w\right] = \sum_k^M \delta_k^*.$$

The activity distribution chosen as reference is a uniform, pure β^+, parallelepipedic source, with the front section larger than the detector dimension so to avoid border effects. The source has been realized by a thin lucite rectangular frame with a cavity sized 66 mm $\times$ 66 mm $\times$ 3.5 mm (15.25 ml). A schematic drawing of the phantom is shown in figure 6.5. The cavity has been filled with a water solution of ^{18}F-FDG and placed at the center of the FOV.

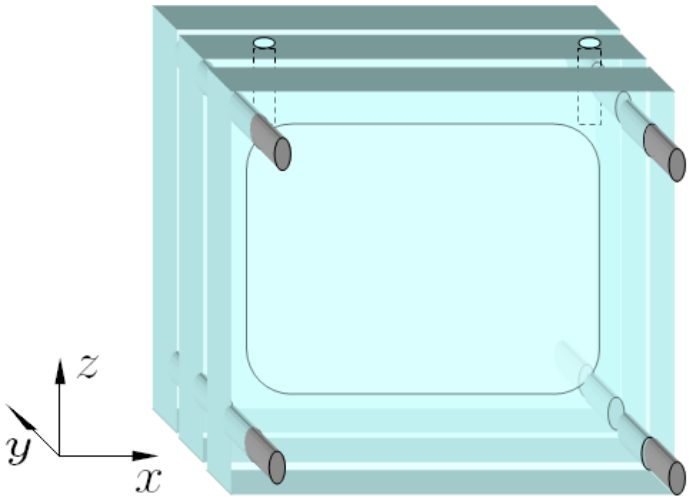

Figure 6.5: Schematic drawing of the rectangular frame used to produce a uniform planar ^{18}F source.

In figure 6.6 a typical distribution α_j of normalization coefficients is presented, as obtained with an acquisition of $6.3 \cdot 10^7$ events with the set-up described.

The large spread of the distribution confirms the necessity of sensitivity corrections. The positive effect of sensitivity normalization on the following data acquisition is shown by the example in figure 6.7.

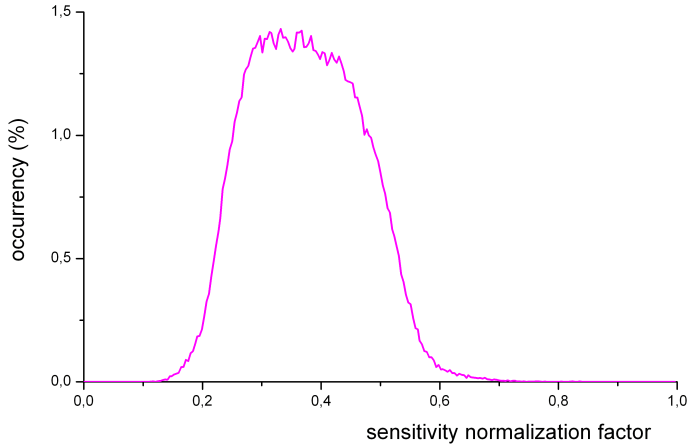

Figure 6.6: Typical spread of the sensitivity normalization coefficients α_j when a [150,850] keV energy selection is applied. The distribution has mean value of 0.4, and a standard deviation of 0.1 (25% spread).

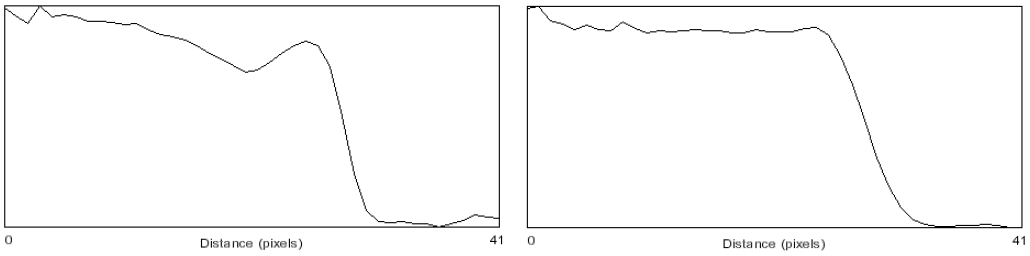

Figure 6.7: Central slice in the xz plane of the reconstructed image of a uniform cylindrical phantom (syringe). A [150,850] keV energy selection is applied before image reconstruction. On the left the raw data have been used, on the right the sensitivity normalization procedure has been applied before reconstruction. The normalized data produce a more uniform image.

6.4 Spatial Resolution

The 3-D spatial resolution of the DoPET detector has been evaluated as the FWHM of a reconstructed image from measurements of a point-like ^{22}Na source. The source dimension is about 1 mm diameter, and it is embedded in a thin lucite support. One can safetely assume that the source size is dominated by its physical

dimension, since the average range of ^{22}Na positron[3] in lucite is less than 0.5 mm.

The source has been placed at the center and at the edge of the FOV to evaluate also the spread in spatial resolution along the direction of proton penetration. Both an empty support and a PolyMethyl-Methacrylate (PMMA) cylindrical block have been used, to evaluate degradation introduced by scattering and attenuation from PMMA. The PMMA cylindrical support derives form the same PMMA bar cut to make the cylindrical phantoms used for the validation with proton irradiation (see chapter 7), and they are placed with the symmetry axis along the x direction.

About $6 \cdot 10^5$ events have been acquired for each measurement. Cubic voxels sized 1.25 mm^3 or 0.16 mm^3 were used for images reconstruction. The iterative algorithm is stopped at the third iteration.

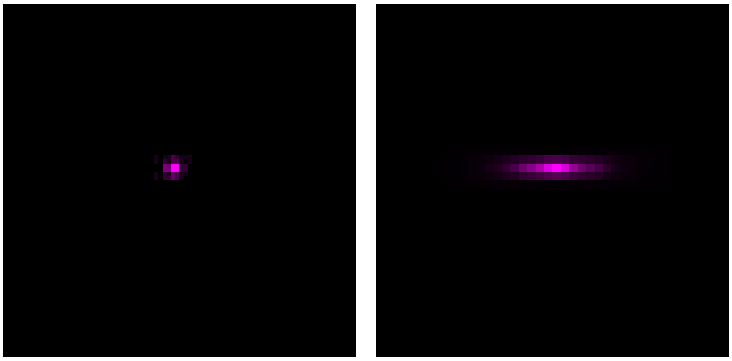

Figure 6.8: Central reconstructed slice (1.076 mm thick) in the xz (left) and yz (right) planes. Data acquired with a ^{22}Na point-source placed in air at the center of the field of view.

Results are summarized in tables 6.6, 6.7 and 6.8.

Both energy selections analyzed (150-850 keV and 350-850 keV) produce similar results, demonstrating that lutetium background events and photon scattering introduce negligible effects. Along the y direction, which is the one orthogonal to the detector faces, the spatial resolution is poor. This happens because of the small sensitive area of the detectors with respect to their relative distance, that causes a very limited angular coverage. The effect has been already analyzed in [110], showing that the image elongation is limited only when the detector gap angles are smaller than 100^o. By a rough count, our small prototype has gap angles ranging from 130^o to 146^o depending on the symmetry axis[4] adopted. The coordi-

[3]The endpoint of ^{22}Na β^+ spectrum is 0.545 MeV.

[4]Diagonal or side of the squared detector head.

Measure type		FWHM x	FWHM z	FWHM y
media	lower energy cut	(mm)	(mm)	(mm)
air	E $>$ 150 keV	1.7	1.7	13
air	E $>$ 350 keV	1.7	1.7	13
PMMA	E $>$ 150 keV	1.7	1.7	13
PMMA	E $>$ 350 keV	1.7	1.7	13

Table 6.6: Summary of the reconstruction results for a single point source at the center of the field of view. The upper energy cut is 850 keV in all the analysis.

nate mixing effect produced by the image elongation is then much pronounced in our case. However, thanks to the irradiation configuration adopted during validation measurements[5], which is y-independent within about 12 mm from the central axis, we can neglect the coordinate mixing effect by simply focussing on the central row of the central xz slices of the reconstructed images. In the following, only few examples of xy slices from reconstructed images will be shown for completeness.

The embedding of the source in a PMMA cylinder does not significantly degrade the spatial resolution. No remarkable improvements in resolution are obtained with higher energy cuts (see table 6.6). Since results are good also with a less stringent energy selection (150 - 850 keV), the latter has been preferred for all the following analysis, and also for the reconstruction of the measurements after proton irradiation.

Measure type		FWHM x	FWHM z	FWHM y
position	media	(mm)	(mm)	(mm)
center of FOV	air	1.7	1.7	13
center of FOV	PMMA	1.7	1.7	13
phantom edge	air	1.7	1.7	16
phantom edge	PMMA	1.7	1.8	15

Table 6.7: Summary of the reconstruction results for a single point source in different position of the field of view (energy threshold 150 keV).

In absence of a positioning setup, it was meaningless a fine scanning of spatial resolution along the x axis, since no precise correlation between result and FOV position was possible. However the spatial resolution in two specific position of

[5]Uniform 25 mm $\oslash$ irradiation impinging on a flat surface. See next chapter.

the x axis have been compared so as to determine the range of variation. The phantom edge is the position where the protons enter the PMMA cylinder, and thanks to the mechanical setup this is few mm before the end of the FOV. The center of the FOV has been made to roughly correspond to the end of the activity distribution produced by proton irradiation, while the phantom edge is obviously where the activity distribution starts. The spatial resolution, when shifting along the x direction, show a rather limited variation for x and z dimensions. Based on detector symmetries, similar conclusions can be drawn for shifts along the z direction.

Measure type		FWHM x	FWHM z	FWHM y
position	head distance	(mm)	(mm)	(mm)
center of FOV	10 cm	1.8	1.8	11
center of FOV	14 cm	1.8	1.7	13
center of FOV	20 cm	1.7	1.7	15
phantom edge	10 cm	1.7	1.9	13
phantom edge	14 cm	1.7	1.8	15
phantom edge	20 cm	1.7	1.7	18

Table 6.8: Summary of the reconstruction results for a single point source at different distances (energy threshold 150 keV, source embedded in PMMA).

As a preliminary evaluation for the performances of a future clinical device (at least 10 cm $\times$ 10 cm heads, 20 cm far from each other, see chapter 8), the spatial resolution of the DoPET prototype has been evaluated also at different head distances. The shorter distance simulates the angular coverage of the larger device (110^o-130^o gap angles) in the evaluation of the image elongation along y, while the 20 cm distance is the right one to estimate the influence of parallax errors in the future detector. The results do not significantly change with head distance, thus confirming than our detector resolution is dominated by the pixel size. It should be reminded that a higher detector efficiency and a more limited image elongation are the main reason for requiring a larger device as clinical detector, rather than a better spatial resolution.

Chapter 7

Validation on plastic head-phantoms

The possibility of test measurements with proton beams has been kindly offered by the CATANA group at INFN-LNS. The beam of the INFN-LNS superconducting cyclotron has a maximum proton energy of about 62.5 MeV, and it is passively conformed to the chosen dose configuration. Dosimetry measurements are needed before each run, in order to obtain an accuracy better than 0.5% in the planning of dose delivery. The variation of dose/(monitor unit) registered on four consecutive days is within 3%.

One run of measurements with carbon ion beams has been also performed, in order to explore a wider range of application of the DoPET prototype. The carbon ion beam has been kindly provided by the HIT group, using the GSI synchrotron in Darmstadt. Preliminary results with the carbon ion beams are presented on appendix B.

7.1 Plastic phantoms

The validation of DoPET detector has been performed through the measurement of the β^+-activation of PolyMethyl-Methacrylate (PMMA, $C_5H_8O_2$, ρ = 1.18 g/cm^3) phantoms undergoing ion beams irradiation, mainly proton beams.

The plastic phantoms used are smaller than required for emulating a human head. Larger and more refined phantoms are planned to be used only with the clinical version of DoPET, which will have a 10 cm $\times$ 10 cm FoV. Two kinds of phantoms have been used in the measurements.

The first type is a PMMA cylinder, 7 cm $\oslash$ and 7 cm height. The flat circular base of the cylinder has been used as orthogonal surface for the impinging ion

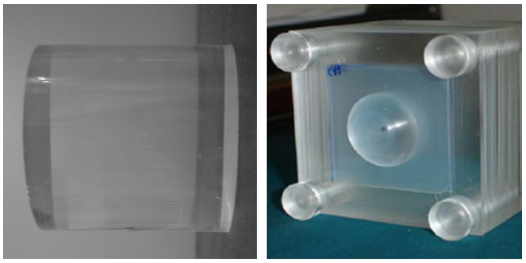

Figure 7.1: Pictures of the PMMA phantoms used: geometry is oriented as in the reconstructed image, with proton impinging from the left. Left: cylindrical phantom. Right: eye-shaped phantom.

beam. Except for the first measurement run, the phantom entrance surface was placed 5 mm within the edge of the FOV with a reproducibility error below 0.5 mm. Five copies of this cylindrical phantom have been alternated during irradiation, in order to save time while waiting for phantom de-activation. All derive from the same PMMA bar, so that homogeneity is assured.

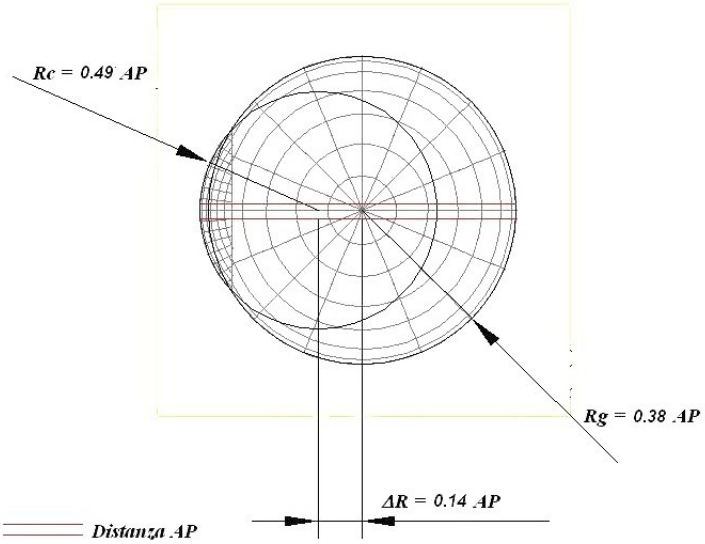

Figure 7.2: Geometrical representation used for the project of the eye phantom, which correspond to the eye modelling in treatment planning. AP = 24.1 mm.

The second type is a PMMA eye phantom realized at INFN-LNS. The eye phantom represent the external part of an eyeball as two intersecting hemispheres

(see figure 7.2). The sphere radii are 11.7 mm and 9.0 mm, respectively, and the shift between their center along the x direction is about 3.4 mm. The half eyeball is located on a PMMA slab 6 cm $\times$ 6 cm $\times$ large, and 2 mm thick. This main slab can be mounted together with a 3 cm thick PMMA block, with the help of four plastic screws, in order to be able to stop protons inside the phantom. Additional slices (either hollowed or not) can be inserted in between so as to place GAF chromic detectors for dosimetric measurements at different depths. Hollowed slices have not been inserted in our measurements, so as to have a uniform PMMA phantom.

7.2 Beam configurations used at the CATANA proton beam line

In all the presented measurements, the transversal beam dimension has not been varied. The reference beam collimator, 25 mm diameter, has been used in all the proton beam irradiations.

In the very first measurements at the CATANA facility on December 2006, the proton irradiations have been used just for detection tests. No dosimetric measurements have been performed, since we were only interested in maintaining constant the irradiation time, the proton current and the acquired statistics. From the available parameters, however, one can estimate that the delivered dose was never either greater than 60 Gy nor lower than 30 Gy. As primary irradiation configuration, unmodulated proton beams have been used with different range shifters. The shifts measured in the induced-activity distal edge were then compared with the nominal thickness of range shifters. A modulated beam configuration with no range shifter has been also used.

In the following two runs of measurement, performed on February and May 2007, it has been chosen to set conditions as close as possible to the clinical ones. Modulated beams have then been preferred, and preliminary dosimetric measurement of each selected dose configuration has been performed for accurate irradiation planning. Figures 7.3 and 7.4 show the depth dose profiles obtained by a scanning with a CCO diode BPW34, for the configurations adopted. Several ranges have been studied with a typical modulation depth (10.8 mm in PMMA), and some analysis on modulation effect has been also performed.

Once one depth-profile has been measured, the center of dose plateau from beam modulation can be found. This is an optimal reference point for an absolute measurement of dose, since fluctuations due to positioning errors are minimized.

range shifter				
element label	mechanical construction		equivalent thickness	
	material	thickness [mm]	PMMA [mm]	eye tissue [mm]
A0	–	0.00	0.0	0.0
1mm	PMMA	1.00	1.0	1.1
A2	aluminum	–	1.9	2.0
A3	PMMA	2.89	2.9	3.0
A4	PMMA	3.85	3.9	4.0
A6	PMMA	5.77	5.8	6.0
modulator wheel				
element label	mechanical construction		equivalent thickness	
	material		PMMA [mm]	eye tissue [mm]
p002	PMMA		10.8	12.0
009/02	PMMA		17.9	20.0

Table 7.1: List of characteristics of range shifters and modulation wheels used during irradiations. Reference abbreviation used in the plots are given.

The absolute measurement is performed with PTW Markus® ionization chamber and is used to determine the conversion factor between dose and monitor units (see section 2.2). When calibration was available, 30 Gy dose has been usually delivered to plastic phantoms.

7.3 Measurements of activation performed with monoenergetic proton beams

Due to the delay in the delivery of the final matrices (see section 4.2), the first measurements planned at the CATANA facility, on December 2006, were performed before a complete detector characterization. No estimation of detector effective area[1], nor lutetium subtraction, nor normalization sensitivity correction

[1]In particular, it was initially believed that the H8500 photocatode area would have allowed the identification of 23 x 23 pixel of 2 mm. After changing the reflecting material and increasing the dead space, a size of 21 x 21 was found to be the optimal. The exceeding pixels were not yet darkened in these first measurements, and their scintillation light affects the precision of the

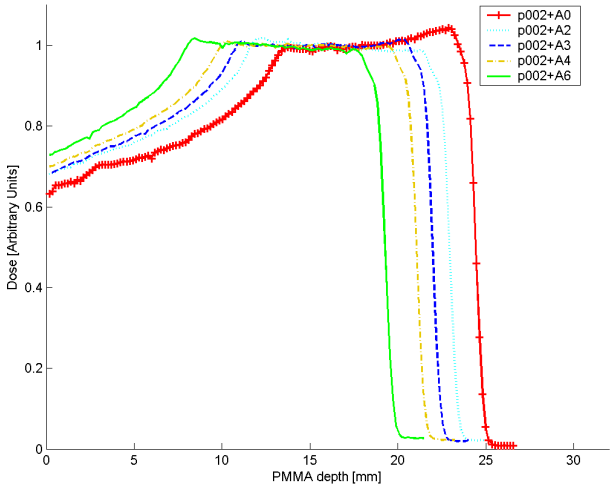

Figure 7.3: In-depth dose profiles of beam line configurations used at CATANA for range shift measurements. Curves are normalized to the middle point of the modulation plateau. Thicknesses in PMMA of range shifters are reported in table 7.1. Eye-tissue equivalent thicknesses are A0=0 mm, A2=2 mm, A3=3 mm, A4=4 mm, A6 = 6mm.

were available. Furthermore, no tests had been possible at high rate, and it was found only too late that the front-end electronics was inadequate to deal with the coincidence rate registered after proton irradiation. The net result is a degradation of planar images which impair pixel resolving. Then event have a high probability to be assigned to the wrong LOR, and energy calibration is neither optimized nor correctly applied.

As additional remark, no reproducibility of phantom positioning was assured in these measurements. In fact, the preliminary version of the phantom holder was designed to assure the vertical and the lateral positioning of the cylinder, but no constraint was set along the beam direction. Moreover, since interest was focussed on the final part of the proton range, the phantom entrance surface where proton were impinging was left outside the FOV.

Due to this situation, no proper planning of measurement has been done, and then those first results are significant only as the very first feasibility demonstration of the prototype, but quantitative analysis are not possible. Data constraints have been somewhat relaxed, by choosing a [100,850] keV window for energy

energy calibration for the visible pixels.

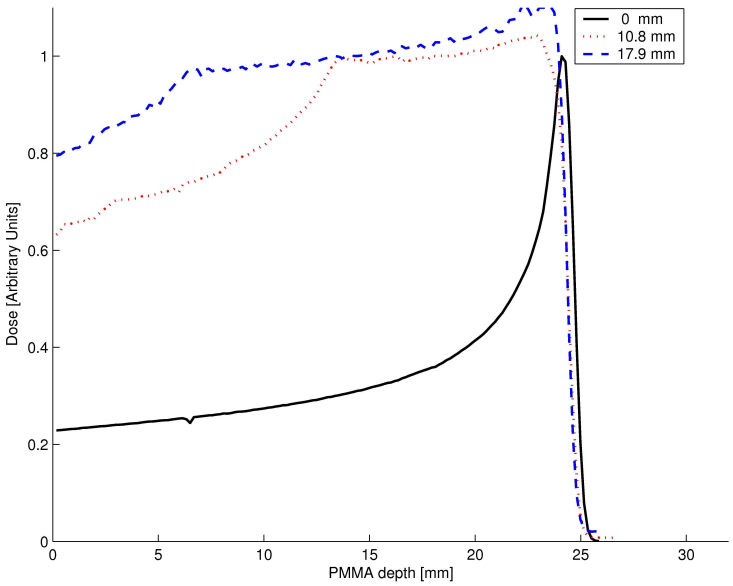

Figure 7.4: In-depth dose profiles of beam line configurations used at CATANA for modulation width detection. Two modulation wheels and a full-energy beam have been used, with no range shifter inserted. The 10.8 mm spread-out curve is the same reported in the previous figure with label A0+p002. Spread-out curves are normalized to the middle point of the modulation plateau, the single Bragg peak is normalized to its maximum. Modulation widths in PMMA are reported in table 7.1. Eye-tissue equivalent modulation widths are: 0 mm, 12 mm, 20 mm.

selection.

As a first check, some measurement has been performed, in order to evaluate the coincidence background which can be produced by the activation of the beam line elements. The detector heads has been placed in position, at 14 cm head-to-head distance, but no phantom has been installed. 30 second irradiations have been performed, and background coincidence rates have been registered during and after irradiation. The evaluation has been performed placing the CFoV at two different distances from the final beam collimator. Results are presented in the table 7.2. As a first comment, concerning the trigger rate registered during the acquisition one must be convinced that no information can be extrapolated with the present detector configuration by acquisitions when the beam is on. In fact, the typical coincidence rate produced by β^+ phantom activation is about 1000 cps, that is much lower than the lowest measured background rate. No energy information for such background events is available for further data analysis.

coll.-CFoV distance [cm]	irradiation bkg raw data [cps]	post-irradiation bkg raw data [cps]	+ ^{176}-Lu subtraction [cps]	+ [100,850] keV selection [cps]
8	9500	117	≈ 60	≈ 10
23	2000	65	≈ 10	≈ 0

Table 7.2: Evaluation of coincidence background produced by beam line activation.

The 8 cm distance correspond to the distance from the final beam collimator to the isocentre, and then would be the ideal placement for the center of the detector FoV. The second distance used has been preferred in this first phase, so as to reduce the background contribution during acquisition. Taking into account the unavoidable lutetium background included in the measurements (see section 6.2), at 23 cm distance the beam activation produces approximately 10 cps rate on the detector. However, it has been verified that energy selection before reconstruction further reduces the collimator activation contribution by a factor larger than 2. Starting from the second measurement run, when a proper energy calibration became available, the distance between collimator and detector has been reduced.

7.3.1 Acquisition at different detector distances

The default beam configuration (no range shifter and no modulation wheel inserted) has been used for the first irradiation tests. An evaluation of detector efficiency scaling for a typical irradiation has been performed. The irradiation depth reached with a full energy beam is about 26.4 mm, which correspond to an irradiated volume of 13 cm^3 when the 25 mm $\oslash$ reference collimator is used. The induced-activity was not entirely contained in the FoV because of a wrong conception of the first version of the phantom holder, and no quantitative evaluation of shifts was possible. Measurements could anyway provide the order of magnitude of acquired statistics, although the collected statistic will be lower than what presented in the following sections, because of the different phantom displacement in the field of view.

Table 7.3 presents the collected statistics in 30 minutes acquisition at various head-to-head distances after 1 minute proton irradiations.

Positioning and irradiation fluctuation should be taken into account. Proton current cannot be precisely controlled, and beam intensity fluctuations of several

head-to-head distance [cm]	initial rate [cps]	acquired statistics
10	$10 \cdot 10^3$	$17.6 \cdot 10^5$
14	$4 \cdot 10^3$	$6.8 \cdot 10^5$
20	$2 \cdot 10^3$	$4.0 \cdot 10^5$
20 *	$2 \cdot 10^3$	$3.8 \cdot 10^5$

* asymmetric detector configuration: (5+15) cm

Table 7.3: Statistics collected after 30 minutes acquisitions at different head-to-head distances.

percent points are possible from one measurement to the following. Furthermore, 1 mm shift in phantom positioning corresponds to about 5% variation in collected statistics.

The only conclusions that can be drawn from this analysis are that coincidences collected during irradiation scale of about a factor 2 when changing the head distance from 20 cm to 14 cm, and that rates registered at 10 cm are even too high for the capability of the acquisition system.

7.3.2 Acquisition after irradiations at different (sharp) Bragg peak depths

A mono-energetic 62 MeV proton beam and three different range shifters were used, thus varyng the irradiation depth from about 26.4 mm to about 21 mm. Irradiations last for about 1.5 minutes, i.e., more protons than before have been used. For the evaluation of detection of shifts in proton range, one of the phantom was left in position for all the measurements in order to assure the same reference system for each dose configuration. A proper time (about one hour) has been waited from one measurement to the following one, in order to assure phantom de-activation.

With an acquisition time of about 10 minutes after the end of each irradiation and a head-to-head distance set to 14 cm, the prototype collected about $3 \cdot 10^5$ coincidences for the measurement corresponding to the smaller irradiation volume. The activity distributions were then reconstructed into a grid of 46×46×46 voxels. The 1 mm-thick central slices in the XZ plane has then been used to evaluate the longitudinal activity profiles, which are reported in figure 7.5. Although the

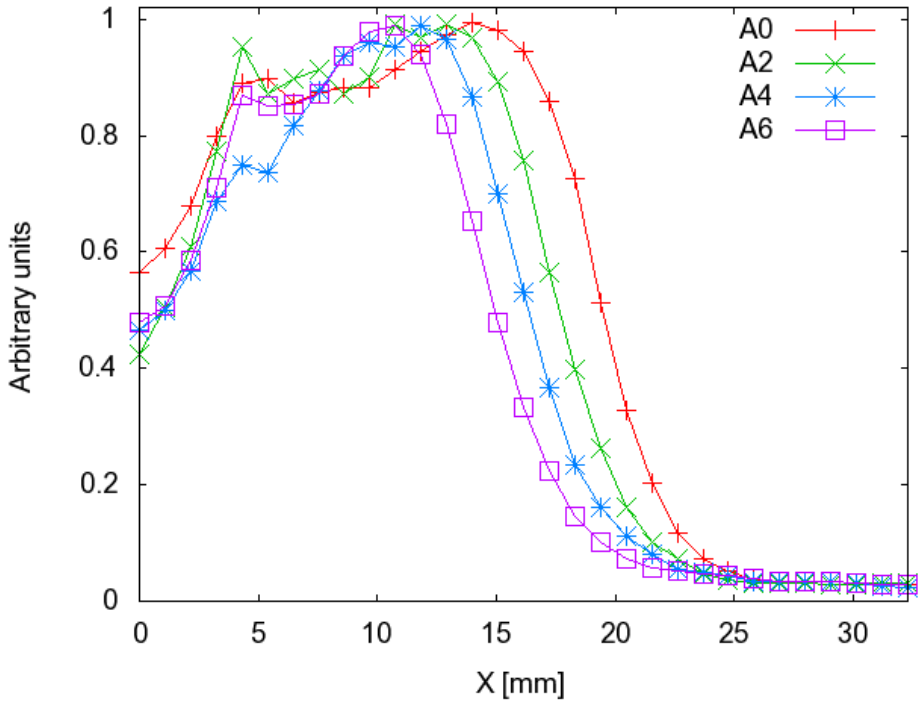

Figure 7.5: Linear profiles in the beam direction obtained by 1.076 mm-thick central slices of the reconstructed images (46x46x46 voxels) for activity acquired after irradiations using the default beam line configuration and three different range shifters (see table 7.1).

central slice activity images are extracted from low statistics 3D images, it was possible to appreciate differences in proton-induced activity distribution along the X direction (i.e., along the proton direction).

A relative measurement was then performed: the distance between any two subsequent distal edges of the reconstructed activity profiles was evaluated and it's reported in table 7.4.

Range shifter difference	[mm]	1.9	1.9	1.9
Distal edge activity distance	[mm]	2.0	1.4	1.4

Table 7.4: Comparison between nominal PMMA thicknesses added from one measurement to the following, and the shift measured in the distal edges of the positron activity.

The measurement results do not perfectly match the corresponding range shifter

thicknesses inserted, however the 2 mm shift in range can be clearly identified.

7.4 Measurements of activation performed with Spread-Out Bragg Peak proton beams

All the irradiations following the test run in December 2006 have been performed after monitor chamber calibration, so as to allow the control of delivered dose. All the acquisitions presented in the following, except where indicated, have been performed after proton irradiations of 30 Gy, i.e., about twice the dose delivered for a real therapy fraction. Beam configurations used correspond to the in-depth configuration shown in figures 7.3 and 7.4 concerning the in-depth distribution, while the transversal distribution is determined by a final collimator of 25 mm diameter. Acquisition time was usually set to 30 minutes and collected statistics was of the order of 10^5 coincidences.

7.4.1 Acquisition after irradiations at different (spread-out) Bragg peak depths

During the characterization of the final matrices, as reported in section 4.2.3, it turned out that only 21×21 crystals per matrix could be detected with good performances. Extra pixels have then been properly darkened, and the number of LORs available for reconstruction dropped from 279841 to 194481. In principle, overall efficiency and spatial resolution are then slightly reduced. However, this is compensated by the increased quality of the remaining data. In fact, since light from outer pixels does not contaminate anymore the signal of edge pixels, the improved pixel identification allows a more accurate energy calibration and a confident assignment of the event to the detecting pixel.

Regarding the large amount of pile-up events registered at the acquisition rate, the cause has been found to be some capacitors introduced to reduce electronic noise in the pre-amplification stage, that increased the time characteristic of the circuit and then the acquisition dead time. The removal of that capacitor solved the rate problem, but has introduced some minor instability in ADC offsets, that have disappeared only in the last version of the electronics boards used for the last run (section 7.4.2).

In figure 7.6 there are presented the in-depth profiles of the measured activity distributions. The shifts in beam range are successfully detected as shift in activity

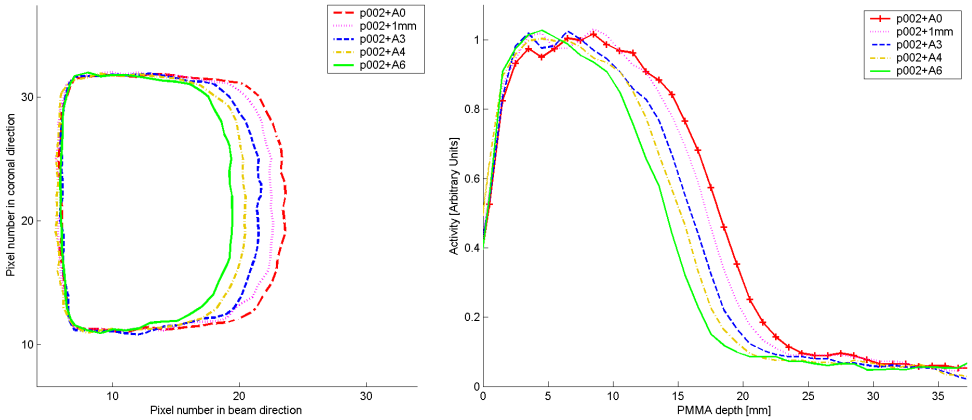

Figure 7.6: 50% contour plot (left) and linear profiles in the beam direction (right) obtained by 1.076 mm-thick central slices of the reconstructed images (42x42x42 voxels) for activity acquired after irradiations using 10.8 mm modulated beams and various range shifters (see dose profiles in figure 7.3).

distribution fall-off. Quantitative analysis of the results will be presented in the next section.

7.4.2 Measurements using the final detector assembly

The high anode luminosity of the PMT used were not compatible with the pre-amplification stage, which was originally developed for SPECT application and using an older version of the PMTs [102]. In order to avoid the ADC saturation we initially operated the photomultipliers at a voltage much lower than the suggested operating one (700 V and 850 V instead of 1000 V).

The final step of detector optimization has been the tuning of front-end electronics amplification. This has allowed to use the PMTs in a more reliable operating condition, obtaining much less instabilities.

The reproducibility of look-up tables each time the detector is assembled has been then assured by gluing the crystal matrices to the PMT photocathodes. Minimal relative shifts were now possible between the crystal grid and the photocathode. This has allowed us to perform the final characterization measurements in Pisa laboratory, and to use the results in the last run in Catania, where the use of liquid sources was not permitted and therefore no sensitivity normalization measurements were possible.

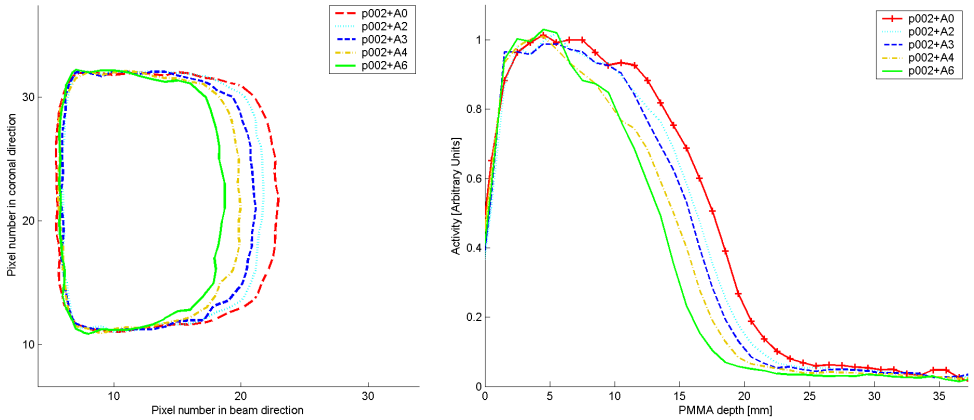

Figure 7.7: 50% contour plot (left) and linear profiles in the beam direction (right) obtained by 1.076 mm-thick central slices of the reconstructed images (42x42x42 voxels) for activity acquired after irradiations using 10.8 mm modulated beams and various range shifters (see dose profiles in figure 7.3).

In figure 7.7 there are presented the in-depth profiles of the measured activity distributions. As already found in the previous measurements, the shifts in beam range up to 1 mm are successfully detected as shift in activity distribution fall-off.

It is interesting to compare results obtained in different runs with the same dose configurations. The minor changes introduced in the acquisition setup has not alterated results and conclusions. The reliability of our results is then well supported by their reproducibility. Measurement reproducibility is fundamental for the quality assurance of clinical treatments, since images produced from different fractions delivered to the same patient in different days will be compared.

From the comparison shown in figure 7.8, one could estimate that the typical deviation that can be expected when reproducing the same activity measurement is of few hundred of microns.

This value has then been used as error bar in the scatter plot in figure 7.9 to verify the sensitivity to range shifts.

Shifts in activity profiles have been measured as shifts in the 50% distal fall-off of the activity profile along the beam direction in the central slice of the reconstructed images. Profiles are evaluated on a single voxel row. Integration on more pixel rows would lead to a reduced statistical fluctuation in the results on beam direction, but would make the results dependent from the coronal profile of the beam. Shifts in proton range have been measured as shifts in practical range mea-

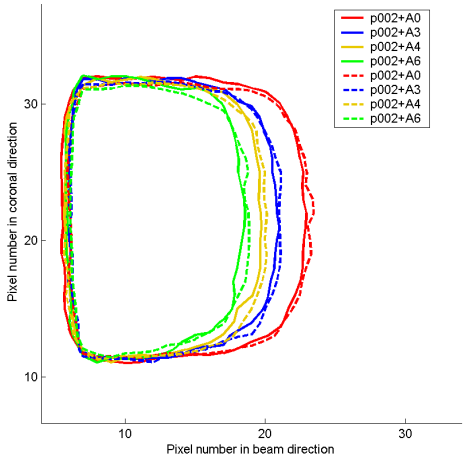

Figure 7.8: 50% contour activity profiles of the central slice (42 x 42 voxel, 1.076 mm thick) of the reconstructed images for the activity acquired after 30 Gy irradiations using 10.8 mm modulation and various range shifters. Solid lines correspond to measurements performed on May 2007, dashed lines correspond to February 2007 measurements. The same color corresponds to the same beam line configuration. The proton beam impinges from left. The proximal edge of the cylindrical phantom is in the vertical line placed at pixel $\#5$ in the beam direction. Center of FoV is at point (21,21) in the shown plot.

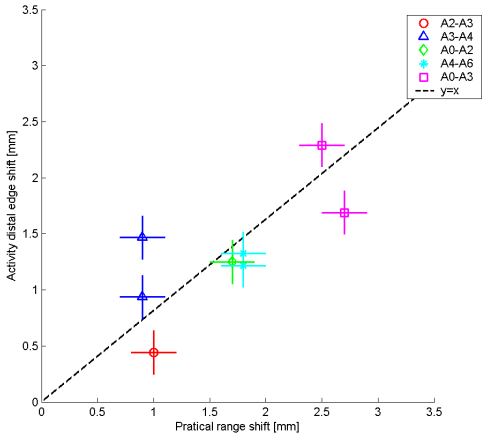

Figure 7.9: Correlation between dose shifts and activity shifts in PMMA phantoms. Legend explains the range shifter combinations used to measure the shifts. As error bars we have indicated the maximum deviation (0.2 mm) in activity shift detection for the repeated measurements. Uncertainties on dose shift measurements are about 0.2 mm. The correlation Y=X is shown by a dotted line.

sured from in-depth dose profiles (see figure 7.3).

If energy dependence of the distal fall-off steepness of the activity profile is neglected, the ideal correlation between dose and activity shifts would lay on the axis bisector y=x. The possibility of neglecting such energy dependence is supported by [81].

An attempt to perform quantitative evaluation of the width of the delivered dose distribution through measurements on induced activity has been also done. In figure 7.10 there are shown the results obtained using different beam modulations, and no range shifter, i.e., dose configuration presented in figure 7.4.

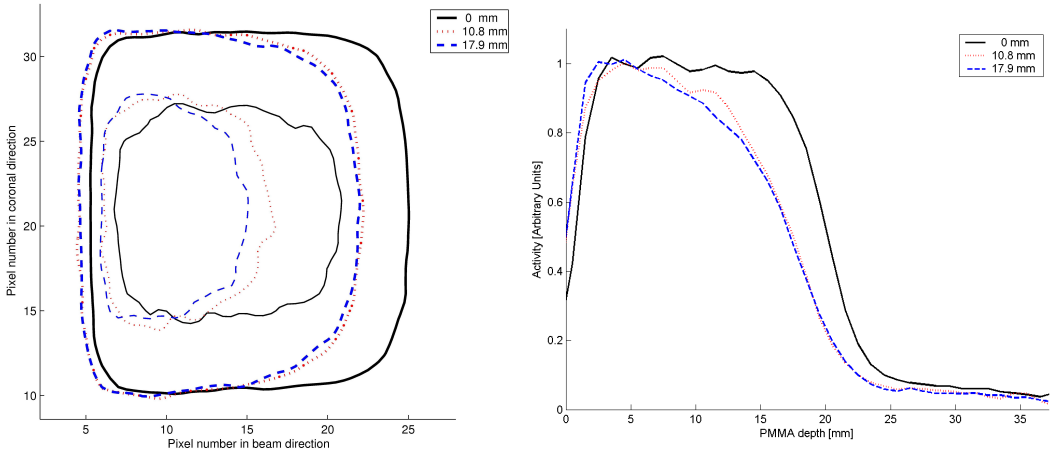

Figure 7.10: 50% and 85% contour plots (left) and linear profiles in the beam direction (right) obtained by 1.076 mm-thick central slices of the reconstructed images (42x42x42 voxels) for activity acquired after irradiations using two energy modulated beams and one unmodulated (see dose profiles in figure 7.4).

The difference in activity profiles between modulated and unmodulated irradiations is well detected, as variation on both in-depth and coronal distributions. The depth-dependence of coronal activity distributions is visible by comparing the 50% contour plots. Since the phantom has the same position in each measurement (i.e., activity profiles start at voxel $\#5$ in the beam direction), it appears from figure 6 that the full-energy beam proximal edge has a milder slope with respect to modulated beams. The detection of differences in the distal slopes of in-depth activity distributions requires a simultaneous observation of 85% and 50% contour plots for each measurement. By decreasing beam modulation, a decreasing of the distance between the two levels of each contour plot happens at distal edge, i.e. a

steepening of the distal edge is detected. Results are consistent with the analytic prediction [81].

7.5 Validation of dose filtering algorithm

A first validation of the filtering algorithm described in section 5.2 has been performed by using experimental data acquired during the final measurement run in May 2007 (see section 7.4.2). A $\tilde{Q}$-functions approximation of the experimental depth dose profiles (figures 7.3 and 7.4) has been computed. Dose profiles have been preliminary smoothed with a Gaussian point spread function of 1.7 mm FWHM to account for the finite spatial resolution of the PET prototype. After that, the linear combination of theoretical ^{11}C and ^{15}O filters has been convoluted with the $\tilde{Q}$-based dose expression to obtain a $\tilde{Q}$-based expression of depth profiles for the induced β^+ activity. All the minor contributions produced by other β^+ emitters have been neglected.

Figure 7.11 shows three examples of the comparison between the measured β^+-activity depth profiles and prediction obtained by dose filtering. A good agreement was found for all beam configurations, i.e., for a large variety of proton energy distributions.

Longitudinal activity profiles in figure 7.11 are obtained by image integration in the transversal direction, in order to have consistency with results of the dose filtering algorithm, where the same integration is assumed. It should be noted that the in-depth activity profiles used for quantitative analysis of range shifts detection (see the previous section) are instead linear profiles obtained from a single voxel column, selected in the transversal direction to correspond to the center of the activity distribution.

Relative contribution of the two activity profiles to the PET image depends on the specific irradiation parameters (beam intensity, irradiation time, proton energy spectrum), that determine the amount of isotope produced and are only approximately known, but mainly from the duration of data acquisition.

A time analysis was performed on acquired data to compare the experimental results with the theoretical prediction of the relative amounts of ^{11}C and ^{15}O detected in a 30 minutes-long acquisition. Image reconstruction has been performed using limited data set, selected in subsequent time intervals. The time evolution of the activity over the acquisition duration has been then fitted by the linear combination of two exponential curves with the proper decay times, for each voxel separately. The linear coefficients produced by the fits have then been used to

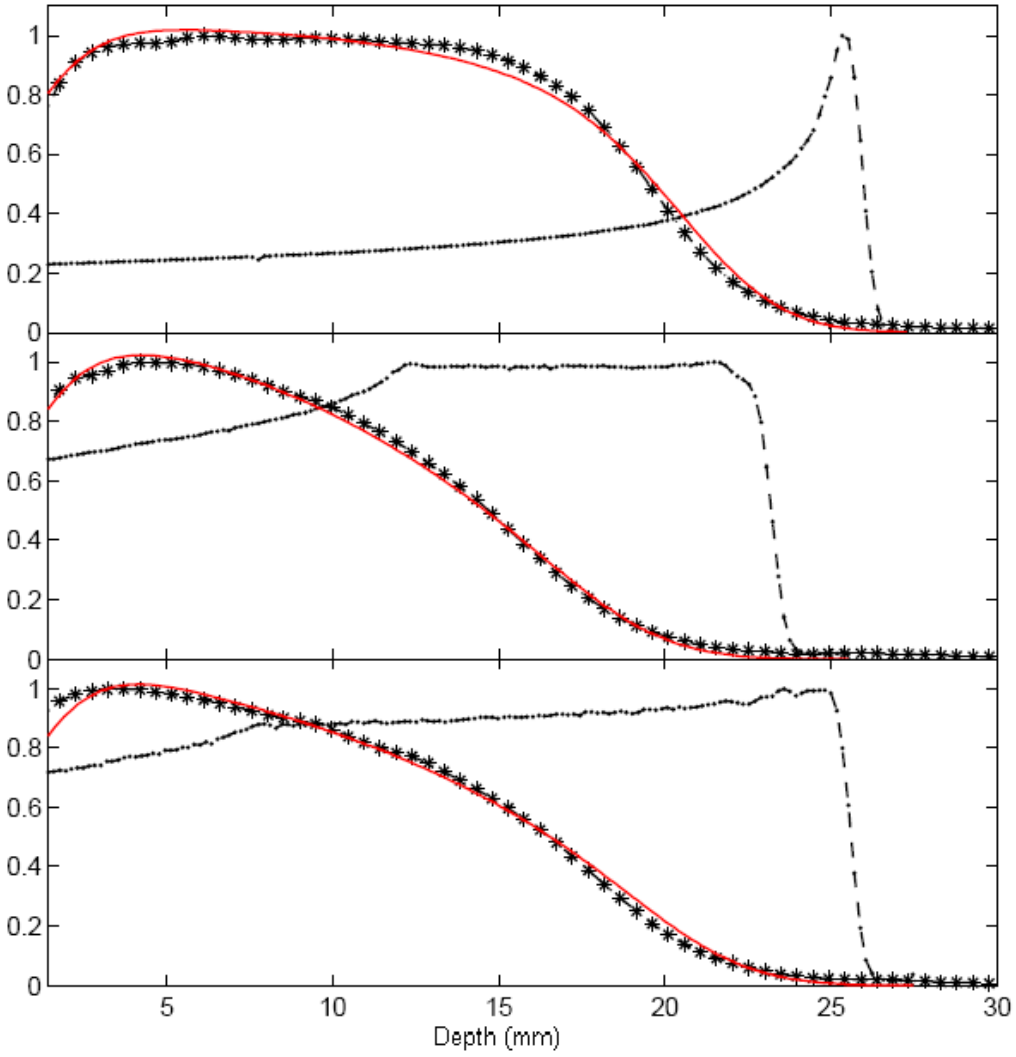

Figure 7.11: Reconstructed activity (star line) compared with the dose (dash-dot line) and the filtered dose (solid red line) for three different proton beam configurations. All the curves are normalized to their maximum. Upper panel: single Bragg peak (default beam configuration, A0). Medium panel: generic shifted and modulated beam (A2 + p002). Lower panel: full-energy modulated beam (A0 + 009/02).

separate the total reconstructed image into the two single-radioisotope activity distribution.

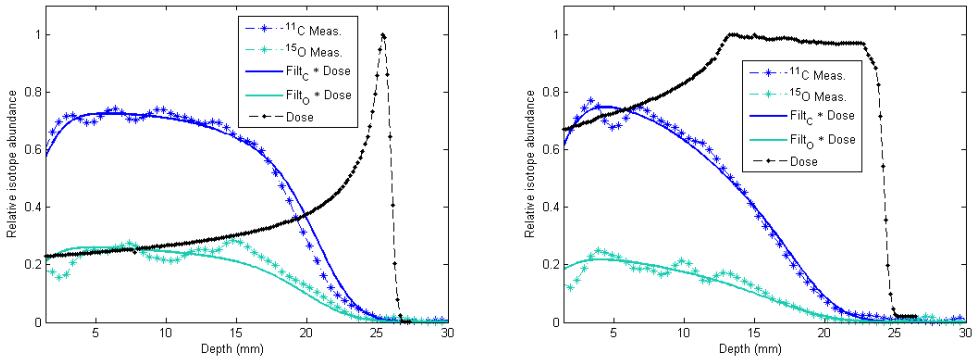

Figure 7.12: Normalized activity distributions for single Bragg peak (A0, left) and spread-out Bragg peak (A2+p002, right) irradiations. Estimated (star line) distributions are compared with the dose (dash-dot line) and the filtered dose (solid line). Carbon (blue) and oxygen (sky-blue) are both shown.

Activity profiles obtained but such single-radioisotope images have then been compared with theoretical prediction from dose filtering. The optimal agreement is shown in figure 7.12. In particular it is confirmed that 75% of measured activity is due to ^{11}C, while about all the remaining contribution is provided by oxygen.

7.6 Qualitative evaluation of a more complex irradiation configuration

All the results presented in the previous section are based on a flat entrance surface, and then on dose and activity distributions almost independent from the radial point within the irradiated transversal section. The approximation of a flat entrace surface, however, cannot be adopted in clinical situations.

In order to perform a more realistic measurement, we have been allowed to use a PMMA eye-phantom developed by the CATANA group, which reproduces a typical eye (see introduction of this chapter). About one therapy dose fraction (15 Gy) has been delivered in about 1 minute as in clinical conditions dose-rates, and an irradiation planning (A2+p002) corresponding to a possible treatment configuration has been applied. In order to get closer to clinical situation, also the

acquisition time has been reduced to 15 minutes.

The result with the eye-shaped phantom is shown in figure 7.13, compared with reconstructed image obtained from 30 Gy proton irradiation of the cylidrical phantom using the same beam configuration.

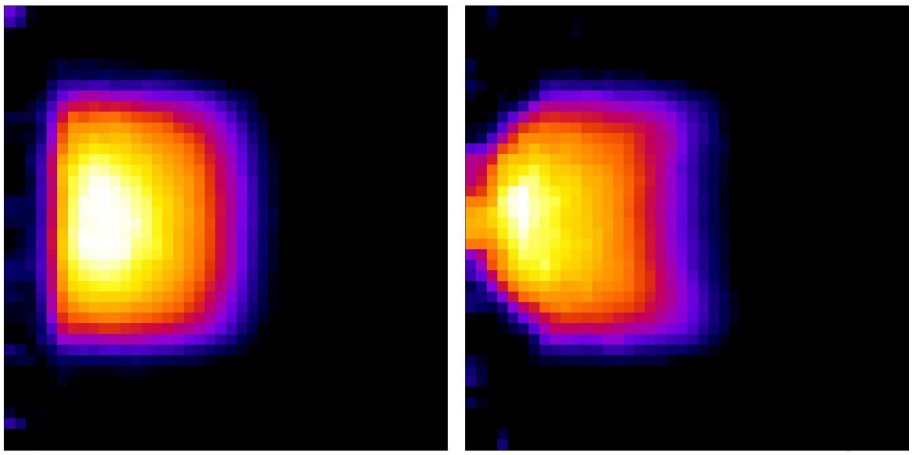

Figure 7.13: Central slice (42x42 voxel, 1.076 mm thick) in the xz plane of the reconstructed image after irradiation of phantoms with different entrance surfaces. Proton impinging from the left. Left: Flat entrance surface. Right: eye-shaped entrance surface. No rigid support was available for the eye-shaped phantom, therefore its displacement in the FoV could not reproduce that of the cylindrical phantom (about 5 mm difference).

The different shape of the entrance surface is rather well detected, and is reproduced in the distal edge of the activity distribution so that the net effect is roughly only a z-dependent activity traslation. Quantitative measurements have not yet been performed, also because the comparison should be repeated at the same irradiation condition (i.e., the same dose should be delivered) and with a better phantom positioning.

In figure 7.14 the previous images are reported as a green contour plot, superimposed on the xy reconstructed central slice.

The cylindrical symmetry of both the irradiation field and the phantoms along the x-axis, produces the same activation in all planes crossing the central x axis. Therefore, in absence of reconstruction artifacts, the color plots should agree with the superimposed color plots. The activity distribution along y appear much larger than the 25 mm expected, because of the effect of the limited solid angle coverage. This makes almost impossible to determine the activity shape from the xy reconstruction, and it is probably affecting the quality of the xz reconstruction.

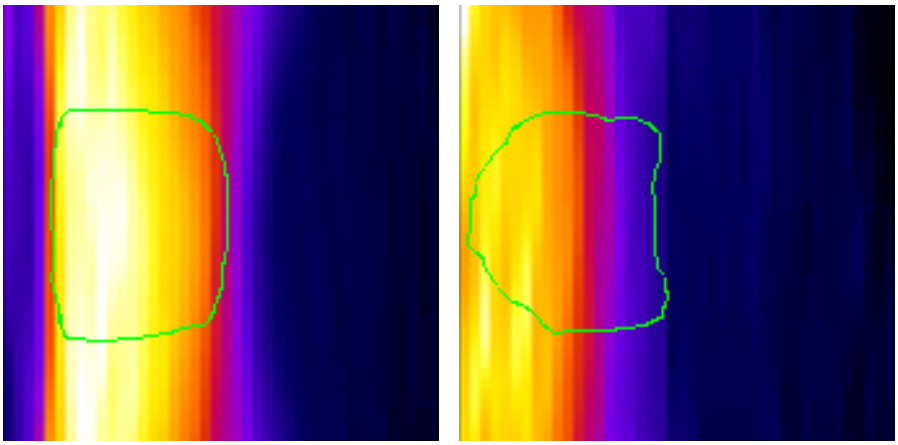

Figure 7.14: Central slice (42x42 voxel, 1.076 mm thick) in the xy plane of the reconstructed image after irradiation of phantoms with different entrance surfaces. The green solid curve superimposed is the 40% contour plot of the central slice in the xz plane. Proton impinging from the left. Left: Flat entrance surface. Right: eye-shaped entrance surface. No rigid support was available for the eye-shaped phantom, therefore its displacement in the FoV could not reproduce that of the cylindrical phantom (about 5 mm difference)

Chapter 8

Summary and Future Work

The "in-beam" PET is one of the most promising techniques for quality assurance in hadrontherapy. Within the DoPET project we started an evaluation of potentiality of dedicated PET scanners for hadrontherapy monitoring. To such aim we have designed a dedicated PET scanner based on a pair of opposing detector heads, made up of a 4.5 cm $\times$ 4.5 cm LYSO scintillator matrix.

The detector performances have been fully simulated, and a semi-analytical method and a GEANT4-based one for beam-induced activity estimation have been developed. At present, the GEANT4 simulation is only used for determining the phase space of the ions impinging on the phantom. While the GEANT4 capability of reproducing all the elements of the CATANA beam line is unchallenged, difficulties have been met on the side of the simulation of isotope production, because of a poor performance of GEANT4 implementation of proton-ion inelastic interactions at MeV energies. Discussion with GEANT4 developers are still ongoing, and studies will start again after the recent advances [103].

The DoPET project had the goal to achieve the detection of 1 mm range differences in proton beam irradiations performed at the CATANA facility on plastic phantoms. Theoretical prediction (section 5.2) demonstrates the feasibility of such purpose.

After detector optimization and calibration, the characterization of planar and 3D performances have been performed.

Flood field images has shown an average peak-to-valley ratio of 7.2, an average intrinsic spatial resolution of about 0.7 mm and an energy resolution lower than 16%. Data contamination from random and ^{176}Lu coincidences, as well as non-uniformities in pixel sensitivity, have been characterized and corrected for in the image reconstruction.

Image reconstruction is performed with a 3D ML-EM iterative algorithm, using a probability matrix based on a multi-ray method. Geometrical symmetries and physical processes which lead to event detection can be modelled. At present only the crystal depth of interaction is implemented, but future improvements are foreseen.

By setting a head-to-head distance of 14 cm, an overall sensitivity of about 1% has been measured, and a spatial resolution lower than 2 mm (FWHM) has been obtained from image reconstruction along beam and vertical directions. The characterization along y is still unsatisfactory, but this was expected form the geometrical design of this first prototype. This aspect has been taken into account in the choice of beam configuration for proton and carbon irradiations.

The validation on plastic phantoms with proton irradiations has been successfully performed at the CATANA beam line, using sharp and spread-out Bragg peaks at different proton ranges.

Reproducibility of results has been verified, thus confirming the reliability of the method for comparing of patient images produced during different therapy fraction for monitoring purposes. Contribution from different positron-emitters have been estimated, confirming that the "in-beam" approach allows one to increase statistics, mainly thanks to the short-lived ^{15}O contribution. Range shifts down to 1 mm have been qualitatively detected. The correlation between dose and activity shifts become poor when shifts are comparable with the voxel size (i.e., 1.076 mm in our reconstruction algorithm). Quantitative detection is possible down to about 2 mm. From detector symmetries, a similar resolution in detecting deviations from planned dose can be also assumed in the vertical direction.

A comparison between the reconstructed image of our standard flat-entrance phantom and a more refined eye-shaped phantom has been also performed, as a first step towards clinical application. In the xz plane, the difference in activity distribution shape at the entrance surface is rather well detected, and as well as its effect at the distal edge of the activity distribution. Dedicated measurements for the quantification of shape detection capability and evaluation of the influence of low performing xy plane have not yet been performed.

The first step to reach a dose-unfolding algorithm has been completed. A convolution filter has been theoretically computed, which allows the analytical estimation of the (transversally integrated) longitudinal activity profile from the measured depth dose profile. Dose filter results have been compared with activity profiles measured after proton beam irradiation on the flat-entrance phantoms. A good agreement is evidenced for both sharp and spread-out Bragg peaks. Work is still ongoing for the extrapolation of the inverse filter which should provide the

dose profile from the measured activity.

A more accurate analysis must be done before concluding the design of a clinical device; in particular, the ability to detect energy modulation should be further explored and different non-uniform phantoms should be used for quantitative analysis in the vertical direction. The positive results already obtained by this first prototype, however, demonstrate the feasibility of a (larger) clinical version of such a dedicated ''in-beam" PET for protontherapy quality assurance.

The validation on plastic phantoms with carbon ion beams has been also started: the preliminary results are reported in appendix B. The detection of shifts in ion range is confirmed, and it is also shown (as expected) a good capability in detection of depth extension of the dose distribution, much better than the one reached with proton irradiations. Further measurements are required to investigate the lower limits of detection capabilities.

Towards a clinical version of DoPET detector

Further funds have been received from MIUR in the framework of PRIN2006 program and from INFN for a second stage of the DoPET project, for realizing a larger version (10×10 cm^2) of the detectors. We have now started the realization of a larger detector, which will be completed in the next year. The $10 \times 10 \times 20$ cm^3 field-of-view (FOV) would produce a significant increase of angular coverage. For typical clinical irradiations of 15 Gy over a 10 cm^3 volume, the statistic collected in ten minutes would then increase to approximately $5 \cdot 10^5$ events, about a factor four with respect to the present detector. Depending on funding [104], the initial design could be further extended to a better geometrical solution, based on two heads (clam shell type) each one 15 cm x 10 cm.

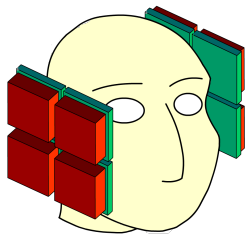

Figure 8.1: Scheme for the second stage of DoPET project.

The evaluation of detector materials has been already concluded, and the LYSO crystal has been confirmed as the scintillator of choice. The crystal pitch is 2 mm and the pixel size is 1.8 mm, slightly smaller than the values used in the present prototype (2.15 mm pitch and 2.0 mm pixel side). Regarding the choice of position sensitive photodetector, the new Burle H85001 PMT has been considered as an alternative to the Hamamatsu H8500 PMT. However, the latter has been confirmed as the

best device for our application, since its low packing density is mandatory for the realization of a modular detector.

The new version of the detector would require much efforts in developing a new readout system. In fact, an independent readout of all the PMTs of one head is required in order to avoid an increase of pile-up and dead time in the acquisition. On the other side, this forces us to develop a system able to handle coincidences between each PMT of one head and any PMT of the opposite head. By combining the information of all the PMTs, some recovery of the dead area at the photomultipliers periphery could also be obtained.

Regarding the reconstruction algorithm, minor changes will be needed for the larger planar version of the detector. All the attention could be then focussed to improve the precision of physics modellization within the probability matrix. For the clam shell heads, the new detector geometry should be also implemented.

The unfolding algorithm would not require substantial modifications (except for the point-spread function and the efficiency adopted), to be adapted to the clinical device for proton therapy monitoring. Present work on 3D dose filtering and on computation of the inverse filter can go on as foreseen by the original project.

The larger device, however, will also sign the evolution from proton eye-therapy monitoring to a more general hadrontherapy monitoring device. Further carbon beam irradiation will be then planned, and a more general algorithm for dose unfolding will need to be developed.

Appendix A

Hadronic physics and implementation in GEANT4

A.1 Hadronic inelastic processes at therapy energies

All the different types of nuclear reactions are summarized schematically in figure A.1.

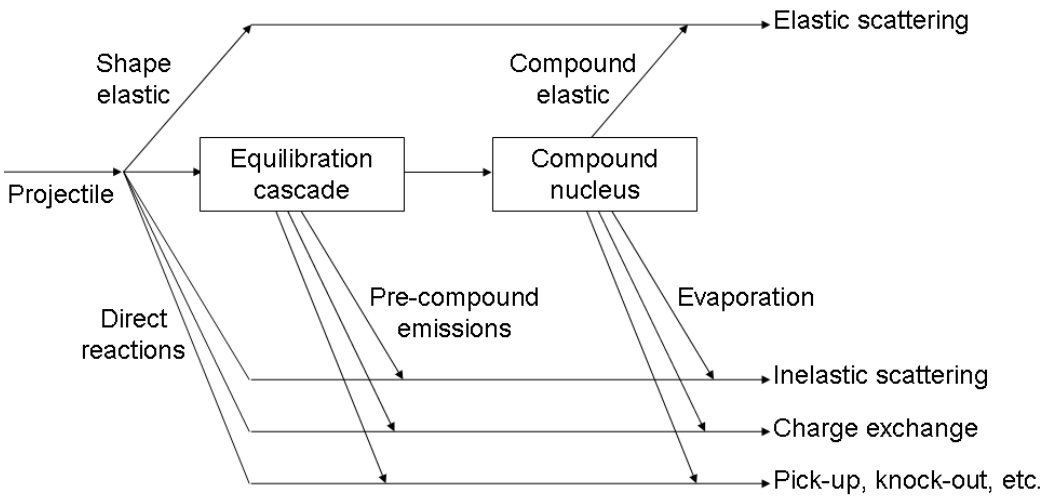

Figure A.1: Direct, pre-compound and compound nucleus contributions to a nuclear reaction. [105]

After the first interaction, the nucleon may leave the nucleus immediately by a direct reaction or it may interact with a nucleon in the nucleus and start a cascade of nucleon-nucleon interactions from which pre-equilibrium emission may occur. During this cascade, the energy is shared among an increasing number of nucleons until the compound nucleus is eventually formed. The compound nucleus may decay into the elastic or any of the reaction channels that are allowed energetically. The shape elastic (scattering by nuclear field) and compound elastic (capture, formation of compound nucleus and emission with the same initial energy) processes combine to give the measured elastic scattering cross section. In a similar way the direct, pre-equilibrium and compound nucleus processes combine to give the inelastic cross sections and all the other non-inelastic reactions.

All these reactions are subject to the conservation laws of energy, momentum, spin, parity, isospin and baryon number, etc., and their relative importance depends on the type of interacting particles and their relative energy.

The *direct reactions* take place in the time the projectile takes to traverse the target nucleus (typically around 10^{-22} s). In these processes the projectile may interact with a nucleon, a group of nucleons or the whole nucleus and emission takes place immediately. In non-inelastic reactions, the states of the residual nuclei which are excited have a simple structural relationship with the ground state of the target nucleus. Inelastic scattering predominantly excites collective states, one-nucleon transfer reactions excite single-particle states, charge-exchange reactions excite particle-hole states and multinucleon transfer excites cluster states.

In *compound nucleus reactions* the projectile is captured by the target nucleus and its energy is shared and re-shared among the nucleons of the compound nucleus until it reaches a state of statistical equilibrium.

The formation of the compound nucleus requires several stages. In the case of a nucleon-induced reaction, it firstly occurs the excitation of a simple state (*doorway state*), as for instance a single-particle state in the potential well. Then, following two-body interactions between the incident nucleon and nucleons of the target nucleus, the excitation of particle-hole states (*hallway states*) of increasing complexity. Finally, as a results of the long sequence of two-body nucleon-nucleon interactions, the long-lived compound nucleus is obtained.

The compound nucleus may decay in a large variety of ways, the main one being *evaporation*. A nucleon or a group of nucleons near the surface may, by a statistical fluctuation, receive enough energy to escape, just as a molecule may

evaporate from a heated drop of liquid. This statistical process favours the evaporation of particles with energy near the smallest possible energy, which in the case of charged particles is the height of the Coulomb potential at the nuclear surface, the Coulomb barrier. This gives an observable Maxwellian distribution in the spectrum of the ejectiles. If the excitation energy of the compound nucleus is high enough, several particles may be evaporated in sequence and the process continues until the energy of the nucleus is below the threshold for particle emission, and then the nucleus emits γ-rays until it reaches the ground state. An alternative important decay channel for heavy compound nuclei is fission into two fragments of comparable mass.

The lifetime τ of the compound nucleus is connected by the uncertainty principle to the width of the specific resonance state (energy, spin and parity) in which it is produced. Compound nucleus reactions therefore take place in a time which depends on the projectile energy, but that is always several[1] orders of magnitude greater than the one required for direct reactions, due to the time required for compound formation and to its long lifetime.

It can happen that a particle is emitted neither immediately after the interaction of the projectile with a nucleon or with a group of nucleons of the target nucleus, as in a direct reaction, nor after a long time by the statistical decay of the compound nucleus. The projectile may share its energy among a small number of nucleons which may further interact with other nucleons, and during this cascade of nucleon-nucleon interactions through which the energy of the incident particle is progressively shared among the target nucleons, a particle may be emitted long before the attainment of statistical equilibrium. These processes constitute the third reaction mechanism and are the *pre-compound* or *pre-equilibrium reactions*.

Nuclear reactions involving two heavy ions makes possible new reaction mechanisms due to the complex ion structure. Such reactions are not of interest in this work, since mainly proton induced reactions are considered.

[1] $10^6 - 10^7$ times greater at low incident energies and only about $10 - 100$ times greater at high incident energies.

A.2 Hadronic Inelastic Physics List in GEANT4.8

Binary Cascade Model Binary Cascade is an intra-nuclear cascade propagating primary nucleons and all secondary particles within a nucleus. Interactions take place between a primary or secondary particle and an individual nucleon of the nucleus. The nucleus is modelled by explicitly positioning nucleons in space, and assigning momenta to these nucleons. This is done in a way consistent with the nuclear density distributions, Pauli's exclusion principle, and the total nuclear mass. Free hadron-hadron elastic and reaction cross-section are used to define collision locations within the nuclear frame. Where available, experimental cross-sections are used directly or as a basis for parameterizations used in the model. Propagation of particles in the nuclear field is done by numerically solving the equations of motion, using time-independent fields derived from optical potentials. The cascade begins with a projectile and the nuclear description, and terminates when the average energy of all participants within the nuclear boundaries are below a given threshold. The remaining pre-fragment are treated by pre-equilibrium decay.

Precompound The GEANT4 precompound model is considered as a low energy extension of the hadron kinetic model. It provides a "smooth" transition from kinetic stage of reaction described by the hadron kinetic model to the equilibrium stage of reaction described by the equilibrium deexcitation models.

At the preequilibrium stage of reaction, decay involves both the emission of particles and the evolution of the number of excitons [2]. Transitions in exciton number of$n$ with $\Delta n = +2, -2, 0$ and emission of neutrons, protons, deutrons, tritium and helium nuclei are considered. The precompound stage of nuclear reaction is effective until nuclear system is not an equilibrium state. Further emission of nuclear fragments or photons from excited nucleus is simulated using an equilibrium model.

De-Excitation Models: evaporation, multifragmentation and Fermi breakup. At the end of a thermalizing process, or the pre-equilibrium stage, the residual nucleus is supposed to be left in an equilibrium state, in which the excitation energy E^* is shared by a large number of nucleons. Such a compound nucleus

[2]The number of excitons is defined as the sum of the number of particles and holes in a nucleus. The excitons energies are calculated in the kinetic model from the Fermi energy T_F. All cascade nucleons with kinetic energies above T_F and absorbed by a nucleus are called particles. The holes are results of cascade interactions, when particles stroke nucleons from nucleus and they occupy states below T_F. [106]

in equilibrium is characterized by its mass, charge and excitation energy with no further memory of the steps which led to its formation. If the excitation energy is higher than the separation energy, it can still eject nucleons and light fragments (^{2}H, ^{3}H, ^{3}He, α) with branching ratios given by the available phase space. These constitute the low energy and most abundant part of the emitted particles in the rest system of the residual nucleus. The emission of particles by an excited compound nucleus has been successfully described by comparing the nucleus with the evaporation of molecules from a fluid.

The first statistical theory of compound nuclear decay is due to Weisskopf and Ewing (1940) and this is the default evaporation model in GEANT4 at excitation energies below 3 MeV per nucleon.

The Statistical Multi-fragmentation Model (SMM) by Bondorf et al (1995) was used at excitation energies above 3 MeV per nucleon to describe multifragment break-up of highly excited residual nuclei. The SMM includes as its part the Fermi break-up model describing an explosive disintegration of excited light nuclei.

The Fermi break-up model is capable to predict final states as result of a statistical break-up of an excited nucleus with atomic number $A < 17$.

Appendix B

Measurements with carbon ions at GSI syncrotron

In perspective of a future application of the clinical version of DoPET detector, considering the increasing interest for carbon therapy, the validation of DoPET detector as device for carbon therapy monitoring becomes as important as its role in proton therapy. Carbon ions can be produced at the LNS cyclotron with energies of about 62 AMeV, and only passive beam shaping is available. Much higher energies and active beam shaping are generally adopted for therapy, then we needed the help of a different beam facility.

A heavy ion tumor therapy pilot project is running at the Gesellschaft für Schwerionenforschung (GSI, Darmstadt) to exploit the physical and radiobiological advantages of carbon ions for high precision radiotherapy. Since December 1997, more than 300 patients with radioresistant tumors in the head and neck region as well as in the pelvis were treated with high energy ^{12}C ions yielding very promising clinical results [107, 108]. The GSI project is the first European operating center for cancer therapy with carbon beams, and it was the only one until 2008[1]. As additional appeal, at GSI is installed the first clinical operating in-beam PET (see chapter 1).

On July 2007, we asked and obtained to perform one run of measurements after carbon ions irradiation, using the GSI synchrotron in Darmstadt. The syn-

[1] A dedicated hospital-based ion beam facility for cancer therapy has now been completed in Heidelberg, Germany. This facility, expected to be operational in the next months, will have a treatment throughput of 1000 patients per year with a wider spectrum of treatable tumors. It will, furthermore, provide beams ranging from proton to oxygen ions thus enabling further clinical studies to be performed.

chrotron ion beam energy used for hadrontherapy ranges from about 88AMeV to about 440 AMeV[2], and the 3D-dose configuration can be obtained by the 2D-raster scanning and the active energy modulation. Dose delivery is planned on the basis of analytic computation, using the code TRiP98 [109].

Although the GSI syncrotron allows a very flexible control of irradiation configuration through beam energy variation and 2D magnetic scanning, we were limited in our choice by the very small dimensions of the DoPET FoV.

In order to compare carbon and proton results, we selected the beam configuration so that irradiate volumes were similar to those used at CATANA. Since dose planning of simple geometries in TRiP98 is easier for squared (and spherical) rather than cylindrical treatment volumes, we decided to adopt a squared section of 28mm side. Three monoenergetic configurations and two extended configurations have been used for carbon irradiations.

Beam parameters and resulting characteristics are listed in table B.1, while the computed dose profiles are shown in figure B.1. About 0.5 mm accuracy is achieved for the treatment planning.

Monoenergetic beams			Extended beams		
Range [mm]	Energy [AMeV]	Intensity [ions]	SOBP width [mm]	Min. energy [AMeV]	Intensity [ions]
21.9	108.53	$3.38 \cdot 10^9$	-	116.57	$3.46 \cdot 10^9$
23.6	112.60	$3.42 \cdot 10^9$	3.4	108.53	$5.26 \cdot 10^9$
25.3	116.57	$3.46 \cdot 10^9$	6.8	100.07	$6.44 \cdot 10^9$

Table B.1: Beam parameters of monoenergetic and extended configuration for carbon irradiations. Range values and SOBP width are expressed in PMMA. Intensity values are given for 60 Gy dose delivery. The maximum beam energy for the extended configuration is always 116.57 AMeV, therefore the third row of left table and the first of right table are the same irradiation.

The total delivered dose was 60 Gy for each beam configuration, divided as 6 beam repainting of 10 Gy each, in order to reduce effects due to phantom deactivation during the irradiation and to enhance homogeneity in the detected activity distribution. The total time required for irradiation spanned from 2 to 6 minutes, mainly because of spill pauses and repainting.

[2]Ions in the GSI synctrotron can be accelerated up to about 2 AGeV, but such a high energy is not used in clinical application.

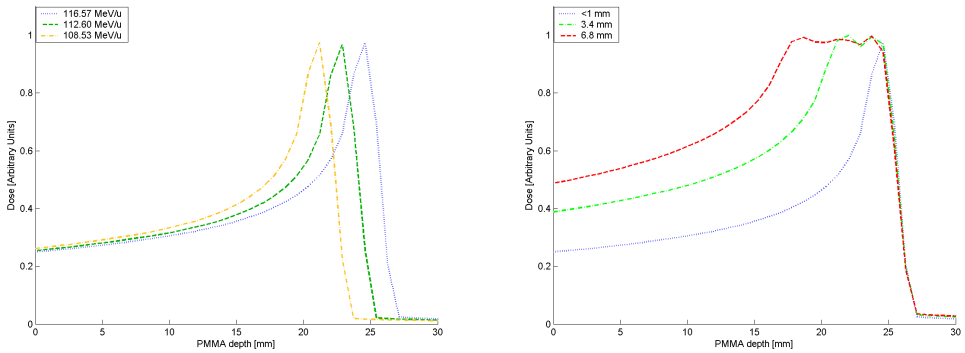

Figure B.1: Calculated in-depth dose profiles for the beam configurations used at GSI for range shift (left) and spread-out width (right) measurements. Blue curve represent the same dose configuration in both plots. Energy parameters used for the simulation are shown in table B.1.

Acquired configuration cannot be compared neither with any GSI clinical situation nor with proton beam configurations used above. In fact, carbon therapy is usually adopted for deep-seated tumours (i.e., very different beam ranges) and only 1 Gy is delivered to the tumoural tissues. Underfractionated effective dose (15 GyE) for ocular protontherapy at CATANA would have been eventually reproduced by a 8 Gy carbon delivery, since the RBE of carbon ions is about 1.7 times higher than the one of protons [11]. The dose fraction used for multi-portal ocular carbon therapy performed at HIMAC [12] is slightly less, between 4 and 6 Gy. For the first tests, however, we have chosen a much higher dose in order to be sure that the reconstructed images were not impaired by the poor statistics. Better tuning of irradiation parameters will be performed next time.

The acquisition were started together with the irradiation, and lasted 35 minutes each. Off-line comparison has been performed between the entire data set and rejection of data belonging to the first minutes, and results are shown in figure B.2.

No significant difference in the energy spectrum is detected when rejecting data acquired in the first six minutes. In addition, no differences between the data distributions have been evidenced in the planograms when applying time selection. Since one fifth of the overall statistics is acquired during that time, no data rejection would be preferred. However, only post-irradiation data are used for the analysis presented below, since an anomalous behaviour of the acquisition system during irradiations made us suspect a rate saturation in that time interval.

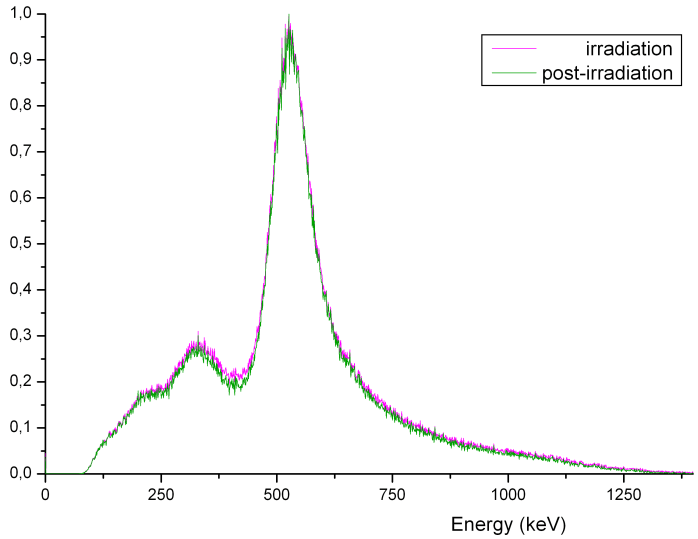

Figure B.2: Spectra obtained from data acquired during carbon irradiation (red) and after carbon irradiation (green). Curves are normalized to their maximum.

In the future, the implementation of a beam triggering is foreseen, so as to be able to acquire ”in-beam” at least during the spill pauses when background rate is lower.

Statistics collected after this selection, however, is about 10^5 events per acquisition, i.e., the same order of magnitude than the one collected after 30 Gy proton irradiations (although differently distributed in the activated volume).

Results of phantom activation after monoenergetic carbon irradiations are shown in figure B.3. The detected shifts in the 50% distal fall-off are 1.8 mm and 3.7 mm. As a rule of thumb, the 1.7 mm range shift between dose peaks should be detected as $1.7 \cdot \frac{11}{12}$ mm = 1.6 mm between activity peaks, because of the different range of ^{12}C and ^{11}C.

Results with extended carbon irradiations are presented in figure B.4. As expected, carbon-induced activity distributions allow an optimal detection for both the proximal and distal edges of dose distribution. A proper analysis of these carbon irradiations requires then the definition of a quantity which can characterize the detection of the Bragg peak spread-out. For the dose measurements the 90% distribution width is given. We decided to adopt the 50% width of the in-depth activity distribution. The FWHM of the activity distribution induced by the monoenergetic peaks is about 5.3 mm. The detected 50% activity distribution widths for the 3.4 mm and 6.8 mm spread-out Bragg peaks are 7.5 mm and 9.7 mm,

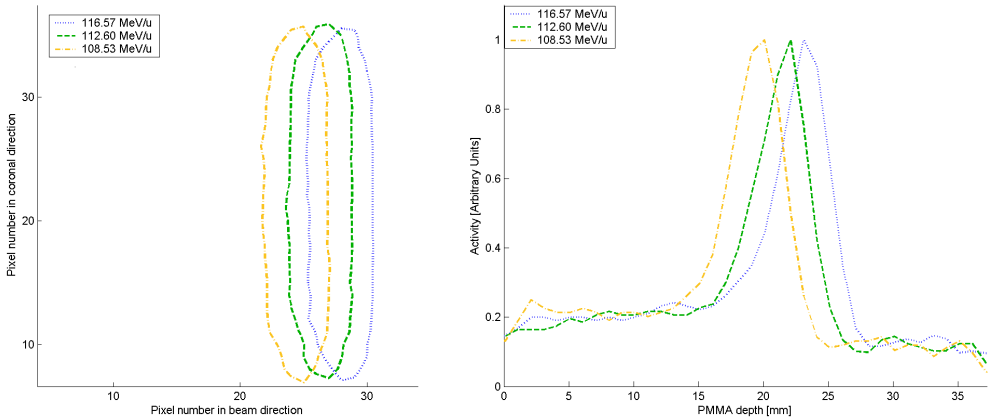

Figure B.3: 50% contour plot (left) and linear profile (right) obtained by 1.076 mm-thick central slices of the reconstructed images (42x42x42 voxels) for activity acquired after irradiations using three different monoenergetic carbon beams.

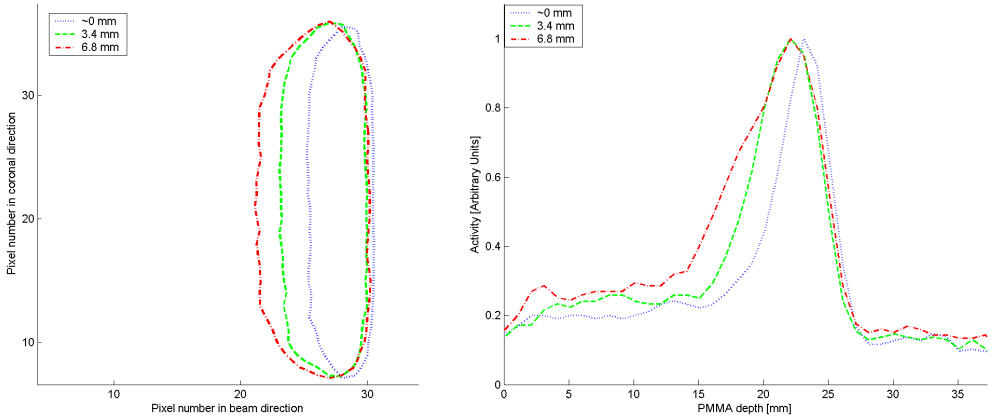

Figure B.4: 50% contour plot (left) and linear profile (right) obtained by 1.076 mm-thick central slices of the reconstructed images (42x42x42 voxels) for activity acquired after irradiations using three different energy modulation for carbon beam irradiations.

respectively.

One of the extended irradiations (3.4 mm SOBP) corresponds to a superposition of the three measured monoenergetic peaks only, therefore a reproducibility check has been performed by using linearity of the transfer function from dose to activity profiles. The coefficients for linear combination of the three peaks have

been extrapolated as the ratio of ions delivered in the monoenergetic configuration and ions delivered in the extended configuration for each energy step. The linear combination of the three monoenergetic-induced activity profiles well matches the extended-induced activity distribution, as shown in figure B.5.

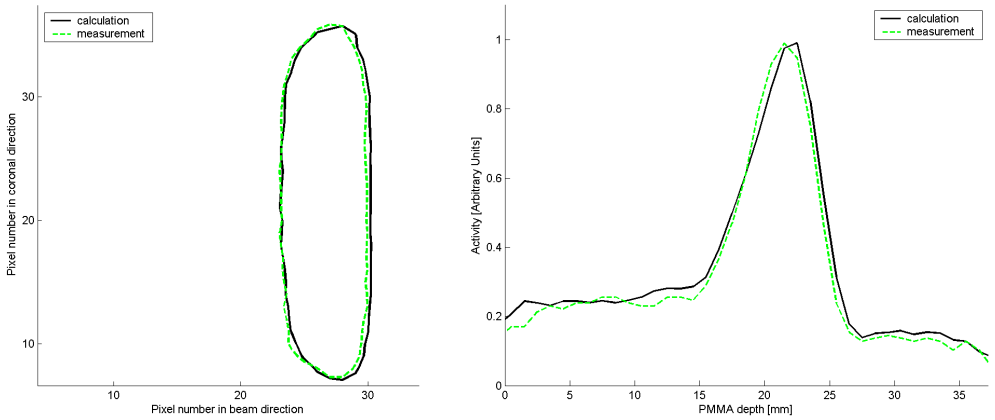

Figure B.5: 50% contour plot (left) and linear profile (right) obtained by 1.076 mm-thick central slices of the reconstructed images (42x42x42 voxels) are compared for a consistency check. The dashed green line are data acquired after 60 Gy carbon irradiation using 3.4 mm spread-out Bragg peak. Solid black line correspond to the weighted sum of data individually acquired for the three monoenergetic peaks (figure B.3) that are used to produce the same spread out irradiation at GSI syncrotron.

Correlation between dose and activity measurements are presented in figure B.6. The ideal line $y = \frac{11}{12}x$ is consistent with data obtained from range shifts, but statistics is not enough for conclusive statements. The correlation between the quantity defined (peak FWHM) for the characterization of the activity measurement and the quantity used for dose measurements (90% peak width) is not easily predictable. The same linear correlation $y = \frac{11}{12}x$ (plus an offset) has been considered as a possibility.

A rigorous analysis of the results could be performed when more data will be available and when a filtering algorithm (see section 5.2) for carbon irradiations will be completed.

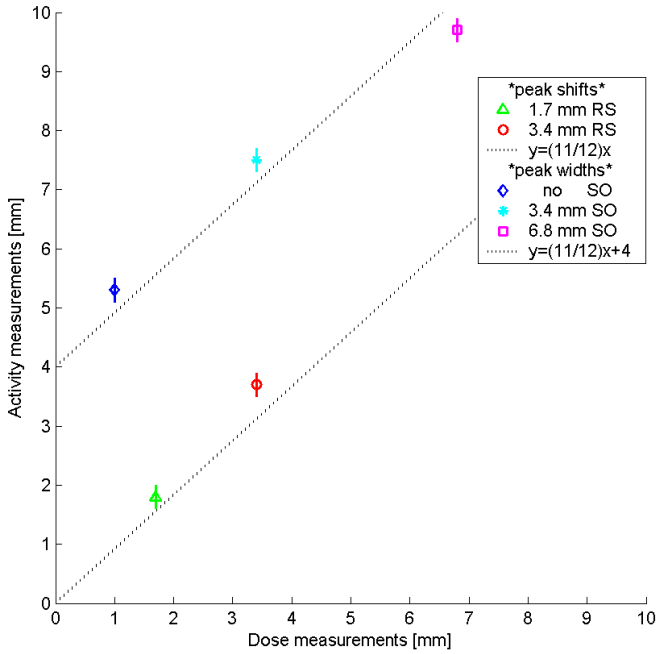

Figure B.6: Correlation between dose shifts and activity shifts, as well as Bragg peak spread-out and activity distribution spread-out in PMMA phantoms for carbon irradiations. Legend explains the quantity measured and the irradiation type used to measure it. The ideal correlation Y=$\frac{11}{12}$X is shown by a dotted line.

B.1 Comparison with BASTEI scanner performances

The positron emission tomograph BASTEI (Beta Activity Measurements at the Therapy with Energetic Ions [27, 110]) installed at the GSI tumour therapy unit consists of two detector heads with 42 $\times$ 21 cm^2 front area each. Each head, forming a spherical calotte with radius 41.5 cm, was built from block detectors of the ECAT® EXACT$^{\mathrm{TM}}$ tomograph from CTI PET Systems Inc. In these detectors, a block of the inorganic scintillator BGO is coupled to PMTs. A block is subdivided into 8 $\times$ 8 BGO crystals with 6.75 $\times$ 6.75 mm^2 front surface each and 20 mm depth, read with a modified Anger scheme by four PMT. A total of 8 $\times$ 4 block detectors were implemented in each head. This detector arrangement consists of 2048 pixel elements per head which yield about $4.2 \cdot 10^6$ lines-of-response (LOR's) crossing the field of view (FoV) of the tomograph.

The total detection efficiency at the centre of the positron camera is approximately 2.3% in the energy window [250,850] keV. The energy resolution is about

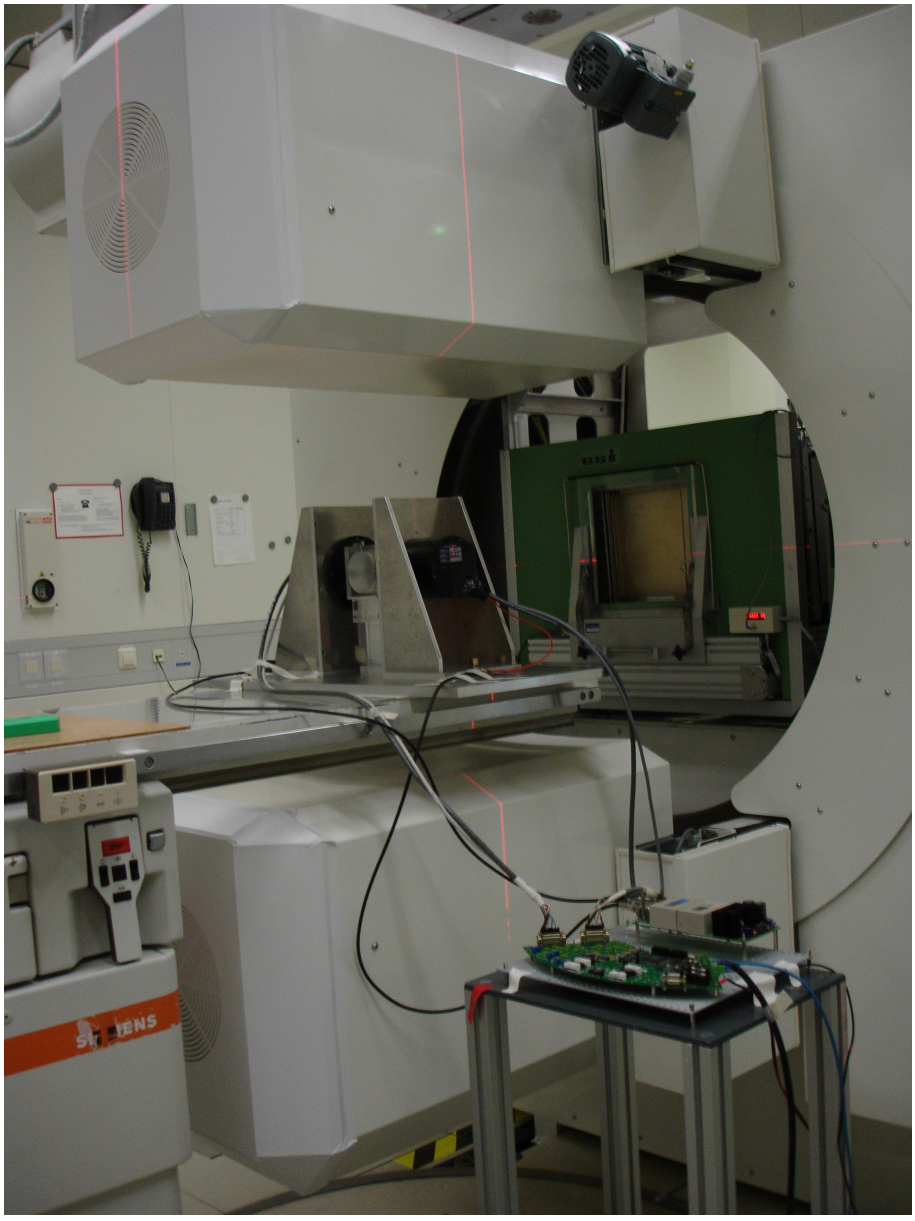

Figure B.7: Experimental configuration for scanner comparison. The BASTEI detector heads are the big white blocks displayed in vertical. The DoPET detector heads are the small black cylinder in the middle, close to the plastic phantom.

16% at 511 keV, the spatial resolution varies between 5 and 7 mm (FWHM). Synchronization of in-beam PET data with the time structure of the slow particle extraction delivered by the synchrotron is derived from the output of an ionization chamber which the beam passes before reaching the target. Data acquisition can then be started with the irradiation, so as to profit of the spill pauses for increasing statistics when γ-ray background produced by beam induced nuclear reactions is absent [101].

A dedicated, attenuation correcting, maximum likelihood expectation maximization algorithm with a single Compton scatter correction is available for image reconstruction of patient data. However, filtered backprojection is adopted for data analysis in phantom experiments.The reconstructed image have a voxel size of 4.81 mm^3 and a total number of 216000 voxels which are reconstructed from 4194304 LOR's.

A comparison of BASTEI and DoPET performance has been performed, on the basis of carbon irradiations presented in the previous section. The two PET devices were placed around the irradiated phantom as shown in figure B.7. Once detectors have been aligned for carbon beam delivery, a ^{22}Na point-source has been placed in front of the phantom entrance surface, and acquired with the BASTEI scanner in order to assure the same system reference. All the carbon induced activity distributions presented in the previous section, was simultaneously acquired by both PET detectors. Linear activity profiles obtained from BASTEI data are shown in figures B.8 and B.9.

A higher photon attenuation affects data acquisition for the lower BASTEI head, because of the presence in the FoV of the anticorodal mechanical supports used for the plastic phantom and for the DoPET heads. Before starting a quantitative analysis of the profiles, this effect should be modellized in the probability matrix used for image reconstruction.

However, these preliminary results are enough to state that 2 mm range shifts and 4 mm peak broadening are detected also with BASTEI in-beam PET. Moreover, one can notice that the shape of the activity distribution is significantly different from DoPET results. This is due to the broader detector point-spread-function, as well as to the possibility to acquire β^+ decays during carbon irradiation, in the spill pause. The latter hypothesis is supported by previous works of the GSI group [37]. The DoPET detector is forced to reject all the data before the irradiation end, while BASTEI can perform a real "in-beam" acquisition, and is then able detect a spatial pattern of activation deriving from both ^{11}C and the shorter-lived ^{15}O decays.

The acquired data can be used also to observe the relation between the detector

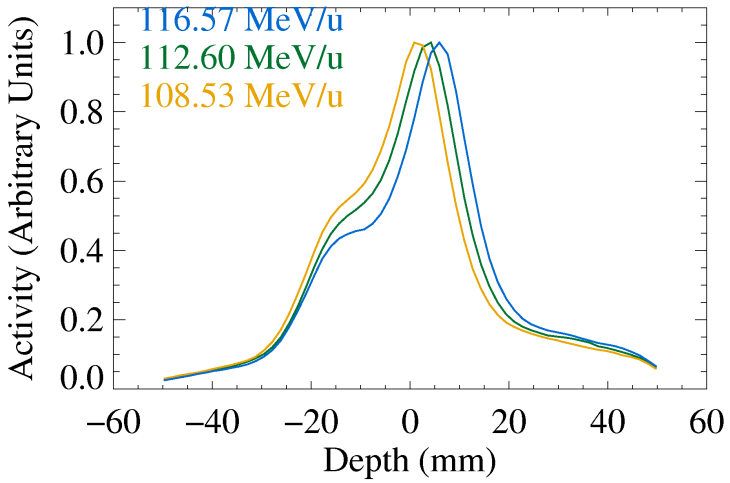

Figure B.8: Linear profiles in the beam direction obtained by central slices of the reconstructed images for activity acquired with BASTEI detector after monoenergetic irradiations (see dose profiles in figure B.1). 0 mm depth correspond to the CFoV of the tomograph. Phantom entrance surface is placed about 20 mm back.

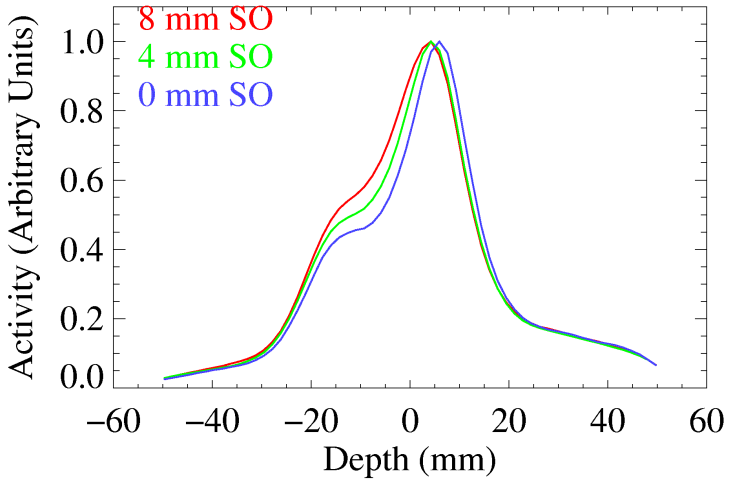

Figure B.9: Linear profiles in the beam direction obtained by central slices of the reconstructed images for activity acquired with BASTEI detector after energy-modulated irradiations (see dose profiles in figure B.1). 0 mm depth correspond to the CFoV of the tomograph. Phantom entrance surface is placed about 20 mm back.

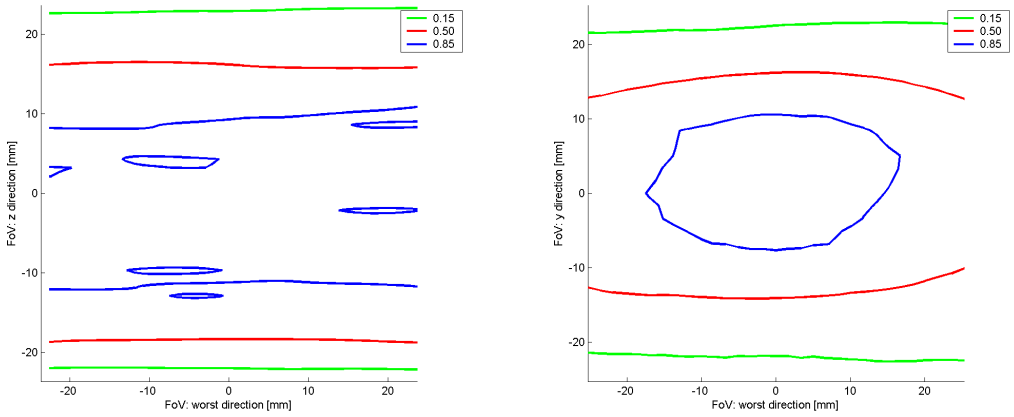

Figure B.10: 15%, 50% and 85% contour plots obtained by central slices in the yz plane of the reconstructed images for activity acquired with DoPET (left) and BASTEI (right) detector after 112.60 MeV irradiation. Point (0,0) correspond to the CFoV of the tomograph. The real edges of the beam field are placed at $\pm$14 mm along both directions.

partial angular coverage and the elongation in reconstructed images (see section 6.4). In figure B.10, there are shown contour plots from activity reconstructed in the plane orthogonal to the beam direction (yz plane). Since DoPET detectors are orthogonal to y-axis, and BASTEI heads to z-axis, the image distortion produced by the "gaps" in the virtual detector rings does not affect the same axis of the reconstructed volume for both scanners. However, thanks to the symmetry under 90^o rotation of the squared irradiation field, a comparison of the zy-images produced by the two positron cameras is possible. From the picture one can observe that the 28 mm squared transversal section is unrecognizable along y in image reconstructed from the DoPET data, while it is much less distorted along z in the image obtained from the BASTEI acquisition.

B.2 Preliminary conclusions

The detection of shifts in ion range by DoPET prototype is confirmed, and it is also shown (as expected) its good capability in detection of depth extension of the dose distribution, much better than the one reached by the same prototype with proton irradiations (see section 7.4.2).

By a preliminary comparison DoPET performance are similar to those of BASTEI detector in terms of ion range resolvability, but somewhat worse in terms

of activity quantification, since the delayed acquisition start prevents the acquisition of large part of the ^{15}O activity. On the other side, DoPET exhibits a superior spatial resolution due to the smaller crystal and detector size and this allows a better resolvability of depth extension of the Bragg peak.

Further measurements are required to investigate the lower limits of detection capabilities, and some more improvement to the detector and to the analysis software could be added. The main improvement required before a new set of measurements is the beam triggering: the possibility to accomodate external trigger signal to tag the acquired data for real in-beam operation would allow to increase the statistics including the β^+ decays occurring during the spill pauses.

Appendix C

List of acronyms

BASTEI	Beta Activity Measurements at the Therapy with Energetic Ions
BGO	$Bi_4Ge_3O_{12}$, bismuth germanate
CATANA	Centro di AdroTerapia e Applicazioni Nucleari Avanzate, Catania, Italy
CFD	Constant Fraction Discriminator
CRT	Conformal RadioTherapy
CT	Computed Tomography
CFoV	Center of FoV
DoPET	Dosimetry with PET
DPC	Discretized Positioning Circuit
EFoV	Edge of FoV (at the phantom edge position)
EM	Expectation Maximization
FoV	Field of View
FWHM	Full Width Half Maximum
GSI	Gesellschaft für Schwerionenforschung, Darmstadt, Germany
HIMAC	Heavy Ion Medical Accelerator in Chiba, Chiba, Japan
HIT	Heidelberg IonTherapy centre, Heidelberg, Germany
IMRT	Intensity Modulated RadioTherapy
INFN	Istituto Nazionale di Fisica Nucleare, Italy
LET	Linear Energy Transfer
LOF	Line Of Flight
LOR	Line Of Response
LYSO	$Lu_{2(1-x)}Y_{2x}SiO_5$ ($x \approx 0.1$), lutetium-yttrium oxyorthosilicate
LUT	Look Up Table
MA	Multi-Anode

MC	Monte Carlo
ML	Maximum Likelihood
NPTC	Northeastern Proton Treatment Center, Boston, USA
OS-EM	Ordinary Subset EM
PET	Positron Emission Tomography
PMMA	PolyMethyl-MethAcrylate
PMT	PhotoMultiplier Tube
PSPMT	Position-Sensitive PMT
RBE	Relative Biological Effect
SCD	Symmetric Charge Division
SOBP	Spread Out Bragg Peak
SPECT	Single Photon Emission Computed Tomography
YAP	$YAlO_3$, yttrium-aluminum perovskite

Bibliography

[1] Ferlay J *et al.* (2007), Estimates of the cancer incidence and mortality in Europe in 2006, Annals of Oncology 18 (3) 581

[2] Proposal for a dedicated ion beam facility for cancer therapy. GSI Nachrichten 1999 (1) 14 [J. Debus ed., Report of the DKFZ, GSI et FZR, September 1998].

[3] Bennett G W *et al.* (1978), Visualization and transport of positron emission from proton activation in vivo, Science 200 1151

[4] Oelfke U *et al.* (1996), Proton dose monitoring with PET: quantitative studies in Lucite, Phys. Med. Biol. 41 (1) 177

[5] Litzenberg D W *et al.* (1999), On-line monitoring of radiotherapy beams: experimental results with proton beams, Med. Phys. 26 (6) 992

[6] Parodi K *et al.* (2002), In-beam PET measurements of β^+ radioactivity induced by proton beams, Phys. Med. Biol. 47 (1) 21

[7] Parodi K *et al.* (2005), Experimental study on the feasibility of in-beam PET for accurate monitoring of proton therapy, IEEE Trans. Nucl. Sci. 52 (3) 778

[8] Nishio T, Sato T, Kitamura H, Murakami K and Ogino T (2005), Distributions of β^+ decayed nuclei generated in the CH_2 and H_2O targets by target nuclear fragment reaction using therapeutic MONO and SOBP proton beam, Med. Phys. 32 (4) 1070

[9] Hishikawa Y *et al.* (2002), Usefulness of positron-emission tomographic images after proton therapy, Int. J. Radiat. Oncol. Biol. Phys. 53 (5) 1388

[10] Cuttone G *et al.* (1996), CATANA: The INFN-LNS facility for the uveal melanoma treatment, Proc. Soc. Ital. Ricerca sulle Radiazioni, Palermo

[11] Tsuji H *et al.* (2007), Carbon-ion radiotherapy for locally advanced or unfavorably located choroidal melanoma: a Phase I/II dose-escalation study, Int. J. Radiat. Oncol. Biol. Phys. 67 (3) 857

[12] Koyama-Ito H, Kanai T, Minohara S, Tsuji H and Tsujii H (2007), Carbon ion therapy for ocular melanoma: planning orthogonal two-port treatment, Phys. Med. Biol. 52 (17) 5341

[13] ICRU Report 60 (1998), Fundamental Quantities and Units for Ionizing Radiations

[14] Brahme A (2000), Development of radiation therapy optimization, Acta Oncol. 39 (5) 579

[15] Webb S (2001), Intensity-Modulated Radiation Therapy, Institute of Physics Publishing, Bristol

[16] Pedroni E (2000), Will we need proton therapy in the future?, Europhysics News 31 (6)

[17] Weyrather W K, Debus J (2003), Particle beams for cancer therapy, Clinical Oncology 15 (1) S23

[18] Haettner E, Iwase H and Schardt D (2006), Experimental fragmentation studies with ^{12}C therapy beams, Radiation Protection Dosimetry 122 (1-4) 485

[19] Kempe J, Gudowska I and Brahme A (2007), Depth absorbed dose and LET distributions of therapeutic ^{1}H, ^{4}He, ^{7}Li and ^{12}C beams, Med. Phys. 34 (1) 183

[20] Antonuk L E (2002), Electronic portal imaging devices: a review and historical perspective of contemporary technologies and research, Phys. Med. Biol. 47 (6) R31.

[21] Steward V W and Koehler A M (1973), Proton radiography as a diagnostic tool, Phys. Med. Biol. 18 (4) 591

[22] Cormack A M and Koehler A M (1976), Quantitative Proton Tomography: Preliminary Experiments, Phys. Med. Biol. 21 (4) 560

[23] Colombino P, Fiscella B and Trossi L (1965), Study of positronium in water and ice from 22 to -144 °C by annihilation quanta measurements, Il Nuovo Cimento XXXVIII (2) 707

[24] Llacer J (1988) Positron emission medical measurements with accelerated radioactive ion beams, Nucl. Sci. Appl. 3 (2) 111

[25] Urakabe E, Kanai T, Kanazawa M *et al.* (2001), Spot Scanning Using Radioactive ^{11}C Beams for Heavy-Ion Radiotherapy, Jpn. J. Appl. Phys. 40 (Part 1, N. 4A) 2540

[26] Kanazawa M *et al.* (2002), Application of an RI-beam for cancer therapy: in vivo verification of the ion-beam range by means of positron imaging, Nucl. Phys. A 701 (1-4) 244c

[27] Enghardt W *et al.* (2004), Charged hadron tumour therapy monitoring by means of PET, Nucl. Instr. Meth. A 525 (1-2) 284

[28] Fiedler F, Crespo P, Sellesk M, Parodi K and Enghardt W (2006) The feasibility of in-beam PET for therapeutic beams of ^{3}He, IEEE Trans. Nucl. Sci. 53 (4) 2252

[29] Inaniwa T, Kohno T, Tomitani T, Sato S (2008), Monitoring the irradiation field of ^{12}C and ^{16}O SOBP beams using positron emitters produced through projectile fragmentation reactions, Phys. Med. Biol. 53 (3) 529

[30] Moeckel D *et al.* (2007), Quantification of β^{+} activity generated by hard photons by means of PET, Phys. Med. Biol. 52 (9) 2515

[31] Mueller H *et al.*(2006), In-beam PET at high-energy photon beams: a feasibility study, Phys. Med. Biol. 51 (7) 1779

[32] Mizuno M, Tomitani T, Kanazawa M, *et al.* (2003), Washout measurement of radioisotope implanted by radioactive beams in the rabbit, Phys. Med. Biol. 48 (15) 2269

[33] Inaniwa T *et al.* (2005), Simulation for position determination of distal and proximal edges for SOBP irradiation in hadron therapy by using the maximum likelihood estimation method, Phys. Med. Biol. 50 (24) 5829

[34] http://www.fzd.de/db/Cms?pOid=24771&pNid=427

[35] Enghardt W *et al.* (1999), Positron emission tomography for quality assurance of cancer therapy with light ion beams, Nucl. Phys. A 654 (Issue 1, Suppl. 1) 1047c

[36] Enghardt W *et al.* (2004), Dose quantification from in-beam positron emission tomography, Radiother. Oncol. 73 (Suppl. 2) S96

[37] Pönisch F *et al.* (2004), The modelling of positron emitter production and PET imaging during carbon ion therapy, Phys. Med. Biol. 49 (23) 5217

[38] Hishikawa Y *et al.* (2002), Usefulness of positron-emission tomographic images after proton therapy, Int. J. Radiation Oncology Biol. Phys. 53 (5) 1388

[39] Parodi K and Bortfeld T (2006), A filtering approach based on Gaussian-powerlaw convolutions for local PET verification of proton radiotherapy, Phys. Med. Biol. 51 (8) 1991

[40] Mizuno H *et al.* (2003), Washout measurement of radioisotope implanted by radioactive beams in the rabbit, Phys. Med. Biol. 48 (15) 2269

[41] Iseki Y *et al.* (2003), Positron camera for range verification of heavy-ion radiotherapy, Nucl. Instr. Methods A 515 (3) 840

[42] Nishio *et al.* (2006), Dose-volume delivery guided proton therapy using beam on-line PET system, Med. Phys. 33 (11) 4190

[43] Attanasi F *et al.* (2008), Preliminary results of an in-beam PET prototype for proton therapy, Nucl. Instr. and Meth. A 591 (1) 296

[44] Taverne M *et al.* (2007), Detector characterization for an inline PET scanner in hadrontherapy, Nucl. Instr. and Meth. A 571 (1-2) 396

[45] Inaniwa T *et al.* (2005), Quantitative comparison of suitability of various beams for range monitoring with induced β^+ activity in hadron therapy, Phys. Med. Biol. 50 (6) 1131

[46] Hamamatsu Technical Information, H8500 PSPMT, Japan, 2003.

[47] Del Guerra A *et al.* (2006), Performance Evaluation of the Fully Engineered YAP-(S)PET Scanner for Small Animal Imaging, IEEE Trans. Nucl. Sci. 53 (3) 1078

[48] Gragoudas E S (1989), Current treatment of metastatic choroidal tumors, Oncology (Huntingt) 3 103

[49] Letson A D, Davidorf F H, Bruce R A Jr (1982), Chemiotherapy treatment of choroidal metastases from breast carcinoma, Am. J. Ophtalmol. 93 (1) 102

[50] Damato B, Ocular tumors: Diagnosis and treatment. Oxford: Butterworth Heinemann, 2000. p. 57-93.

[51] Brady L W, Shields J A, Augsburger J J and Day J L (1982), Malignant intraocular tumors, Cancer 49 (3) 578.

[52] Dobrowsky W (1988), Treatment of choroidal metastases. Br. J. Radiol. 61 (722) 140.

[53] Fuss M, Loredo L N, Blacharski P A, Grove R I, Slater J D (2001), Int. J. Radiation Oncology Biol. Phys. 49 (4) 1053

[54] Courdi A *et al.* (1999), Results of proton therapy of uveal melanomas treated in Nice, Int. J. Radiation Oncology Biol. Phys. 45 (1) 5

[55] Tsina E K, Lane A M, Zacks D N, Munzenrder J E, Collier J M and Gragoudas E S. (2005), Treatment of metastatic tumors of the choroid with proton beam irradiation, Ophthalmology 112 (2) 337

[56] Char D H *et al.* (1993), Helium ions versus ^{125}I brachytherapy in the management of uveal melanoma: A prospective, radomized, dynamically balanced trial, Ophtalmology 100 (10) 1547.

[57] http://ptcog.web.psi.ch/ptcentres.html

[58] Finger P T (1997), Radiation therapy for choroidal melanoma, Surv. Ophthalmol. 42 (3) 215

[59] Wilson M W (1999), Comparison of episcleral plaque and proton beam radiation therapy for the treatment of choroidal melanoma, Ophthalmology 106 (8) 1579

[60] Damato B, Kacperek A, Chopra M, Campbell I R and Errington R D (2005), Proton beam radiotherapy of choroidal melanoma: the Liverpool-Clatterbridge experience, Int. J. Radiation Oncology Biol. Phys. 62 (5) 1405

[61] Spatola C *et al.* (2003), Clinical application of proton beams in the treatment of uveal melanoma: the first therapies carried out in Italy and preliminary results (CATANA project), Tumori 89 (5) 502

[62] Cirrone G A P *et al.* (2004), A 62-MeV Proton beam for the treatment of ocular melanoma at Laboratori Nazionali del Sud-INFN, IEEE Trans. Nucl. Sci. 51 (3) 860

[63] Dendale R *et al.* (2006), Proton beam radiotherapy for uveal melanoma: Results of Curie Institut-Orsay Proton Therapy Center (ICPO), Int. J. Radiation Oncology Biol. Phys. 65 (3) 780

[64] Cirrone G A P *et al.*, The CATANA proton therapy facility: four years of clinical and dosimetric experience, LNS Activity Report 2006, 185

[65] Egger E, Schalenbourg A, Zografos L, Bercher L, Boehringer T, Chamot L and Goitein G (2001), Maximizing local tumor control and survival after proton beam radiotherapy of uveal melanoma, Int. J. Radiation Oncology Biol. Phys. 51 (1) 138

[66] Attanasi F (2006), Dosimetria PET in vivo nella terapia a protoni, Università di Pisa, Tesi di Laurea Specialistica, Anno Accademico 2005-2006

[67] http://depts.washington.edu/simset/html/simset_main.html

[68] Cirrone G A P *et al.* (2006), The GEANT4 toolkit capability in the hadron therapy field: simulation of a transport beam line, Nucl. Phys. B (Proc. Suppl. 150) 54

[69] Agostinelli S *et al.* (GEANT4 Collaboration) (2003), GEANT4-a simulation toolkit, Nucl. Instr. and Meth. A 506 (3) 250

[70] Allison J *et al.* (GEANT4 Collaboration) (2006), GEANT4 developments and applications, IEEE Trans. Nucl. Sci. 53 (1) 270

[71] Geant4 collaboration, Physics Reference Manual v 8.0, December 2005

[72] http://root.cern.ch

[73] Ferrari A *et al.*, FLUKA: A multi-particle transport code, CERN Yellow Report No. INFN/TC_05/11

[74] Folger G *et al.* (2004), The Binary Cascade: nucleon nuclear reactions, Eur. Phys. J. A 21 (3) 407

[75] Fermi E (1950), High Energy Nuclear Events, Prog. Theor. Phys. 5 (4) 570

[76] Del Guerra A *et al.* (1995), A compilation of nuclear nonelasticity data for PET-monitored hadrontherapy, TERA 95/19 TRA 15

[77] J. Beebe-Wang *et al.* (2003), Simulation of Proton Therapy Treatment Verification via PET Imaging of Induced Positron-Emitters, NSS Conf. Rec., 2003 IEEE (4) 2496

[78] Vavilov P V (1957), Interaction cross section of π mesons and nucleons at high energies, Zh. Eksp. Teor. Fiz. 32 940 [Sov. Phys. JETP 5 749]

[79] Parodi K and Enghardt W (2000), Potential application of PET in quality assurance of proton therapy, Phys. Med. Biol. 45 (11) N151

[80] Pshenichnov I *et al.* (2006), Distributions of positron-emitting nuclei in proton and carbon-ion therapy studied with GEANT4, Phys. Med. Biol. 51 (23) 6099

[81] Attanasi F *et al.* (2008), Experimental validation of the filtering approach for dose monitoring in proton therapy at low energy, Physica Medica XXIV (2) 102

[82] Sekiya H *et al.* (2006), Studies of the performance of different front-end systems for flat-panel multi-anode PMTs with CsI(Tl) scintillator arrays, Nucl. Instr. and Meth. A 563 (1) 49

[83] Vecchio S *et al.*, Preliminary study of different readout strategies for a positron emission mammograph head, Nucl. Instr. and Meth. A 569 (2) 264

[84] Belcari N *et al.*, Performance of a four-output front-end electronics for multi-anode PMTs readout of scintillator arrays, Nucl. Instr. and Meth. A 572 (1) 335

[85] Pani R *et al.* (2004), Imaging detector designs based on flat panel PMT, Nucl. Instr. and Meth. A 527 (1-2) 54

[86] Siegel S *et al.* (1996), Simple charge division readouts for imaging scintillator arrays using a multi-channel PMT, IEEE Trans. Nucl. Sci. 43 (3) 1634

[87] Olcott P D *et al.* (2005), Compact readout electronics for position sensitive photomultiplier tubes, IEEE Trans. Nucl. Sci. 52 (1) 21

[88] Pani R *et al.* (2003), Flat Panel PMT for photon emission imaging, Nucl. Instr. and Meth. A 505 (1-2) 590

[89] Popov V *et al.* (2001), Analog readout system with charge division type output, NSS Conf. Rec., 2001 IEEE (4) 1937

[90] Herbert D *et al.* (2004), A comparison of the imaging performance of different PSPMTs for PET applications, Nucl. Instr. and Meth. A 518 (1-2) 399

[91] Philips Product Specification, XP2020 PMT, France, 2005.

[92] Firestone R B and Shirley V S, editor (1996). Table of Isotopes. John Wiley & Sons, Inc., New York, 8th edition

[93] Enghardt W, Fromm W D, Manfrass P and Schardt D (1992), Limited-angle 3D reconstruction of PET images for dose localization in light ion tumour therapy, Phys. Med. Biol. 37 (3) 791

[94] Yoshizawa Y and Takeuchi J (1997), The latest vacuum photodetector, Nucl. Instr. and Meth. A 387 (1-2) 33

[95] Motta A *et al.* (2005), Fast, 3D-like Expectation Maximization Reconstruction using Planograms for the Stationary Planar Positron Emission Mammography camera, Computerized Medical Imaging and Graphics 29 (8) 587

[96] Moehrs S, Defrise M, Belcari N, Del Guerra A (2007), Multi-Ray based system matrix generation for 3D PET reconstruction, Proc. of The 9th International Meeting on Fully Three-Dimensional Image Reconstruction in Radiology and Nuclear Medicine, Lindau, Germany. 217

[97] Hebert T, Leahy R M (1990), Fast method for including attenuation in the EM algorithm, IEEE Trans. Nucl. Sc. 37 (2) 754

[98] Yavuz M, Fessler J A (1996), Objective functions for tomographic reconstruction from randoms-precorrected PET scans, NSS Conf. Rec., 1996 IEEE (2) 1067

[99] Kadrmas D J (2004), LOR-OSEM: statistical PET reconstruction from raw line-of-response histograms, Phys. Med. Biol. 49 (20) 4731

[100] Bortfeld T (1997) An analytical approximation of the Bragg curve for therapeutic proton beams, Med. Phys. 24 (12) 2024

[101] Parodi K *et al.* (2005), Random coincidences during in-beam PET measurements at microbunched therapeutic ion beams, Nucl. Instr. Meth. A 545 (1-2) 446

[102] Camarda M *et al.* (2007), SPEMT imaging with a dedicated VAoR dual-head camera: preliminary results, submitted to Nucl. Instr. and Meth. A

[103] Pshenichnov I *et al.* (2007), PET monitoring of cancer therapy with ^{3}He and ^{12}C beams: a study with the GEANT4 toolkit, Phys. Med. Biol. 52 (24) 7295

[104] Battistoni G *et al.* (2008), The INFN TPS project, to appear on Nuovo Cimento C

[105] Hodgson P E, Gladioli E, Gladioli Erba E, Introductory Nuclear Physics, Clarendon Press, Oxford, 1997

[106] Gudima K K, Mashnik S G, Toneev V D (1983), Cascade-exciton model of nuclear reactions, Nucl. Phys. A 401 (2) 329

[107] Schulz-Ertner D *et al.* (2002), Radiotherapy for chordomas and low-grade chondrosarcomas of the skull base with carbon ions, Int. J. Radiat. Oncol. Biol. Phys. 53 (1) 36

[108] Krämer M *et al.* (2004), Treatment planning for scanned ion beams, Radiother. Oncol. 73 (Suppl. 2) 80

[109] Krämer M *et al.* (2000), Treatment planning for heavy ion radiotherapy: Physical beam model and dose optimization, Phys. Med. Biol. 45 (11) 3299

[110] Crespo P A V, Shakirin G, Enghardt W (2006), On the detector arrangement for in-beam PET for hadron therapy monitoring, Phys. Med. Biol. 51 (9) 2143

Publications

2006-1 VECCHIO S, Camarda M, Belcari N, Bianchi D, Cinti M N, Del Guerra A, Herbert D, Lazzarotti M and Pani R (2006), Preliminary study of different readout strategies for a positron emission mammograph head, Nucl. Instr. and Meth. A 569 (2) 264-8

2006-2 Lanconelli N, Campanini R, Iampieri E, Pani R, Cinti M N, Bennati P, Belcari N, Camarda M, Spontoni L, VECCHIO S, Randaccio P, Russo P and Del Guerra A (2006), Optimization of the acquisition parameters for a SPET system dedicated to breast imaging, Conference Records of 2006 IEEE NSS/MIC/RTSD , San Diego, USA, M14-18, 2959-62

2007-1 Belcari N, Del Guerra A, Camarda M, Spontoni L, VECCHIO S and Bianchi D (2007), Performance of a four-output front-end electronics for multi-anode PMTs readout of scintillator arrays, Nucl. Instr. and Meth. A 572 (1) 335-7

2007-2 VECCHIO S, Belcari N, Bennati P, Camarda M, Campanini R, Cinti M N, Del Guerra A, Iampieri E, Lanconelli N, Pani R and Spontoni L (2007), A Single Photon Emission Computer Tomograph for breast cancer imaging, Nucl. Instr. and Meth. A 581 (1-2) 84-7

2007-3 Attanasi F, Belcari N, Camarda M, Cirrone G A P, Cuttone G, Del Guerra A, Di Rosa F, Lanconelli N, Moehrs S, Rosso V, Russo G and VECCHIO S, Test Results from an "in-beam" PET system, LNS Activity Report 2006, 193-195

2008-1 Belcari N, Del Guerra A, Camarda M, Spontoni L, VECCHIO S, Bennati P, Cinti M N, Pani R, Campanini R, Iampieri E and Lanconelli N, Tomographic Approach to Single-Photon Breast Cancer Imaging with a Dedicated Dual-Head Camera with VAOR (SPEMT): Detector Characterization,

Conference Records of 2007 IEEE NSS/MIC/RTSD, Hawaii, USA, M13-61, 2901-5

2008-2 VECCHIO S, Attanasi F, Belcari N, Camarda M, Del Guerra A, Moehrs S, Rosso V, Lanconelli N, Cirrone G A P, Cuttone G, Di Rosa F and Russo G, A PET prototype for "in-beam" monitoring of proton therapy, Conference Records of 2007 IEEE NSS/MIC/RTSD, Hawaii, USA, N24-362, 1607-11

2008-3 Attanasi F Belcari N, Camarda M, Cirrone G A P, Cuttone G, Del Guerra A, Di Rosa F, Lanconelli N, Rosso V, Russo G and VECCHIO S (2008), Preliminary results of an in-beam PET prototype for proton therapy, Nucl. Instr. and Meth. A 591 (1) 296-9

2008-4 Attanasi F, Belcari N, Camarda M, Del Guerra A, Moehrs S, Rosso V, VECCHIO S, Lanconelli N, Cirrone G A P, Di Rosa F and Russo G (2008), Experimental validation of the filtering approach for dose monitoring in proton therapy at low energy, Physica Medica XXIV (2) 102-6.

2008-5 Attanasi F, Belcari N, Camarda M, Cirrone G A P, Cuttone G, Del Guerra A, Di Rosa F, Lanconelli N, Moehrs S, Rosso V, Russo G and VECCHIO S, Preliminary results from an "in-beam" PET system, LNS Activity Report 2007

2008-6 VECCHIO S and Attanasi A, Performance of the DoPET system for ^{12}C irradiation induced β^+-activity, GSI Scientific Report 2007, RADIATION-BIOPHYSICS-24, 378

2008-7 Camarda M, Belcari N, Del Guerra A, Spontoni L, VECCHIO S, Bennati P, Cinti M N, Pani R, Campanini R, Iampieri E and Lanconelli N (2008), SPEMT imaging with a dedicated VAoR dual-head camera: preliminary results, to appear on to Nucl. Instr. and Meth. A

XXXX-1 Agodi C, Antoccia A, Attanasi A, Attili A, Battistoni G, Berardinelli F, Bourhaleb F, Cherubini R, Cirio R, Cirrone G A P, Cuttone G, D'Ambrosio C, Del Guerra A, De Nadal V, Gerardi S, Marchetto F, Monaco P, Morone C, Mostacci A, Muraro S, Patera V, Peroni C, Raciti G, Rosso V, Sacchi R, Sala P, VECCHIO S, Tanzarella C, The INFN TPS project, to appear on Nuovo Cimento C

XXXX-2 VECCHIO S, Attanasi F, Belcari N, Camarda M, Del Guerra A, Moehrs S, Rosso V, Lanconelli N, Cirrone G A P, Cuttone G, Di Rosa F and Russo G,

A PET prototype for “in-beam” monitoring of proton therapy, submitted to IEEE Trans. Nucl. Sc.

Acknowledgments

My first grateful acknowledgment goes to Prof. Alberto Del Guerra for having accepted to be my supervisor. He trusted me when I still did not know anything about medical physics, and guided me to find my way through this field. He offered me several opportunities to travel, to get in touch with interesting research groups, and to increase my personal experience. In these last three years my spirit has been toughened, and I learned the importance of initiative and autonomy, as well as mind linearity and diplomacy.

Sincere gratitude is also owed to all the DoPET group: without their results and their collaboration, this work would not have been possible. Prof. Valeria Rosso performed her chairperson duties in an unimpeachable way, always keeping the group members in touch and dealing with management aspects. She has been a steady presence in writing papers and her suggestions have had a direct impact on the final form and quality of this thesis. Among the referential persons for all the software aspects of DoPET project, I would like to thank Dr. Nico Lanconelli for patiently tutoring me at my first experience with PET image reconstruction, and Francesca Attanasi for the fruitful discussions about SimSET and unfolding algorithm. I am also deeply grateful to Sascha Moehrs for his help on different software problems and for providing me part of his PHD work on iterative reconstruction algorithm as well as several other useful pieces of his code. Special thanks to the mechanical engineers and the members of the mechanical workshop of INFN-Pisa that designed and realized the DoPET components at very short notice.

I wish also to thank all the LNS-INFN staff who has permitted the experiments at the CATANA facility. Their contribution to this work go beyond the merely assistance in preparation and management of the proton beam, since they helped us to make it through the nights of beam time with pleasant diversions. I am deeply indebted to Dr. Giacomo Cuttone for his unlimited courtesy and helpfulness regarding the beam time assignment and every small and big trouble occurred

during the measurements. Many thanks to Dr. Pablo Cirrone, Giorgio Russo and Francesco Di Rosa who first introduced me to hadronic physics in GEANT4 and always find the time to answer to my questions.

Additionally, I would like to thank Prof. Thomas Bortfeld (MGH), who had to play the unconfortable role of forcing me to face up the unsatisfactory aspects of my work. No growth is possible without recognizing our own weak spots.

I am also thankful to all those people who made the data acquisition at GSI possible. Among them, Dr. Thomas Haberer (HIT) for organisation of the beam time, Prof. Wolfgang Enghardt (FZD) for the authorization to use BASTEI, Dr. Katia Parodi (HIT), Dr. Stephan Brons (HIT) and Dr. Dieter Schardt (GSI) for the preparation of the experiment and their complete assistance at each stage of run. We spent together a long troubled night, I hope that the results presented here can balance the lost sleep.

All the FIIG group from Pisa University substantially contributed to the development of this work. My thanks to my friends and colleagues for the great time I had in our group. I enjoyed the atmosphere, their friendship, and their support. It was a pleasure to work with all these people and to benefit from their knowledge. Above all I thank Manuela Camarda, which (bravely) followed us in Catania, shared a room with me and tolerated my hyperactivity even out of working time. She gave an unreplaceable contribution to the experimental work and proved to be a friend more than a colleague. Then, I would like to thank Dr. Nicola Belcari for the guide and the support that he has always offered me, and for the interesting and fruitful discussions starting from all my doubts. He was the one who convinced me to join the FIIG group, and I hope he does not regret it after he has faced the storm of my question during these years.

All my other friends, who are too many to be listed here, will personally receive my gratitude at another time and place. However, I can not fail to mention my parents and my brother, who have always supported me, even when I was the one supposed to support them...

Last but not least, I owe to Pino many thanks: I have made him the scapegoat of stressing moments, and he not only accepted this role with resignation, but he also got used to going along with my circuitous recover of serenity.